Theses and Dissertations

Fall 2016

Integration of deformable tire-soil interaction simulation capabilities in physics-based off-road mobility solver

Bryan Peterson
University of Iowa

Recommended Citation

Peterson, Bryan. "Integration of deformable tire-soil interaction simulation capabilities in physics-based off-road mobility solver." MS (Master of Science) thesis, University of Iowa, 2016.
http://ir.uiowa.edu/etd/2258.

INTEGRATION OF DEFORMABLE TIRE-SOIL INTERACTION SIMULATION

CAPABILITIES IN PHYSICS-BASED OFF-ROAD MOBILITY SOLVER

by

Bryan Peterson

A thesis submitted in partial fulfillment
of the requirements for the Master of
Science degree in Mechanical Engineering
in the Graduate College of
The University of Iowa

December 2016

Thesis Supervisor: Associate Professor Hiroyuki Sugiyama

Graduate College
The University of Iowa
Iowa City, Iowa

CERTIFICATE OF APPROVAL

_____

MASTER'S THESIS

_____

This is to certify that the Master's thesis of

Bryan Peterson

has been approved by the Examining Committee
for the thesis requirement for the Master of Science
degree in Mechanical Engineering at the December 2016 graduation.

Thesis Committee: _____
                         Hiroyuki Sugiyama, Thesis Supervisor

                   _____
                         Kyung K. Choi

                   _____
                         Albert Ratner

ACKNOWLEDGMENTS

ABSTRACT

The objective of this study is to integrate a continuum-based deformable tire and terrain interaction model into a general-purpose physics-based simulation environment capable of off-road vehicle mobility analysis and high-performance computing potential. Specifically, the physics-based deformable tire and terrain models which were recently proposed and validated by Yamashita, et al. will be implemented into the structure of the multi-physics simulation engine Chrono. In off-road vehicle mobility analysis, empirical and analytical models have been commonly used for vehicle-terrain interaction. While these models utilize experimental data or terramechanics theories to create quick predictive mobility models, they are unable to capture the highly nonlinear behavior of soft soil deformation, which can lead to inaccurate or unreliable results. In order to resolve these limitations, the use of physics-based numerical approaches have been proposed. These methods make use of finite element and discrete element simulations to describe the interaction between the vehicle and deformable terrain. Continuum-based finite element models transfer tire forces to the terrain and model the deformation with elasto-plastic constitutive equations. Discrete element soil uses a large number of small rigid body particles to describe the microscale behavior of granular terrain, with the deformation of the soil represented by the motion and contact of the particles. While these physics-based models offer a more accurate vehicle-terrain interaction model, the solution procedure can become complex and computationally expensive since co-simulation techniques are often used.

To address these issues, the analysis of physics-based full vehicle dynamics simulations utilizing high-fidelity deformable tire and terrain models in a multi-physics engine with high-performance computing capability is desired. To this end, the deformable tire model formulated using the continuum mechanics based shear deformable laminated composite shell element proposed by Yamashita, et al. was integrated into the flexible body dynamics simulation framework of Chrono. This shell element is based on the absolute nodal coordinate formulation and is defined by the global position coordinates and the transverse gradient coordinates of its four nodes. Element lockings are eliminated with the incorporation of the enhanced assumed strain (EAS) and assumed natural strain approaches (ANS). The element formulation includes an extension to model laminated composite materials. Additionally, a locking-free 9-node brick element was integrated into the Chrono framework that makes use of the curvature coordinates at

the center of the element. This element is formulated with the Hencky strain measure such that multiplicative finite strain plasticity theory can be used to incorporate soil plasticity models, such as the capped Drucker-Prager failure criterion.

With the shear deformable laminated composite shell element and plastic soil brick element integrated into the Chrono multi-physics simulation engine, an off-road deformable tire and terrain interaction model was developed using the vehicle dynamics simulation module Chrono::Vehicle. An off-road deformable tire model was parameterized based on commercial tire properties and generated as an interchangeable tire model option in the full vehicle dynamics system. Benchmark verification tests were performed to ensure the accuracy of tire deformation and tire force characteristics. Further tests were performed to validate a deformable tire model with a deformable tread pattern constructed from shear deformable shell elements and co-rotational tetrahedral elements. The deformable soil model was also integrated as a terrain option in Chrono::Vehicle and numerical tests were carried out to demonstrate its interaction with rigid and deformable tire models. Several numerical examples are presented to demonstrate the extension of the deformable tire and terrain models to full vehicle dynamics simulation using Chrono::Vehicle. To make use of the computational performance enhancements available in Chrono, Open Multi-Processing (OpenMP) and Advanced Vector Extensions (AVX) were applied to the evaluation of the elastic force/Jacobian matrix and large matrix operations of flexible bodies, respectively, in order to reduce the computation time by nearly 60%.

PUBLIC ABSTRACT

This study aims to develop a physics-based off-road vehicle mobility simulation environment by integrating a deformable tire and terrain interaction model into a multi-physics simulation engine with high-performance computing capability support. Because of the limitations that the empirical and analytical models widely used for vehicle mobility analysis present, there is a need for the development of physics-based mobility simulations that can make use of a single simulation architecture and high-performance computing. In this study, deformable tire and terrain models recently proposed by Yamashita, et al. were integrated into the multi-physics simulation engine Chrono. A structural off-road deformable tire model was designed using a shear deformable laminated composite shell element to model the fiber-reinforced rubber material. Additionally, a continuum-based soil model was integrated into the vehicle dynamics framework of Chrono using the capped Drucker-Prager failure criterion based on multiplicative plasticity theory. These additions allowed for the creation of a high-fidelity full vehicle dynamics simulation that can utilize deformable tires or terrain. Computational performance improvements were made considering Open Multi-Processing and Advance Vector Extensions and additional parallel computing potential exist for future development.

TABLE OF CONTENTS

LIST OF TABLES

LIST OF FIGURES

CHAPTER 1

INTRODUCTION

1.1 <u>Background and Motivation</u>

For off-road mobility performance evaluations, empirical and analytical vehicle-terrain interaction models have been widely used for decades. Empirical models make use of experimental data of terrain characteristics in order to parameterize a predictive model for off-road vehicle performance. This experimental data can include terrain properties such as cone index, moisture content, and topography. Analytical methods have been developed by Bekker [1] and Wong [2] as a means to consider terramechanics theories for cases of vehicle/terrain interaction. While these processes are computationally cheap, it is hard to capture many of the deformation modes and highly nonlinear soft soil behavior. Thus, use of empirical and analytical terramechanics model can result in inaccurate or unreliable results under severe dynamic loading scenarios [3]. To address the shortcomings of empirical and semi-empirical models, physics-based numerical simulations have been proposed utilizing finite element and discrete element approaches to describe the interaction between vehicle and deformable terrains [3,4,5,6,7,8,9,10,11]. In the case of finite element soil models, the terrain is represented by a continuum and the contact forces are transferred from the tire to the terrain with contact methods across the contacting surfaces. The internal forces are evaluated based on the constitutive model of the soil. Yielding criteria is defined through soil plasticity theories, like the Drucker-Prager or Mohr-Coulomb models, to describe permanent soil deformation and hardening characteristics due to consolidation. Using this methodology, the mobility of a vehicle through a snow was also predicted and validated against experimental results by Shoop [5].

On the other hand, for discrete element methods, the soil is modeled using a large amount of small particles in contact with each other to describe the microscopic granular soil behavior. The terrain deformation is represented by the motion of the particles due to the contact with the tire and other particles. The contact between discrete element particles can be formulated using a complementarity approach or a penalty method. In the complementarity approach, the particles are treated as rigid and the collisions of the particles at the given step are treated as constraints in the dynamic problem. These unilateral contact constraints introduce an optimization problem that must be solved to obtain the solution to the set of complementarity conditions. This unilateral

contact method also allows for a larger time step size as the rigid particle contacts do not introduce compliant forces unlike the penalty approach. In the penalty contact approach, on the other hand, the contact is modeled as set of spring and dampers that are a function of some interpenetration between the particles. This elastic collision can introduce large forces between the particles due to sudden increases in penetration depth, leading to high frequencies in the equations of motion. In order to handle this phenomenon, a smaller time step size is required. While discrete element soils can be advantageous when considering interaction with a rigid tire model, the use of deformable finite element tires can make the solution process complex [7,8]. This stems from the fact that implicit time integration methods are needed to effectively solve the finite element equations, while DEM terrain can be solved by explicit integration schemes. This issue is usually resolved through co-simulation techniques to guarantee numerical stability and accuracy at the sacrifice of computational efficiency. A comparative study on the complementarity and penalty approaches for modeling the deformable terrains was carried out using an physics-based off-road mobility solver Chrono in the literature [12].

Due to highly nonlinear material behaviors exhibited for tires and soils with large deformations, the computational vehicle/terrain interaction model becomes complex and computationally expensive. A single high-fidelity wheeled vehicle mobility simulation can be comprised of the mechanical parts of the vehicle body, four deformable finite element tires, and a continuum- or DEM-based soil model. Massively parallel architecture can be used to reduce the computation time of these large order systems. This can be achieved through the use of Open Multi-Processing (OpenMP) to divide the computational tasks amongst the available threads in a CPU. On a large scale, this process can be done over a multicore system to increase the total number of available threads, thus increasing the processing power. Additionally, parallel computing support can be found in the use of graphical processing units (GPU) to speed up the execution of single instruction multiple data (SIMD) operations. This is commonly used in the computational analysis of very large order systems, like DEM models or fluid/soil interaction using smoothed particle hydrodynamics [13].

Furthermore, in order to integrate deformable tires, terrains and vehicle components developed with different software for a single off-road vehicle model, co-simulation techniques have been utilized. This, however, requires extensive computational efforts to interface different codes in time domain and to assure numerical stability, especially under severe transient

maneuvering scenarios that need to be considered in off-road mobility performance evaluation. To address these computational and modeling challenges, a new continuum-based tire-soil interaction simulation capability that can be fully integrated into general multibody dynamics computational algorithm has been recently proposed by Yamashita, et al. using the flexible multibody dynamics techniques [14]. Using this approach, flexible tires, deformable soil and various rigid/flexible vehicle components can be modeled in a single multibody dynamics computational framework without resorting to co-simulation techniques. The nonlinear deformable tire model is developed using shear deformable laminated composite shell elements based on the finite element absolute nodal coordinate formulation, while deformable terrain is modeled using the finite element soil model using the capped Drucker-Prager failure criteria with the multiplicative finite plasticity theory [14]. These models were successfully validated against the test data [14]. However, use of high-performance computing as well as integration into high-fidelity full vehicle models have not yet been addressed rigorously. It is, therefore, the objective of this study to explore potential applicability of the deformable tire/soil model using the flexible multibody dynamics approach to the off-road mobility simulation using high-performance computing techniques.

1.2 Objectives of the Study

This study is conducted with the purpose of integrating a continuum-based deformable tire and terrain interaction simulation capability into a general-purpose physics-based off-road mobility simulation environment using high-performance computing. In particular, physics-based deformable tire and terrain models that were recently proposed and validated by Yamashita, et al. will be incorporated into the framework of the multi-physics simulation engine Chrono to allow for full vehicle simulation with deformable tire and terrain models analyzed in a single multi-physics engine. To achieve this goal, the following issues are addressed:

(1)   Implementation of a shear deformable composite shell element based on the absolute nodal coordinate formulation in flexible multibody dynamics simulation engine Chrono::FEA for modeling the fiber reinforced rubber material of deformable tire models.

(2)   Implementation of a 9-node brick element in Chrono::FEA to incorporate a continuum-based deformable terrain simulation capability in the off-road mobility solver Chrono. To account for the plastic soil behavior, the capped Drucker-Prager yield criterion is used with the multiplicative finite strain plasticity theory and is implemented in Chrono::FEA.

(3)   Development of a physics-based off-road deformable tire-soil interaction module capability in Chrono::Vehicle using high-performance computing techniques.

(4)   Analysis of wheeled and tracked vehicles on deformable terrain to demonstrate and validate the simulation capability developed in this study.

1.3 Organization of Thesis

This thesis is organized as follows: In Chapter 2, the structure and features of the multi-physics simulation engine Chrono, including flexible multibody dynamics, multi-physics support, and high performance computing methods will be discussed. The integration of a shear deformable laminated composite shell finite element based on the absolute nodal coordinate formulation and a 9-node brick finite element capable of modeling elasto-plastic behavior into the flexible body dynamics simulation framework of Chrono::FEA is detailed in Chapter 3. Chapter 4 will describe the development of deformable tire and terrain models using the added finite elements discussed in Chapter 3 as well as their integration into the vehicle dynamics module Chrono::Vehicle. Numerical examples for the finite element models and the deformable tire model will be shown in Chapter 5. Examples will be shown that will validate the accuracy of the laminated composite material models for the shear deformable shell element and the Drucker-Prager and Capped Drucker-Prager soil plasticity models for the 9-node brick element. Many numerical examples will then be presented to evaluate the performance of the deformable tire model and continuum based soil model. Finally, improvements made to the computational efficiency of the dynamics simulation code will be quantified and will also be presented in Chapter 5. Chapter 6 will present examples of simulations in which the deformable tire and terrain models are used in full vehicle dynamics scenarios. These examples will include acceleration and cornering of a vehicle with deformable tires on rigid terrain and vehicles interacting with the continuum soil model. Chapter 7 will provide the summary and conclusions of this study.

CHAPTER 2

FULL VEHICLE DYNAMIC SIMULATION FRAMEWORK

2.1 Introduction

In this chapter, the simulation environment for on- and off-road vehicle design and performance predictions within a large multi-physics simulation engine called Chrono will be briefly described. As discussed previously, it is crucial that the desired simulation engine used be capable of high-fidelity physics-based dynamics simulation considering complex dynamic tire deformation. This simulation environment must allow for the coupling of multibody dynamics simulation algorithms for vehicle components and nonlinear finite element procedures for large deformable bodies such as tires and soils. Therefore, there must be a general solution procedure that can be used for a variety of flexible multibody dynamics simulations in collaboration with multi-physics models. This generality will facilitate the construction of different simulation scenarios with various tire and vehicle configurations. Ultimately, the goal is to simulate multiple combinations of tire and terrain models with a range of accuracy. For simulations of large degree of freedom systems, the utilization of high performance computing methods will be instrumental. With these characteristics in mind, the multi-physics engine called Chrono was chosen as the framework for the advancement of physics-based full vehicle dynamics simulation. This code has also been tested and used as a modeling and simulation tool for military vehicles under various operational scenarios.

2.2 Chrono Software Overview

Chrono is a multibody physics engine which is capable of performing general purpose multibody dynamics simulation. The source code is of C++ inheritance and is open source available through an online repository via Github [12]. Chrono was originally developed by Alessandro Tasora in 1998 and has since been consistently developed by the Simulation-Based Engineering Lab (SBEL) at the University of Wisconsin-Madison under Dan Negrut [15]. Overall, Chrono is a physics-based modelling and simulation software that can make use of multibody systems, nonlinear finite element analysis, smoothed particle hydrodynamics, discrete element modelling, and high performance computing in a generalized, user-friendly framework.

Due to constant development, the Chrono structure is constantly expanding with more simulation capabilities and features. The code is structured such that new modules are built outward from the existing framework, as shown in Fig. 2.1. The core functionality of Chrono is the formulation and solving of a set of governing equations for a dynamics system. Upon this base, a set of modules were created for the analysis of different types of applications. Among these modules are Chrono::MBD for rigid multi-body dynamics simulation, Chrono::FEA for finite element analysis, and Chrono::FSI for the analysis of fluid/soil interactions. Additional toolkits were created that built off the core modules with specific applications in mind, allowing users to create and simulate more advanced systems in a streamlined fashion. These toolkits include Chrono::Vehicle, Chrono::Fording, and Chrono::Granular which can be used for vehicle dynamics simulation, modeling granular materials, and simulation of river fording scenarios, respectively.
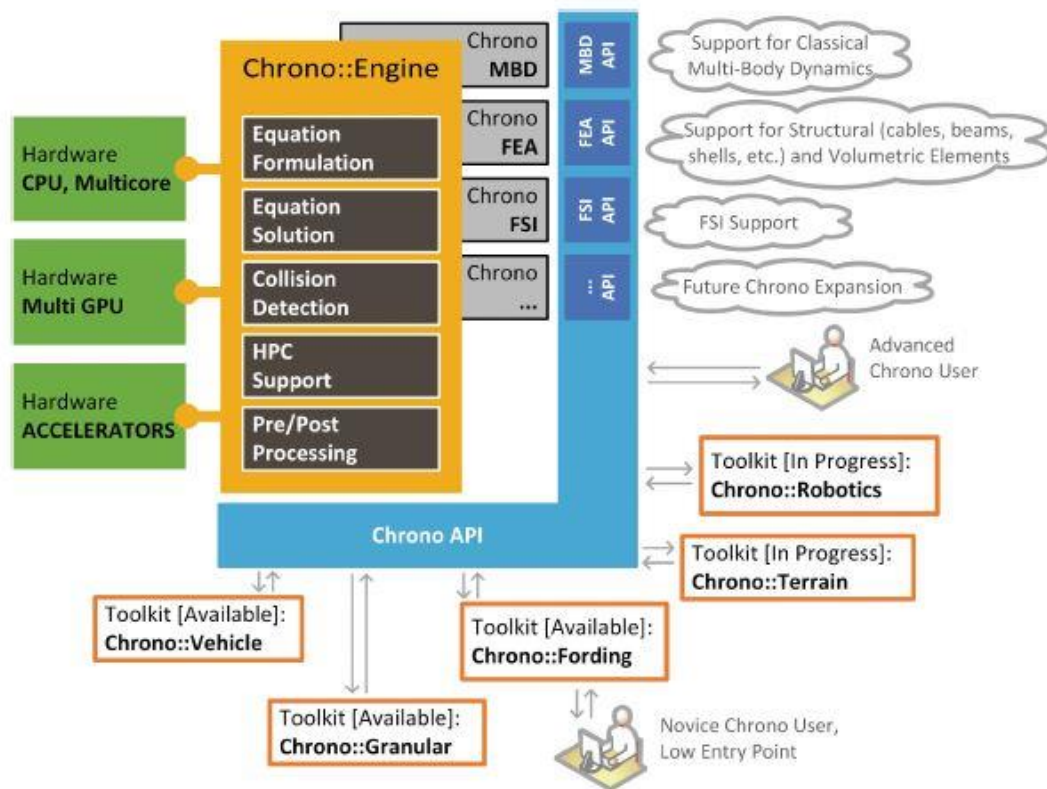
Figure 2.1: Diagram of the Project Chrono framework [12]

2.3 Chrono Vehicle Dynamics Simulation Capabilities

2.3.1 Multibody Dynamics Simulation Support in Chrono

Multibody dynamics simulation has been a primary function of Chrono since its inception. Chrono was originally created as a multibody dynamics tool with the purpose of simulating robotics and biomechanical applications. This led to the structure of Chrono having a primary focus on dynamics simulation capability. The equations of motion for a system of rigid bodies can be defined as the following set of differential algebraic equations [12]:

$$\dot{\mathbf{q}} = \mathbf{L}(\mathbf{q})\mathbf{v} \tag{2.1}$$

$$\mathbf{M}(\mathbf{q})\dot{\mathbf{v}} = \mathbf{f}(t,\mathbf{q},\mathbf{v}) - \mathbf{g}_{\mathbf{q}}^{T}(\mathbf{q},t)\hat{\boldsymbol{\lambda}} \tag{2.2}$$

$$\mathbf{g}(\mathbf{q},t) = \mathbf{0} \tag{2.3}$$

In Eq. 2.1, $\dot{\mathbf{q}}$ represents the time derivative of the generalized position coordinates, $\mathbf{v}$ is the system velocities, and $\mathbf{L}$ is a linear transformation matrix that relates the two values. Equation 2.2 defines the equations of motion of the multibody system subjected to constraint equations given by Equation 2.3. The rigid bodies themselves can be created as primitive shapes or by importing object files from 3D modeling software. In Chrono::MBD, primitive shapes can include a box, cone, cylinder, and sphere. The surfaces of these shapes are easily defined, which allows for the addition of collision detection and contact methods between bodies. Chrono utilizes the Bullet physics library for a collision detection algorithm between surfaces and both penalty and complementarity methods are available for contact force formulation [12]. Once the rigid body objects are defined, constraints can be applied between the bodies. The motion of the multibody system can then be defined by application of either driving constraints or external loads. This structure allows for the inertial properties and state information of the system's bodies as well as the Lagrange multipliers associated with the constraints to be introduced into the framework of the equations of motion. The system can then be solved at each time step and integrated using a selected time integration scheme to produce the dynamic results.

The use of this multibody dynamics framework can also be extended to integrate a set of differential inclusions. The inclusions can make use of unilateral constraints in order to change the system of equations from a set of differential algebraic equations to a differential variational inequality problem. In this framework, the unilateral constraints created a set of complementarity

conditions which can be solved as part of an optimization problem shown in the following equation [12]:

$$i \in A(\mathbf{q}(t)) : \begin{cases} 0 \leq \Phi_i(\mathbf{q}) \quad \perp \quad \hat{\gamma}_{i,\mathrm{n}} \geq 0 \\ \left(\hat{\gamma}_{i,u}, \hat{\gamma}_{i,\mathrm{w}} \right) = \underset{\sqrt{\hat{\gamma}_{i,u}^2 + \hat{\gamma}_{i,\mathrm{w}}^2} \leq \mu_i \hat{\gamma}_{i,\mathrm{n}}}{\arg\min} \left(\mathbf{v}^T \cdot \left(\overline{\gamma}_{i,u} \mathbf{D}_{i,u} + \overline{\gamma}_{i,\mathrm{w}} \mathbf{D}_{i,\mathrm{w}} \right) \right) \end{cases} \tag{2.4}$$

where i is the potential contact of a body in the active set $A(\mathbf{q}(t))$. The complementarity condition is given as the first equation in the set, where $\Phi_i(\mathbf{q})$ is the distance between the surfaces of two bodies and $\hat{\gamma}_{i,\mathrm{n}}$ is the normal contact force. In the second equation, $\mathbf{D}$ is used to project the force onto the particles surface. In Chrono::MBD, this is used to model the contact forces between colliding bodies. The equations of motion become the differential inclusion and the normal and tangential contact forces are defined as a set-valued function which is yet to be determined. The function is calculated from the optimization problem, as the first order Karush-Kuhn-Tucker optimality conditions are defined as the friction characteristics. The contact forces associated with the complementarity model are added to the equations of motions by altering Eq. 2.2 in the following way [12]:

$$\mathbf{M}(\mathbf{q}) \dot{\mathbf{v}} = \mathbf{f}(t, \mathbf{q}, \mathbf{v}) - g_{\mathbf{q}}^T(\mathbf{q}, t) \hat{\lambda} + \sum_{i \in A(\mathbf{q}, \delta)} \left(\hat{\gamma}_{i,\mathrm{n}} \mathbf{D}_{i,\mathrm{n}} + \hat{\gamma}_{i,u} \mathbf{D}_{i,u} + \hat{\gamma}_{i,\mathrm{w}} \mathbf{D}_{i,\mathrm{w}} \right) \tag{2.5}$$

2.3.2 Chrono::FEA

The Chrono::FEA module incorporates finite elements into the multi-body dynamics simulation framework. This module consist of a library of nodes, elements, and constraints that interact with the existing dynamics framework in order to describe the motion of flexible models. The Chrono::FEA module itself defines the characteristics of its components and how these components interact with each other. For example, in Chrono::FEA it is defined that nodes are needed to define an element structure and constraints must be applied to nodes. A tree show the inheritance from the Chrono::FEA module can be seen in Fig. 2.2. Each node and element class is derived from a generalized base class that defines the requirements that must be met to be able to communicate with the solution procedure. All nodes are derived from the base class "ChNodeBase", which provides a bookkeeping method for the information stored by each node. For finite element nodes specifically, the node classes are derived from "ChNodeFEAbase", which is made up of functions that define inertial properties and organizing state information. In a similar

manner, all element classes in Chrono::FEA inherit from "ChElementBase", which defines the necessary functions that are needed to construct the equations of motion. Among these functions are the computation of the internal force vector, calculation of the mass matrix, and the evaluation of the stiffness matrix. This also defines functions that load these vectors and matrices into the governing equations to be solved. In order to create a finite element in Chrono::FEA, the user must provide some key information, including the corresponding nodes of the element, materials properties, and dimensions. The element shape is determined by the order and the location of the nodes. Each element class must also have a compatible material model, which will describe the structural properties of the element. These material classes often include parameters such as the Young's modulus, Poisson's ratio, and density, but can also include a stiffness matrix or damping coefficients.

Once the nodes and elements are added to the dynamics system, constraints and external loads can be applied. Constraints can be enforced through either elimination of the nodal coordinates in the equations of motion or by constraint equations on the nodal positions. External forces and torques can be applied to the flexible bodies in multiple ways. At the nodal level, point load vectors can be applied as well as an initial velocity or acceleration condition. For elements, external forces can be applied over area or volumes using load classes. These classes integrate over the elements area or volume using the analytical shape functions to define the loading condition. This is done using the classes "ChLoadableUV" for loads over a surface and "ChLoadableUVW" for loads applied across element volumes.
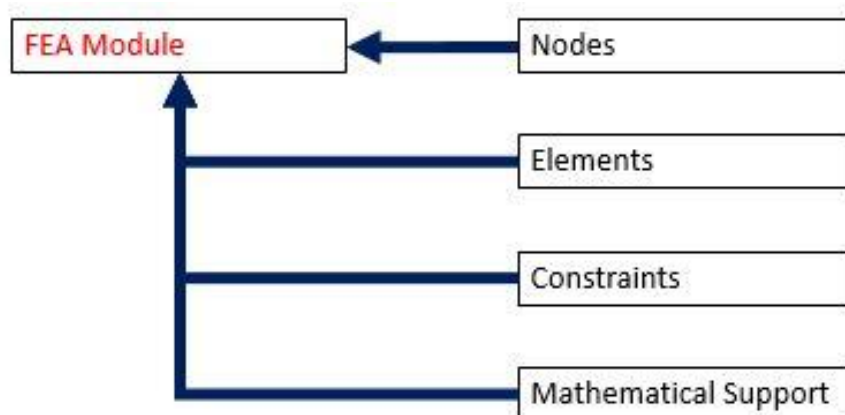
Figure 2.2: Inheritance tree of the Chrono::FEA module with all subsystems

2.3.3 Chrono::Vehicle

Chrono::Vehicle was created in order to streamline the process of creating a detailed full vehicle model with current support for wheeled and tracked vehicles. This module makes use of rigid body dynamics simulation and the features of Chrono::FEA to model and assemble various vehicle components in a more straightforward manner. The vehicle system is modular, such that different parts of the vehicle are easily defined, identifiable, and able to be altered. As shown in Fig. 2.3, among the subsystems in Chrono::Vehicle are models for driver input, powertrain models, various types of terrains, and two classes of vehicles: using either wheels or tracks. An entire wheeled vehicle system in Chrono::Vehicle consists of a chassis, suspension, rim-set, wheelset, tire-set, and braking system. In the case of a tracked vehicle, the rims, wheels, and tires are replaced with a sprocket and track-shoe system. A diagram of the subsystems of a wheeled vehicle is shown in Fig 2.4, while the subsystem tree for a tracked vehicle is shown in Fig. 2.5.
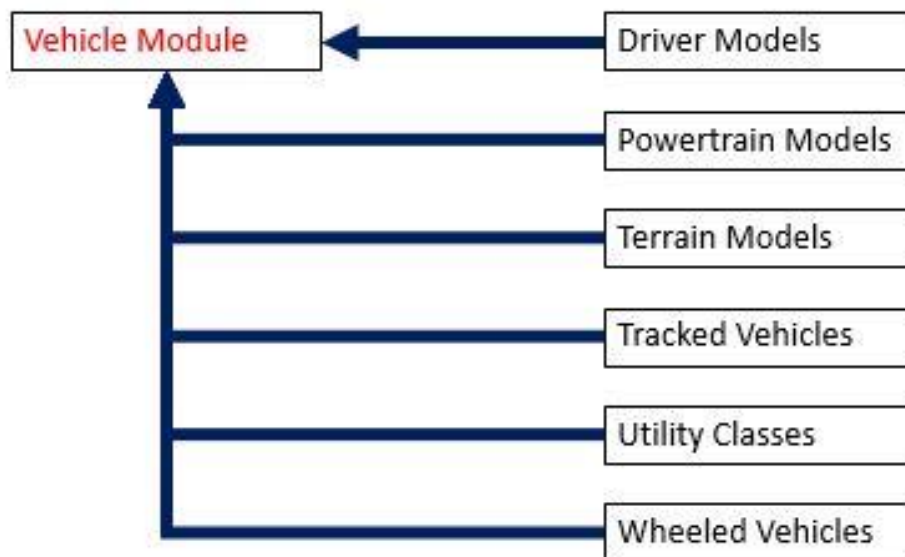
Figure 2.3: Inheritance tree of the Chrono::Vehicle module with all subsystems
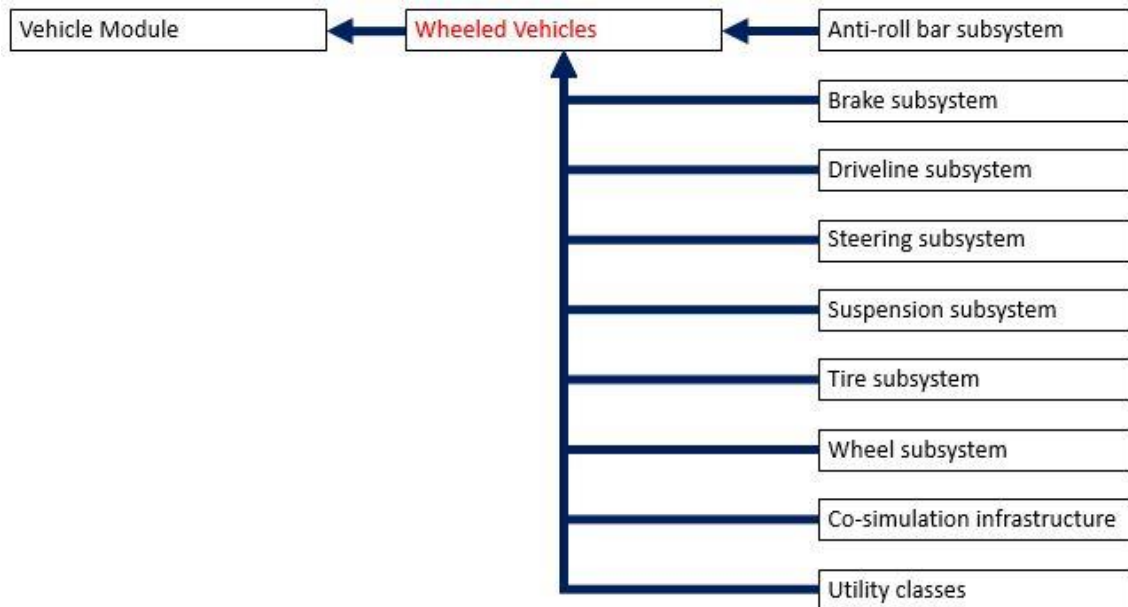
Figure 2.4: Inheritance tree of the wheeled vehicle class in Chrono::Vehicle
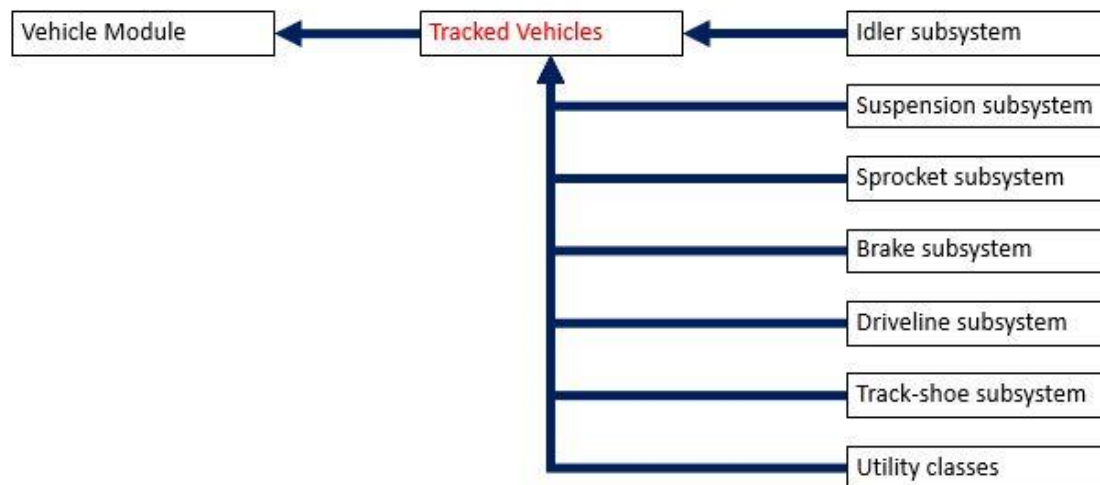
Figure 2.5: Inheritance tree of the tracked vehicle class in Chrono::Vehicle

In order to demonstrate the interaction between these many subsystems of a wheeled vehicle, a sample wheeled vehicle is illustrated in Fig. 2.6 with an exploded view of its components. It is important to note here that each of these models are interchangeable. This allows the user to create models using different vehicle bodies and run them with a variety of analytical tire models over different terrains and obstacles. The motion of the vehicle model is described by a driver model, which creates functions for the vehicle's throttle, brakes, and steering. The throttle

and braking values are altered by applying torques to the revolute joints between the rim and wheel, while the steering is a set rotation range that is mapped from -1 to 1. A tire test rig model exists using the Chrono::Vehicle structure so that different tire models could be simulated on different types of terrain models in a more simplified system. This system uses a simplified vehicle model consisting of the same vehicle parts and this structure is illustrated in Fig. 2.7.

The Chrono::Vehicle module has a library for a different rigid-body based tire models as well as deformable terrain models. The available handling-type tire models include a simple rigid cylindrical tire, a Pacejka tire model [16], and a LuGre tire model [17]. Although these analytical tire models can introduce a more realistic representation of tire dynamics, there is a distinct lack
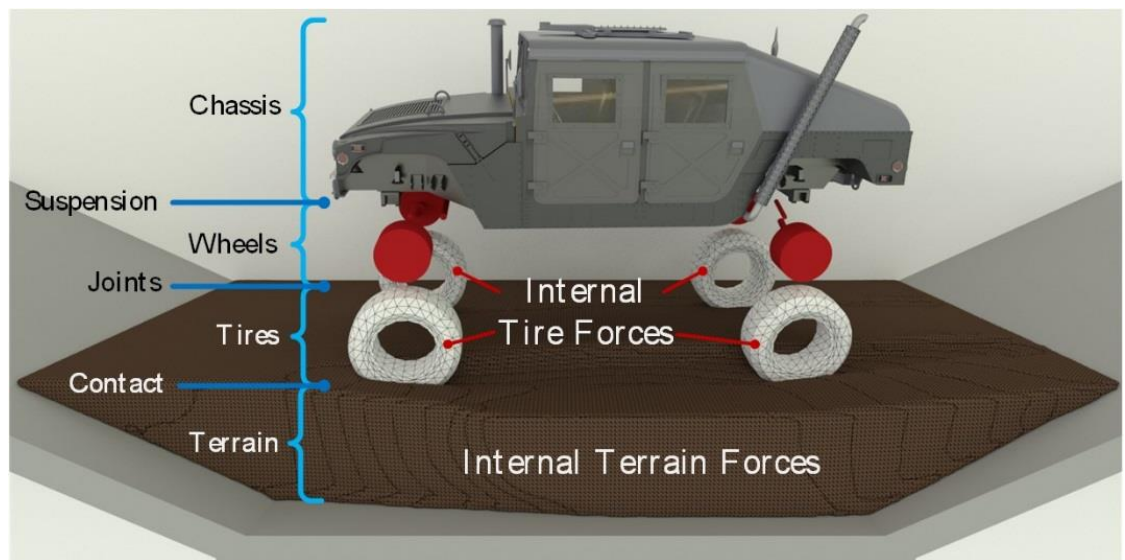
Figure 2.6: Structure of a full wheeled vehicle system in Chrono::Vehicle
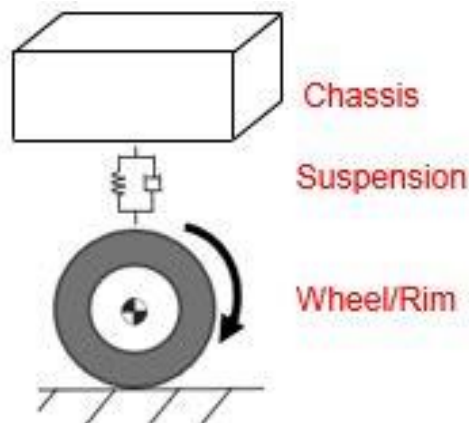
Figure 2.7: Structure of a simplified tire test rig model in Chrono::Vehicle

of a deformable physics-based tire modeling capability in Chrono::Vehicle. The available models cannot capture the structural tire deformation of the fiber-reinforced rubber material that makes up tires. Consideration of the nonlinear tire structure has a significant impact of the tire shape, which in turn alters the normal and tangential contact stress pressure distribution and affects the overall tire and vehicle dynamics. This creates the opportunity for a high-fidelity deformable tire model to be integrated into the physics-based vehicle dynamics simulation framework. Additionally, while granular terrain models exist in the Chrono::Vehicle architecture, there is a need for a continuum-based finite element soil model for cohesive soil. This model should be capable of exhibiting the plastic deformation of a tire footprint in a loose soil, allowing for prediction of drawbar pull and rolling resistance of a tire on cohesive soil.

2.3.4 Multi-physics Simulation Support in Chrono

Chrono has additional support for multi-physics simulation, which can create more complex vehicle mobility simulations. In particular, the use of discrete element method (DEM) and smoothed-particle hydrodynamics (SPH) are supported in Chrono and are instrumental to the toolkits Chrono::Granular and Chrono::Fording, respectively. The discrete element method is primarily used for the simulation of granular soil models, as shown in the anchoring simulation in Fig. 2.8.
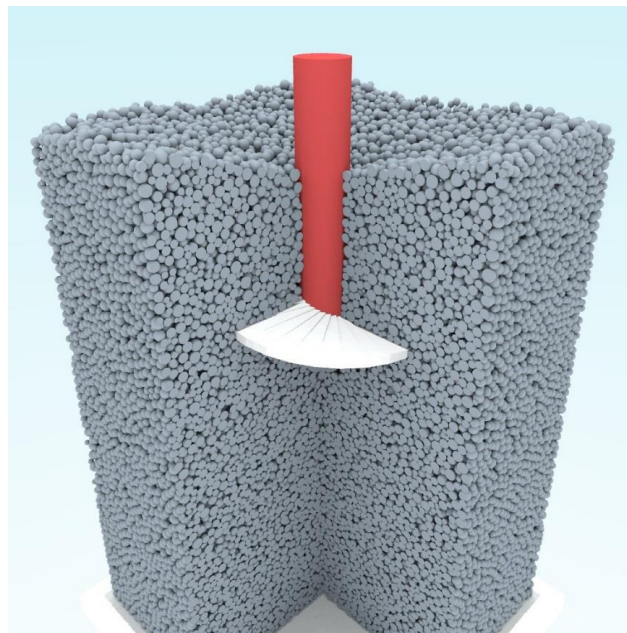
Figure 2.8: An example of an anchoring simulation utilizing granular material
modeled with discrete element method [18]

The soil models are comprised of tens of thousands of discrete element particles of varying distribution samples that utilize either a penalty-based (DEM-P) or complementarity-based (DEM-C) contact method as well as cohesion properties between particles. The DEM-C method uses the complementarity condition to solve the optimization problem described in Section 2.3.1. In this case, there are six constraints created for each contact between two particles in order to evaluate the contact forces. This allows the contact of the DEM particles to be modeled with mutual-contact without penetration, where the rolling and sliding friction is determined by the optimization process. For the DEM-P case, the contact forces are evaluated as a function of an interpenetration between the particles. The contact force formulation for the normal and tangential force are given in the following equations: [12]

$$
\begin{aligned}
\mathbf{F}_n &= f\left(\bar{R}, \delta_n\right)\left(k_n \mathbf{u}_n - \gamma_n \bar{m}\mathbf{v}_n\right) \\
\mathbf{F}_t &= f\left(\bar{R}, \delta_n\right)\left(k_t \mathbf{u}_t - \gamma_t \bar{m}\mathbf{v}_t\right)
\end{aligned}
\tag{2.6}
$$

where δ_n is the interpenetration between the DEM particles, k is the contact stiffness coefficient, γ is the contact damping coefficient, $\mathbf{u}$ is the contact displacement vector between the two contacting bodies, and $\mathbf{v}$ is the vector of the relative velocity at the point of contact. The effective mass $\bar{m}$ and effective radius of curvatures $\bar{R}$ are defined with the following equations: [12]

$$
\begin{aligned}
\bar{m} &= m_i m_j / \left(m_i + m_j\right) \\
\bar{R} &= R_i R_j / \left(R_i + R_j\right)
\end{aligned}
\tag{2.7}
$$

for contacting bodies i and j. The function $f\left(\bar{R}, \delta_n\right)$ is determined by the contact theory chosen by the user as either Hookean or Hertzian. For the former, $f\left(\bar{R}, \delta_n\right) = 1$ and for the latter, $f\left(\bar{R}, \delta_n\right) = \sqrt{\bar{R}\delta_n}$. The application of the normal and tangential contact forces from DEM-P particles is shown in Fig. 2.9. The large order of the DEM system may be computationally expensive, but this cost can be significantly reduced through the high performance computing and parallelism techniques that will be discussed in the following section.

The use of smoothed-particle hydrodynamics was implemented as part of the module for fluid/soil interaction, Chrono::FSI. This module has the capability to simulate fluid interaction with rigid bodies and flexible beams by incorporating the Navier-Stokes equations into the
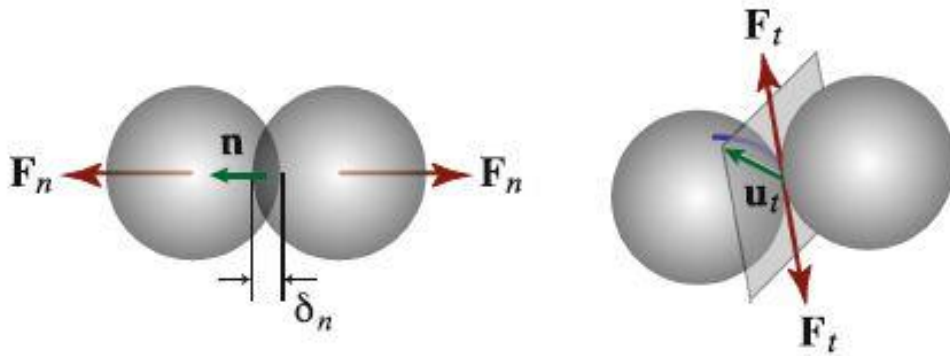
Figure 2.9: The definition of the normal and tangential contact forces between DEM particles using the penalty-based contact method [12]

equations of motion for a multi-body dynamics system. These equations are defined in the following way: [12]

$$
\frac{d\rho_a}{dt} = \rho_a \sum_b \frac{m_b}{\rho_b} \left(\mathbf{v}_a - \mathbf{v}_b \right) \cdot \nabla_a W_{ab}
$$

$$
\frac{d\mathbf{v}_a}{dt} = -\sum_b m_b \left[\left(\frac{p_a}{\rho_a^2} + \frac{p_b}{\rho_b^2} \right) \nabla_a W_{ab} - \frac{\left(\mu_a + \mu_b \right) \mathbf{x}_{ab} \cdot \nabla_a W_{ab}}{\rho_{ab}^{-2} \left(x_{ab}^2 + \varepsilon h^2 \right)} \mathbf{v}_{ab} \right] + \mathbf{f}_a
$$

(2.8)

where ρ is the fluid density, $\mathbf{v}$ is the flow velocity, p is the flow pressure, $\mathbf{f}$ is the fluid body force, and μ is the fluid viscosity. The subscripts a and b are used to identify two markers at different positions and the subscript ab is used to express the difference of the value between the markers as $\mathbf{x}_a - \mathbf{x}_b$. An example of a fluid simulation with both rigid and flexible bodies in shown in Fig. 2.10. This functionality was then extended in order to simulate vehicle-fording scenarios through a trough of flowing water. Much like the use of DEM, the computational burden of SPH can be reduced from parallelism methods.

2.4 High Performance Computing Capabilities

Because of the increasingly complex nature of the full vehicle dynamics simulations, high performance computing capability is essential to the practicality of this work. As an open source multi-body physics engine, Chrono is being constantly updated to include more techniques for
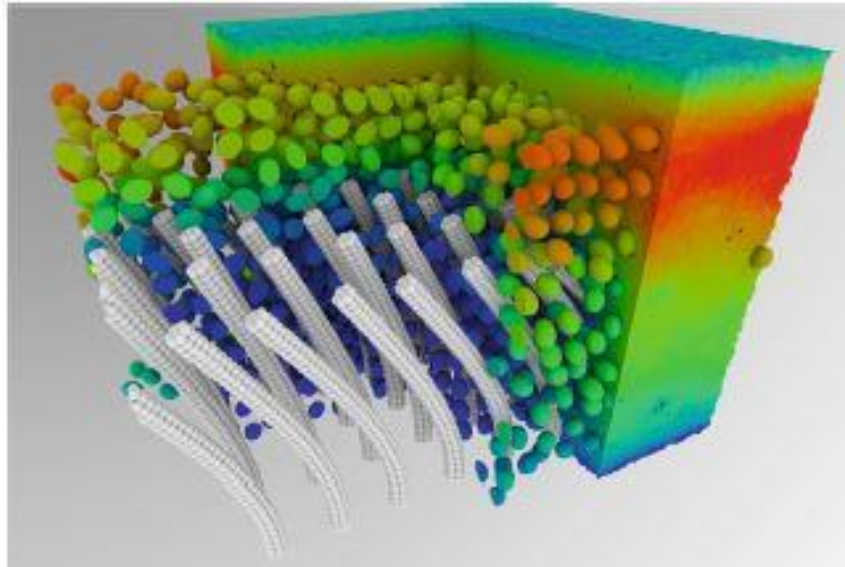
Figure 2.10: Sample simulation of the interaction between smoothed-particle hydrodynamics with rigid bodies and flexible beams [12]

HPC and performance enhancement. As shown in Fig. 2.1, Chrono is able to be used on many different computing platforms which will have varying capacities for high performance computing based on the number of available processing cores. Chrono has the capability to introduce parallelism when multiple cores are present using methods such as Open MP, MPI, and GPU. These techniques are needed for large-scale computational models involving DEM and SPH. When considering a full vehicle model with deformable tires, granular terrain consisting of one quarter million particles, or dynamic fluid-structure interaction, the required computational time can be enormous. With the inclusion of these parallel computing methods, the performance can be improved as a function of the number of cores devoted to the calculation. However, this scalability is not perfect, as some overhead process time will be required to split the calculations amongst the cores. Therefore as the total number of processors increase, the parallel efficiency will be reduced.

CHAPTER 3

INTEGRATION OF SHELL AND BRICK ELEMENTS FOR TIRE AND
TERRAIN MODELING INTO CHRONO::FEA

3.1 Introduction

In this chapter, a shear deformable shell element and 9-node brick element are integrated into the framework of Chrono::FEA in order to create physics-based computational models for deformable tires and terrains for off-road mobility simulation. The shear deformable shell element based on the absolute nodal coordinate formulation is specifically chosen because this can be implemented in a multibody dynamics framework in a straightforward manner. This shear deformable shell element utilizes the transverse gradient vectors to describe the orientation and deformation along the thickness of the shell [19]. Additionally, the generalized elastic force formulation for this element can be extended to accurately describe the properties of fiber-reinforced rubber material for tries. This material structure plays a very important role in the dynamics of a deforming tire and must be accurately represented by a laminated composite shell element. Additionally, a 9-node brick element was integrated in the element library of Chrono::FEA in order to model a plastically deformable soil terrain. The brick element uses the curvature coordinates at the center of the element to alleviate the element locking resulting from the use of lower order of polynomials [14]. The Hencky strain measure is used such that multiplicative finite plasticity theories can be implemented using return mapping algorithms developed for the infinitesimal plasticity theories [20].

3.2 Shear Deformable Shell Element

The shear deformable shell element based on the absolute nodal coordinate formulation consists of four nodes, with each possessing the global position coordinates as well as the transverse gradient coordinates aligned with the thickness of the element, as shown in Fig. 3.1 [19]. These gradient coordinates are necessary to describe the orientation of the element and the deformation of the element cross section. The global position vector $\mathbf{r}^i$ of a material point $\mathbf{x}^i = [x^i \quad y^i \quad z^i]^{\mathrm{T}}$ in shell element i is defined as

$$\mathbf{r}^i = \mathbf{r}_m^i(x^i, y^i) + z^i \frac{\partial \mathbf{r}^i}{\partial z^i}(x^i, y^i) \tag{3.1}$$

where $\mathbf{r}_m^i(x^i, y^i)$ is the global position vector of the middle surface and $\partial \mathbf{r}^i(x^i, y^i)/\partial z^i$ is the transverse gradient vector, as shown in Fig. 3.1. The global displacement field is interpolated using a bi-linear polynomial to obtain the element shape functions. Using this shear deformable shell element, the mass matrix is constant in time for fully nonlinear dynamics problems, allowing for the use of non-incremental solution procedure adopted in a general-purpose multibody dynamics simulation framework.

3.2.1 Generalized Elastic Force Formulation

The generalized elastic forces for the shear deformable shell element are formulated using a continuum mechanics approach, which allows for the inclusion of nonlinear constitutive models. In this approach, the shell is evaluated as a continuum volume. The element uses the Green-Lagrange strain formulation which defines the strain tensor $\mathbf{E}$ at an arbitrary point on element i as follows: [19]

$$\mathbf{E}^i = \frac{1}{2}\left((\mathbf{F}^i)^T \mathbf{F}^i - \mathbf{I}\right) \tag{3.2}$$

where $\mathbf{F}^i$ is the global position vector gradient tensor defined by

$$\mathbf{F}^i = \frac{\partial \mathbf{r}^i}{\partial \mathbf{X}^i} = \frac{\partial \mathbf{r}^i}{\partial \mathbf{x}^i}\left(\frac{\partial \mathbf{X}^i}{\partial \mathbf{x}^i}\right)^{-1} = \bar{\mathbf{J}}^i\,(\mathbf{J}^i)^{-1} \tag{3.3}$$

where $\bar{\mathbf{J}}^i = \partial \mathbf{r}^i/\partial \mathbf{x}^i$ and $\mathbf{J}^i = \partial \mathbf{X}^i/\partial \mathbf{x}^i$ while $\mathbf{X}^i$ is an arbitrary reference configuration of the global position vector of element i. It is then possible to obtain the generalized elastic forces using the virtual work as follows:

$$\mathbf{Q}_k^i = \int_{V_0^i}\left(\frac{\partial \boldsymbol{\varepsilon}^i}{\partial \mathbf{e}^i}\right)^T \boldsymbol{\sigma}^i dV_0^i \tag{3.4}$$

where $\boldsymbol{\sigma}^i$ is a vector of the second Piola–Kirchhoff stresses and dV_0^i is the infinitesimal volume at the reference configuration of element i. . Since the shell element is formulated as a continuum solid with a three-dimensional stress state, the generalized elastic forces of a laminated composite shell element can be defined as follow: [22]
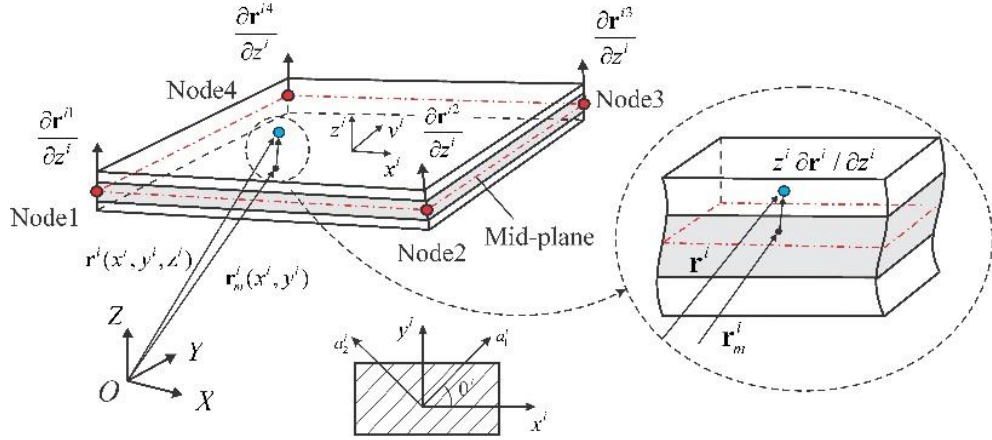
Figure 3.1: Kinematics of bi-linear shear deformable laminated composite element [21]

$$\mathbf{Q}_s^i = -\sum_{k=1}^{N} \int_{V_0^{ik}} \left(\frac{\partial \boldsymbol{\varepsilon}^{ik}}{\partial \mathbf{e}^i} \right)^T \frac{\partial W^{ik}(\boldsymbol{\varepsilon}^{ik})}{\partial \boldsymbol{\varepsilon}^{ik}} dV_0^{ik} \tag{3.5}$$

In the preceding equation, the integration range for the k-th laminae in the positive thickness direction is from z_{k-1} to z_k. With this formulation, the generalized elastic force is calculated as the sum of the elastic force vectors of each layer as shown in Eq. 3.5.

3.2.2 Shear and Thickness Locking Remedies

The problem of transverse shear locking and in-plane shear/normal locking for bi-linear quadrilateral shell elements has been well-documented in the literature [21,23,24,25,26,27,28,29,30,31]. The transverse shear locking is alleviated by the use of the assumed natural strain (ANS). With this methodology, the covariant transverse shear strain is calculated at sampling points at the midpoints of each of the edges of the shell element. The covariant transverse shear strains are then interpolated using the following equations: [21,31]

$$\left. \begin{aligned} \tilde{\gamma}_{yz}^{ANS} &= \frac{1}{2}(1-\xi)\tilde{\gamma}_{yz}^A + \frac{1}{2}(1+\xi)\tilde{\gamma}_{yz}^B \\ \tilde{\gamma}_{xz}^{ANS} &= \frac{1}{2}(1-\eta)\tilde{\gamma}_{xz}^C + \frac{1}{2}(1+\eta)\tilde{\gamma}_{xz}^D \end{aligned} \right\} \tag{3.6}$$

where $\tilde{\gamma}_{yz}^A$, $\tilde{\gamma}_{yz}^B$, $\tilde{\gamma}_{xz}^C$ and $\tilde{\gamma}_{xz}^D$ are compatible covariant transverse shear strains at the four sampling points labelled A, B, C, and D, as illustrated in Fig. 3.2.
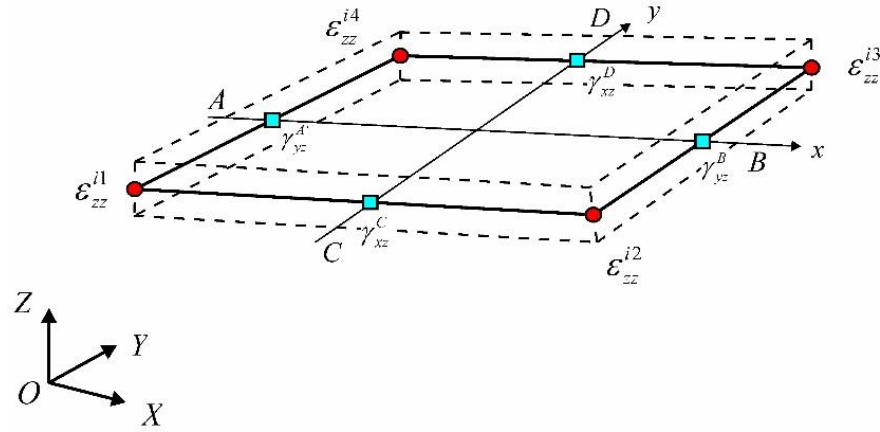
Figure 3.2: Sampling points for assumed natural strain calculation [21]

Another typical locking scenario occurs for the in-plane shear stress when a bi-linear shell element is subjected to pure bending loads. To combat this, the compatible in-plane strains (ε_{xx}, ε_{yy} and γ_{xy}) are improved with the introduction of enhanced assumed strains $\boldsymbol{\varepsilon}^{EAS}$ in the following manner: [25,29]

$$\boldsymbol{\varepsilon} = \boldsymbol{\varepsilon}^c + \boldsymbol{\varepsilon}^{EAS} \tag{3.7}$$

where $\boldsymbol{\varepsilon}^c$ represents the compatible strain vector, which are obtained by the assumed displacement field, and the strain vector $\boldsymbol{\varepsilon}^{EAS}$ is defined by

$$\boldsymbol{\varepsilon}^{EAS}(\boldsymbol{\xi}) = \mathbf{G}(\boldsymbol{\xi})\boldsymbol{\alpha} \tag{3.8}$$

where $\boldsymbol{\alpha}$ is used here as a vector of parameters that describe the additional in-plane strain field. The above $\mathbf{G}(\boldsymbol{\xi})$ matrix is a function of the global position vector gradient matrix at the reference configuration. The vector $\boldsymbol{\xi}$ consists of element natural coordinates. It is required that the assumed stress and strain must meet the following orthogonality condition: [25]

$$\int_{V_0} \boldsymbol{\sigma} \cdot \boldsymbol{\varepsilon}^{EAS} dV_0 = 0 \tag{3.9}$$

With the previous condition satisfied, the assumed stress term that appears in the generalized elastic force vector as follows:

$$\mathbf{Q}_k^i = -\int_{V_0^i} \left(\frac{\partial \boldsymbol{\varepsilon}^c}{\partial \mathbf{e}^i} \right)^T \frac{\partial W^i (\boldsymbol{\varepsilon}^c + \boldsymbol{\varepsilon}^{EAS})}{\partial \boldsymbol{\varepsilon}^i} dV_0^i \tag{3.10}$$

where W is an elastic energy function.

Due to the use of the transverse gradient vectors in the shear deformable shell element, additional locking occurs for the transverse normal strain and elongation is introduced in the thickness as the element undergoes pure bending or twisting deformation. The assumed natural strain (ANS), shown above, is also used to alleviate this curvature thickness locking using the following approximation: [26]

$$\varepsilon_{zz}^{ANS} = S_1^{ANS}\varepsilon_{zz}^1 + S_2^{ANS}\varepsilon_{zz}^2 + S_3^{ANS}\varepsilon_{zz}^3 + S_4^{ANS}\varepsilon_{zz}^4 \tag{3.11}$$

where ε_{zz}^k indicates the compatible transverse normal strain at node k and S_k^{ANS} is the associated shape function. This method can be used to counter the curvature thickness locking because the bi-linear shell element uses an elastic middle surface approach and the thickness strain distribution is assumed to be constant. Additional thickness locking is introduced from the coupling of the in-plane strains and the transverse normal strain due to the Poisson's ratio. This locking issue is resolved by introducing an additional term in the enhanced assumed strain associated with the transverse normal strain [23,32]. The following equation is used to calculate the transverse normal strain while alleviating the curvature thickness locking and the Poisson's thickness locking: [32]

$$\varepsilon_{zz} = \varepsilon_{zz}^{ANS} + \varepsilon_{zz}^{EAS} \tag{3.12}$$

In essence, the compatible transverse normal strain is replaced and added to the enhanced transverse normal strain.

3.2.3 Implementation of Shell Element into Chrono::FEA

The implementation of this element into the Chrono::FEA framework requires many considerations. The formulation of the shear deformable shell element must be adapted to cooperate with the existing Chrono system and libraries. In its current state, Chrono::FEA primarily is designed for co-rotational elements in dynamic simulation of structural elements [12]. Therefore, new node and element classes were developed to integrate the shear deformable shell element based on the absolute nodal coordinate formulation. There were crucial additions made to solution procedure as well to help improve the performance and convergence of the element.

As mentioned previously, the initialization of an element in Chrono::FEA requires the nodal information. Therefore, it is necessary to create the nodal landscape of the total finite element mesh before creating the individual elements. For the shear deformable shell element, a new node object was created to account for the transverse gradient coordinate vector. The new node class,

titled "ChNodeFEAxyzD", is able to store two vectors of state information, those being the global position coordinate and the transverse gradient coordinate. This class can use this state information to calculate state derivatives as well as communicate this information to the system's solver. This class inherits from the class "ChNodeFEAxyz", which is used as a finite element node that only contains the global position coordinates as the state information. The full class inheritance is shown in Fig. 3.3, which show the classes from which the new node positon and gradient class is derived. This includes classes "ChNodeFEAbase" and "ChNodeXYZ", the former defines the requirements of a node used for finite element analysis applications and the latter defines nodes that are described using a position vector in three-dimensional space. It is important to note here that ChNodeXYZ does not exist within the "fea" namespace, so this particular class is not used for finite element simulations. Both of these classes then inherit from "ChNodeBase", which is the most basic class for describing all nodes within the Chrono system.

The element class was created as an interface between the new ChNodeFEAxyzD nodes and the generalized elastic forces. This class was known as "ChElementShellANCF" and contains functions for the calculation of the elastic forces, mass matrix, gravitational force, and Jacobian matrix. These element functions are required to interface with the solution procedure of the Chrono system. As previously mentioned, there are instances in the solution procedure that must collect the internal force vector and the elastic force Jacobian in order to construct the equations of motion
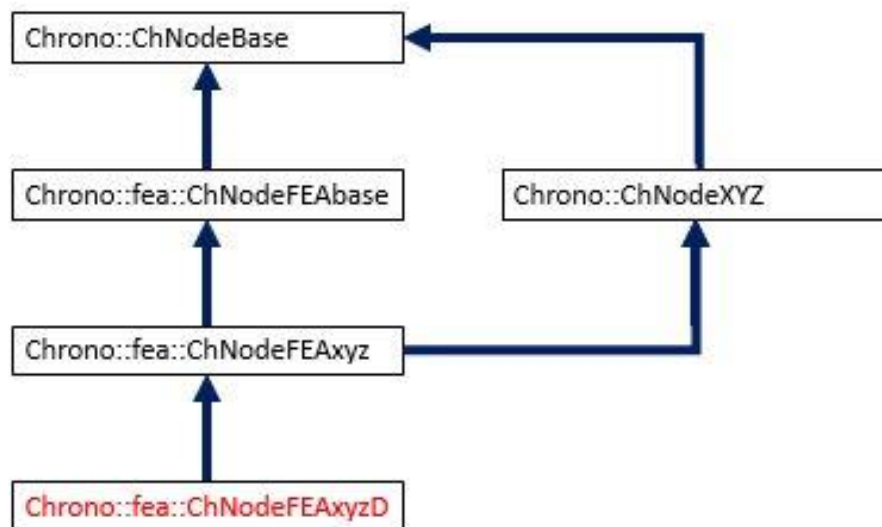
Figure 3.3: Inheritance of the node class containing position and transverse gradient coordinates in Chrono::FEA

and the new element class is required to contain these functions based the collaboration with other classes. The inheritance of the class for the shear deformable shell element are shown in Fig. 3.4, which shows the relationship with other finite element classes as well as external load classes. These external load classes are used to apply forces over element area or volumes by classes "ChLoadableUV' and "ChLoadableUVW", respectively. As shown in Fig. 3.4, the shear deformable shell element inherits from a class that defines all shell elements. This allows the shear deformable shell element to simply meet the requirements for the shell element class and be defined only by its formulation. There are additional parameters that need to be provided by the user in order to create an accurate shell element model. A material model class was created specifically for the shear deformable shell element that contains material property information, which includes the density and three-dimensional vectors for the Young's modulus, Poisson's ratio, and Bulk modulus parameters. This allows multiple material models to be created to be used in a single simulation. To facilitate the creation of a laminated composite shell element, a subclass of the shear deformable shell element was created to contain the layer information. This class contains the layer thickness, fiber angle for orthotropic material, and material model for a single layer that can be added sequentially to an element. Additional parameters required for the shear deformable shell element include the in-plane dimensions, the four corresponding ChNodeFEAxyzD nodes that define element, and a structural damping coefficient to improve the solution convergence.
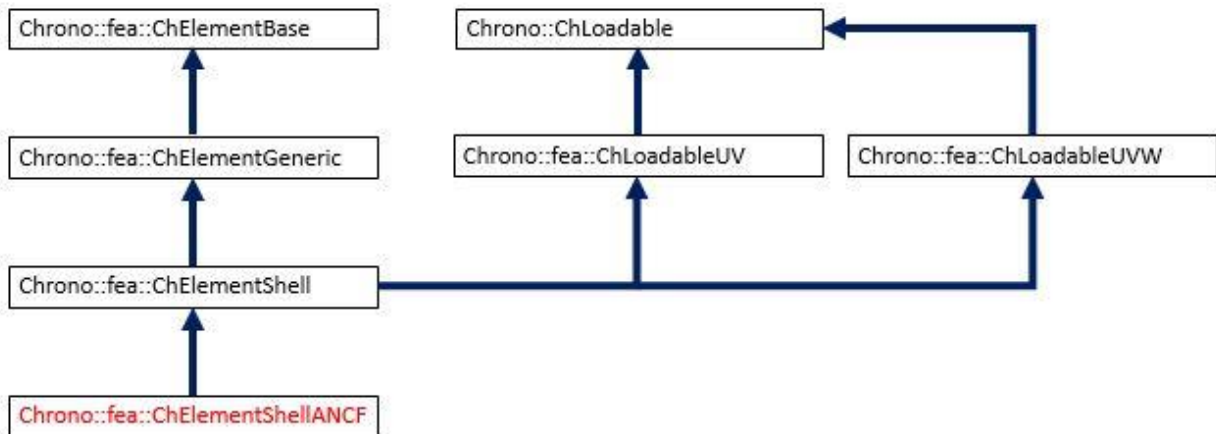
Figure 3.4: Inheritance of the shear deformable shell element in Chrono::FEA

3.3 9-Node Brick Element with Curvature Coordinates

For the purpose of creating an accurate continuum-based terrain model, a 9-node brick element proposed by Yamashita, et al. [14] was added to Chrono::FEA. This element builds off of a standard tri-linear 8-node brick element by considering additional curvature coordinates at the center of the element to alleviate the locking caused by the difficulties in capturing the linear stress and strain distribution over the volume of the 8-node element. By utilizing the additional curvature node, the lengthy calculations of iterative locking remedies can be avoided without the addition of internal element parameters. In this formulation, the quadratic terms of the following polynomial are considered as

$$r = a_0 + a_1\xi + a_2\eta + a_3\zeta + a_4\xi\eta + a_5\xi\zeta + a_6\eta\zeta + a_7\xi\eta\zeta + a_8\xi^2 + a_9\eta^2 + a_{10}\zeta^2 \tag{3.13}$$

To use the preceding polynomials, central node that consists of the second derivative of the global position coordinates need to be introduced as follows:

$$\mathbf{e}^{i9} = [\partial^2\mathbf{r}^{i9}/(\partial x^i)^2 \quad \partial^2\mathbf{r}^{i9}/(\partial y^i)^2 \quad \partial^2\mathbf{r}^{i9}/(\partial z^i)^2]^T \tag{3.14}$$

Since additional internal element parameters do not need to be introduced to alleviate lockings, complex plasticity failure models, like the Drucker-Prager yield criterion for deformable soil, can be implemented in a straightforward manner [14].

3.3.1 Generalized Elastic Force Formulation

To implement the finite plasticity theory, the Hencky strain measure is utilized to formulate the elasto-plastic forces for the 9-node brick element in Chrono::FEA. The logarithmic strain tensor obtained by the special decomposition of the left Cauchy-Green tensor $\mathbf{B}^e$ is defined as follows:

$$\boldsymbol{\varepsilon}_L^e = \frac{1}{2}\ln(\mathbf{B}^e) = \sum_{i=1}^{3}\ln(\lambda_i)\mathbf{e}_i \otimes \mathbf{e}_i \tag{3.15}$$

where λ_i ($i = 1, 2, 3$) is the i-th eigenvalue of the spatial stretch tensor $\mathbf{V}^e$ defined by the polar decomposition $\mathbf{F}^e = \mathbf{V}^e\mathbf{R}$ and the rotation tensor $\mathbf{R}$. The generalized elastic force vector is then defined using the Kirchhoff stress tensor as follows:

$$\mathbf{Q}_e = \int_V \left(\frac{\partial \mathbf{D}}{\partial \dot{\mathbf{e}}}\right)^T \boldsymbol{\tau}\, dV \tag{3.16}$$

where $\mathbf{D}$ is the deformation rate tensor calculated by:

$$\mathbf{D} = \frac{1}{2}(\mathbf{L} + \mathbf{L}^T)$$ (3.17)

and $\mathbf{L}$ is the velocity gradient tensor as given by $\mathbf{L} = \dot{\mathbf{F}}\mathbf{F}^{-1}$. While the Green-Lagrange strain formulation can be used for elastic solid problems, the inclusion of the Hencky strain formulation allows for a straightforward integration of multiplicative plasticity models of finite strain plasticity theory. As shown in Fig. 3.5, the global position gradient vector tensor $\mathbf{F}$ can be decomposed into elastic and plastic components [14]. This creates an intermediate stress-free state for which a classical return mapping scheme can be used to determine the plastic strain.

3.3.2 Drucker-Prager Failure Model and Return Mapping Algorithm

One of the most common plasticity theories used for the fundamental modeling of terrain response for tire/soil interaction scenarios is the Drucker-Prager Failure Model [3]. The yield criteria for the Drucker-Prager model can be described as the yield surface of a cone in a three-dimensional stress space as shown in Fig. 3.6. The yield function of the Drucker-Prager criterion is as follows: [33]
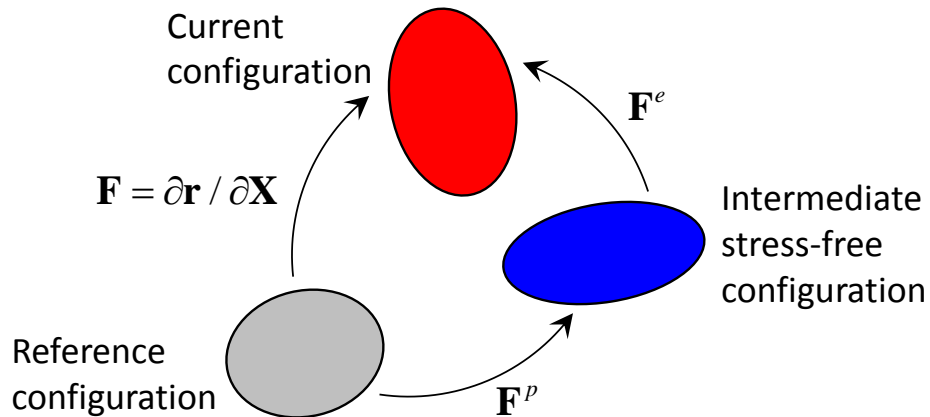
Figure 3.5: Decomposition of position vector gradient tensor for multiplicative plasticity theory
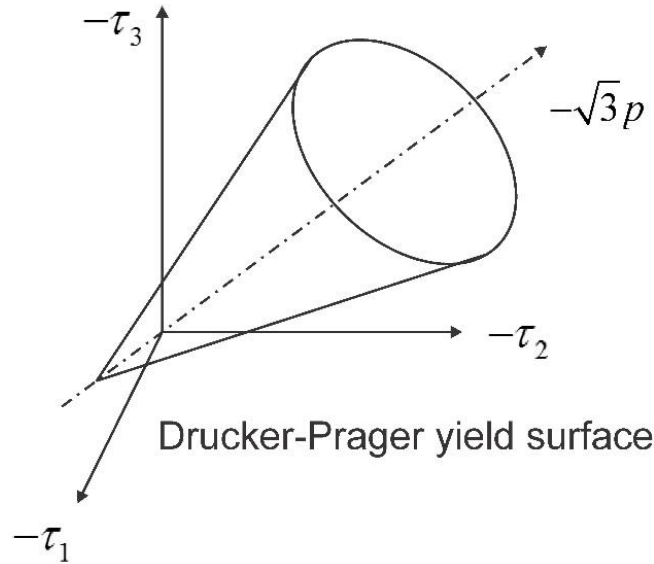
Figure 3.6: Drucker-Prager yield surface for a three-dimensional stress state

$$\Phi = \sqrt{J_2(\mathbf{s})} + \eta p - \xi d \tag{3.18}$$

where $J_2(\mathbf{s}) = \frac{1}{2}\mathbf{s}:\mathbf{s}$; $\mathbf{s}(\boldsymbol{\tau})$ is the deviatoric stress of the Kirchhoff stress tensor defined by

$\mathbf{s}(\boldsymbol{\tau}) = \boldsymbol{\tau} - p(\boldsymbol{\tau})\mathbf{I}$; and $p(\boldsymbol{\tau})$ is the hydrostatic pressure, or mean effective stress, calculated as

$p(\boldsymbol{\tau}) = tr(\boldsymbol{\tau})/3$. The parameters η and ξ are defined using the friction angle β as follows:

$$\eta = \frac{1}{\sqrt{3}}\tan\beta \quad \text{and} \quad \xi = \frac{1}{\sqrt{3}} \tag{3.19}$$

Also, the cohesion d is expressed as a linear function of the equivalent plastic strain multiplied by the plastic hardening slope. The incremental plastic strain is then calculated as a function of the plastic flow vector and subsequently the dilatancy angle φ. To determine if plastic loading occurs, an elastic trial step is first taken. The left Cauchy-Green tensor will be calculated using the following equation: [14]

$$(\mathbf{B}_{n+1}^e)^{\text{trial}} = \mathbf{F}_{n+1}(\mathbf{C}_n^p)^{-1}\mathbf{F}_{n+1}^T \tag{3.20}$$

where $\mathbf{C}_n^p$ denotes the right Cauchy-Green tensor that has been adjust to account for previous plastic strains. The logarithmic elastic strains and the Kirchhoff stress tensor are calculated using the elastic trial step before the yield function is evaluated. In the case that the yield criterion is not met, the right Cauchy-Green tensor and plastic strains will remain the same as the previous step

and the elastic force calculation will consider the Kirchhoff stress tensor due to elastic strains only. Should the yield criterion be satisfied, the plastic strains are determined using a return mapping algorithm that bring the stress state to either the yield cone surface or the apex of the cone, illustrated in Fig. 3.7. For either case, a discrete equation exists to update the elastic and plastic strains and Kirchhoff stress tensor in order to calculate the generalized elasto-plastic force vector with Eq 3.16.

3.3.3 Capped Drucker-Prager Failure Model and Return Mapping Algorithm

A drawback of the Drucker-Prager failure model is that it is unable to demonstrate the effects of soil compaction due to compressive hydrostatic pressure on the plastic deformation. This phenomenon can be considered if the yield surface of the Drucker-Prager model is altered to include an elliptical surface capping the flat face of the cone. This updated yield surface is shown in Fig. 3.8 and the updated yield function is defined as follows: [33]
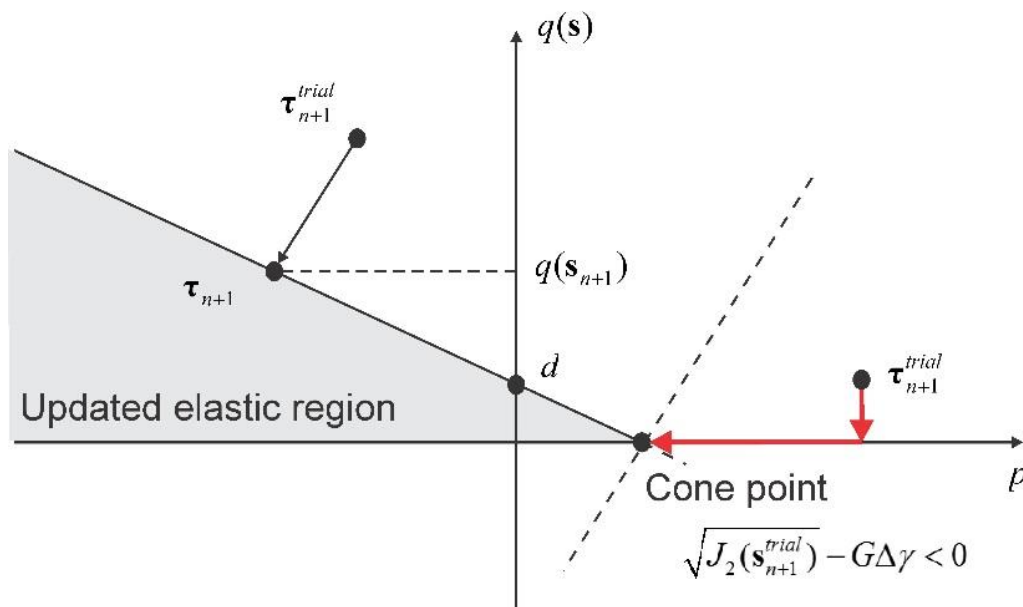
Figure 3.7: Drucker-Prager return mapping diagram on *p-q* plane
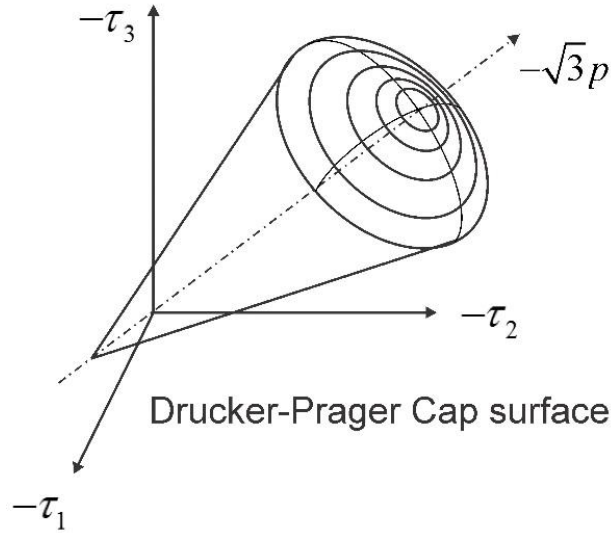
Figure 3.8: Capped Drucker-Prager yield surface for a three-dimensional stress state

$$
\left.
\begin{aligned}
\Phi^a &= \sqrt{J_2(\mathbf{s})} + \eta p - \xi d \\
\Phi^b &= \frac{1}{b^2}\left[p - p_t + a\right]^2 + \left[\frac{q(\mathbf{s})}{M}\right]^2 - a^2
\end{aligned}
\right\}
\tag{3.21}
$$

where Φ^a is the original Drucker-Prager yield function presented in the previous section and Φ^b describes the elliptical cap yield function based on a modified Cam-Clay yield criterion as illustrated in Fig. 3.9. In the preceding equation, $p_t = (\xi/\eta)d$ represents the tensile yield pressure; b is the parameter that defines the cap shape; $M = \sqrt{3}\eta$; and $q(\mathbf{s})$ is the deviatoric stress.
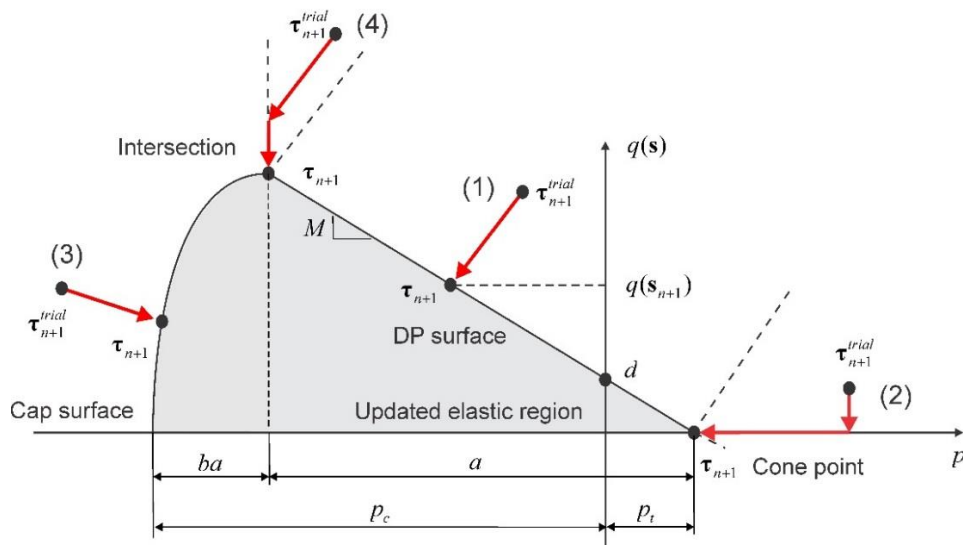
Figure 3.9: Capped Drucker-Prager return mapping diagram on *p-q* plane

In this model, the cohesion is not determined by a linear hardening slope, but rather is represented by change is the cap surface. The hardening parameter a is defined as follows:

$$a(\alpha) = \frac{p_c(\alpha) + p_t}{1 + b} \tag{3.22}$$

where $\alpha \equiv -\varepsilon_v^p$ is the volumetric plastic strain and $p_c(\alpha)$ is the compaction pressure or yield mean effective stress, which can be determined with experimental data of soil compression tests.

While, in the previous model, the return mapping algorithm would bring the stress state to either the cone surface or the apex of the cone, it is possible for the stress state to be returned to the elliptical cap surface and the intersection between the cap and cone surfaces as well for the Capped Drucker-Prager model. In a similar fashion to the previous Drucker-Prager model, this return mapping algorithm is considered for each integration point for every element at each time step in order to determine the updated plastic strains and Kirchhoff stress tensor. A flow chart of the return mapping algorithm of the Capped Drucker-Prager model is illustrated in Fig. 3.10 [14].
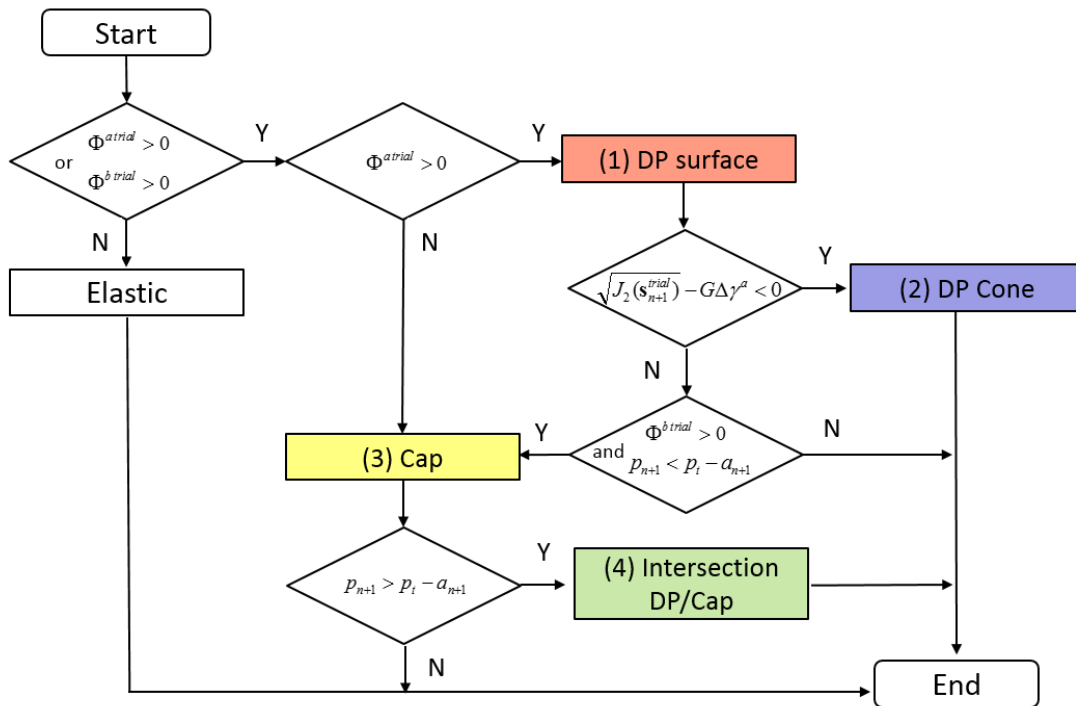
Figure 3.10: Flow chart for the capped Drucker-Prager return mapping algorithm

3.3.4 Implementation of Brick Element into Chrono::FEA

Similar to the integration of the shear deformable shell element discussed in Section 3.2.3, it was necessary for new classes to be added for the addition of the 9-node brick element. Although this element can make use of the preexisting ChNodeFEAxyz class to model the 8 corner nodes of the brick element, there was not a class that was capable to storing the curvature coordinate information needed for the 9-node brick element. This new node class was title "ChNodeFEAcurv" and this was used to describe the three curvature coordinate vectors at the center of each element. Much like the other node classes, this class contains functions to load the state variables and derivatives into the system equations of motion as well as report the current state values. This class is used in conjunction with ChNodeFEAxyz to fully define the nodes for the 9-node brick element. The full inheritance of the new ChNodeFEAcurv class is illustrated in Fig. 3.11.

The addition of the 9-node brick element class required the inclusion of many user options to fully describe the element needed for the simulation. Since this element includes multiple strain formulations as well as multiple plasticity models, there were many considerations made in order to adapt this element into the Chrono::FEA structure. As mentioned before, a finite element class requires functions to calculate the mass matrix, external gravity body force vector, the internal elastic force vector, and the elastic force jacobian matrix. Both the internal force vector calculation and the elastic force jacobian matrix were segmented into separate sections accommodate the different options of strain formulation and plasticity model. First, these functions are split by the strain formulation option, allowing the user to select between the Green-Lagrange and Hencky formulations, neither of these options requiring additional parameters. It is then possible for the user to activate a plastic deformation option using the Hencky strain formulation. From here, it is possible to select the Drucker-Prager or Capped Drucker-Prager plasticity models, each needing a different set of input parameters. The Drucker-Prager model requires a specified cohesion and hardening slope as well as the friction and dilatancy angle in order to fully describe the model. These parameters are also needed for the Capped Drucker-Prager option, as well as parameters to describe the elliptical cap shape. The 9-node brick element must also have a material model, element dimensions, and the list of the corresponding nodes that it is associated with. The full inheritance diagram of the 9-node brick element are shown in Fig. 3.12. Similarly to the shear deformable shell element, the 9-node brick element class inherits from the generic finite element class as well as the external load class applied over the element volume.
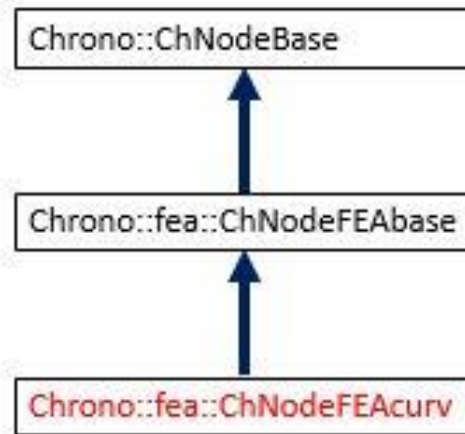
Figure 3.11: Inheritance of the node class containing three-dimensional curvature coordinates in Chrono::FEA
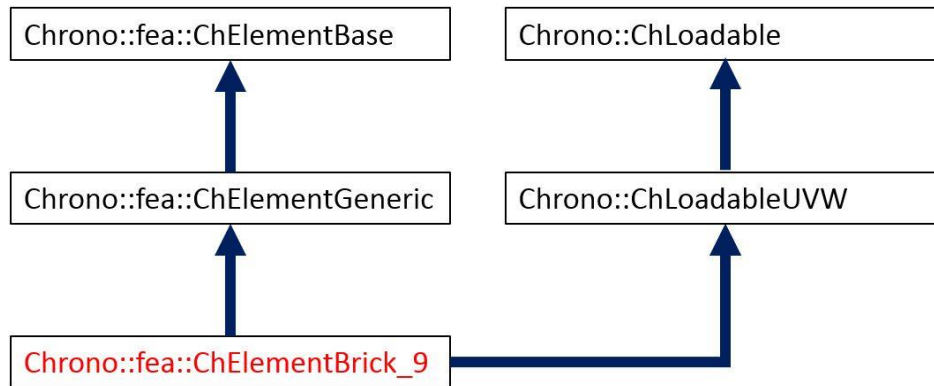
Figure 3.12: Inheritance of 9-node brick element in Chrono::FEA

CHAPTER 4

INTEGRATION OF DEFORMABLE TIRE AND TERRAIN MODELS INTO

CHRONO::VEHICLE

4.1 Introduction

In this chapter, the construction and integration of the deformable tire model and the flexible soil model will be described. There are many considerations that must be made in the design of a physic-based tire model in order to accurately represent the structural tire characteristics. An off-road tire was modeled based on the structural information from commercial off-road tires. An additional key feature of the off-road tire model is the integration of a deformable tread pattern used to interact with off-road terrain models via third-party collision detection algorithms applicable to any surface contact geometries. This chapter will also detail the computational burdens that come with the complex flexible multibody dynamics needed for physics-based vehicle modeling. Several improvements were made to improve the code's numerical efficiency and introduce high performance computing capabilities for large-scale computational models. This is also for more complex vehicle simulations involving fine mesh flexible bodies and multiphysics models.

4.2 Deformable Tire Modeling in Chrono::Vehicle

4.2.1 Flexible Tire Generation Tools

The creation of a deformable tire model using the shear deformable shell element described in Chapter 3 can present many challenges. Important characteristic such as the cross-sectional geometry, the tire size, and material model has a significant impact on the overall tire dynamics as well as the numerical convergence of the system. It is critical that the construction and design be considered thoroughly in order to create an accurate model. To facilitate this, a set of functions were implemented to generalize the tire model creation in a straightforward manner while also satisfying the requirements of the Chrono::Vehicle module. The shell element based tire model was parameterized such that it could be fully defined by the fewest amount of data from the user.

The creation of the flexible tire body in Chrono::Vehicle is performed during the initialization of each shear deformable shell element based tire. This process relies on user-provided model parameters through a .json input file. The first step in generating the flexible tire body is the definition of the geometry of the tire cross-section. This process can be difficult because

a tire shape is more complex than that can be simplified by basic algebraic expressions and models will give unrealistic results when generalized into simple shapes. To fully describe the detailed tire geometry, a cubic spline interpolation are used to describe the tire cross-section geometry. The user must provide this profile data points as a series of vector coordinates. A spline polynomial is created from the data points along the circumference and nominal width of the tire. ChNodeFEAxyzD type nodes are created along the profile, where the transverse gradient coordinates are defined as a vector normal to the tangent of the cubic spline at the given position [14]. The node creation process across the tire width is then repeated on a plane rotated forward around the circumferential of the tire. The number of nodes created in the circumferential and width direction is determined by the element mesh resolution provided by the user. Once the nodes has been created, the shear deformable shell elements are constructed from the existing nodes, following the same numbering convention. Here, the layered material models for the shell element are defined based on user input information. Due to the inhomogeneous nature of the structure of a tire, it would not be appropriate to model the entire body with a single material model. In order to allow for a more accurate representation of the materials properties across a tire profile, it is possible to create sections of elements that share the same materials. These sections are symmetric across the tire width and circumference and allow for certain areas of the tire to be modeled with greater thickness, different combinations of materials, and various configurations of orthotropic material properties. Again, this information is provided through an input file that specifies the materials used and their properties, number of sections, and the element layer properties for each section. The tire generation tools in Chrono::Vehicle can then organize this information and apply the correct material and layer models to the corresponding shell elements in the tire. Additional parameters provided by the input file include the overall tire radius, rim radius, rim width, structural damping coefficient, and tire air pressure.

Once the flexible tire body has been fully defined and added to the Chrono::Vehicle system, it must be integrated and constrained to the full vehicle model. The outer most set of nodes on each end of the tire profile is rigidly connected to wheel body of the wheeled vehicle system by imposing kinematic constraints. The nodes are constrained using the classes "ChLinkPointFrame" and "ChLinkDirFrame" which constrains the global position vector and transverse gradient vector of each of the end nodes, respectively, as shown below:

$$g(\mathbf{q},t) = \left\{ \begin{array}{c} \mathbf{r}_p^b - \mathbf{r}_p^n \\ \overline{\mathbf{v}}_c - (\mathbf{A}^b)^T \dfrac{\partial \mathbf{r}}{\partial z} \end{array} \right\} = 0 \tag{4.1}$$

where $\mathbf{r}_p^b$ is the global position vector of the constraint definition point P on the rigid rim body, while $\mathbf{r}_p^n$ is the global position vector for the ChNodeFEAxyzD node of the shell element. In the second equation, $\overline{\mathbf{v}}_c$ is a directional vector defined in the rigid rim body coordinate system at the constraint definition point, and $\mathbf{A}^b$ represents the transformation matrix to project the transverse gradient coordinate vector $\partial \mathbf{r}/\partial z$ of the shell element onto the rigid rim body coordinate system. In addition to the constraints, a distributed load is applied to the inner surface of the shear deformable shell elements for modeling internal air pressure using a load class derived from ChLoadbleUV. This new class titled "ChLoaderPressure" applies a constant pressure to the shell element surface using a Gaussian integration technique. A contact surface is also created for each deformable tire model that requires the user to prescribe a collision detection radius as well as contact stiffness, damping, friction, and adhesion coefficients. After this process has been completed for a single tire, the framework is copied to create the remaining tire for the wheeled vehicle system. The tire model is rotated 180 degrees about the vertical axis if the tire changes to the opposite side of the vehicle in order to enforce symmetry across the vehicle system. This is done because the layered orthotropic materials of the shear deformable shell element tire can results in asymmetric deformation across the width of each tire. Rotating the tire on the opposite side of the vehicle helps balance the overall vehicle.

4.2.2 Structural Tire Characteristic for Off-Road Tire

Using the tire generation tools described in the previous subsection, an off-road tire was constructed in Chrono::Vehicle. This tire model was created with the purpose of being a general use tool for validation and testing. The design of the model was based on the cross-section and materials of commercial off-road tires (235/75R15). It is important to use a model that can be easily represented by layered material models without being excessively computationally expensive. As explained in Chapter 3, the generalized elastic force vector and the elastic force Jacobian matrix calculations for the laminated composite shell element are repeated for each layer

in the element. Therefore, the computational time for the elastic force evaluation will dramatically increase with the more layers that are needed to describe the tire material.

As discussed in the subsection above, the deformable tire model is broken up into several material sections that allow for the modeling of the changing material properties across the tire profile. For the purposes of this model, three material sections were chosen. A section representing the bead of the tire was defined on the outer edges of the cross-section. Another section was used to represent the sidewall of the tire as the shape moves further from the center. Finally, a tread section was created to model the area of the tire that comes in contact with the terrain. A cut cross-sectional profile of a commercial tire showing the changing material composition and thickness along the width as well as the fully constructed shell element tire model are illustrated in Fig. 4.1. Three materials models created for the layer modeling; these materials were an isotropic rubber material model to serve as the composite matrix, a tire carcass material model consisting of polyester cords embedded in rubber, and a steel belt material model to represent the orthotropic fiber reinforced rubber. An outline of the layer configuration for the off-road tire is described in Fig. 4.2.
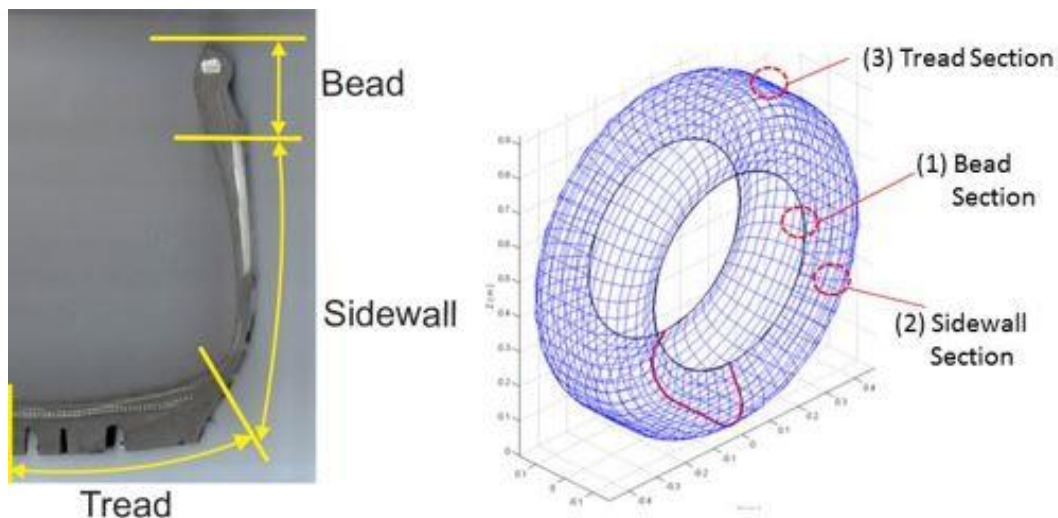
Figure 4.1: (Left) A cut off-road tire cross section with three distinct material sections identified. (Right) The diagram of the structure of the off-road tire model constructed from shear deformable shell elements
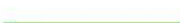
(1) Bead section	Cord angle	Thickness
———— Carcass	$\alpha = 90°$	$h = 0.5mm$
———— Rubber	$\alpha = 0°$	$h = 5.0mm$
———— Carcass	$\alpha = 90°$	$h = 0.5mm$

(2) Sidewall section		
———— Carcass	$\alpha = 90°$	$h = 0.5mm$
———— Rubber	$\alpha = 0°$	$h = 0.1mm$
———— Carcass	$\alpha = 90°$	$h = 0.5mm$

(3) Tread section		
———— Rubber	$\alpha = 0°$	$h = 1.0mm$
———— Belt	$\alpha = -20°$	$h = 0.3mm$
———— Belt	$\alpha = 20°$	$h = 0.3mm$
———— Carcass	$\alpha = 90°$	$h = 0.5mm$

Figure 4.2: A tabular representation of the layer configuration for the material sections used in the deformable off-road tire model

4.2.3 Modeling of Tread Block of Tire

For off-road tire applications, the tire tread pattern can have a significant impact on the interaction with the deformable terrain. As a tire encounters uneven or deformable ground, the presence of tread is essential for gaining the needed traction to move the vehicle forward. The effect of the tread pattern can often be neglected in the case of on-road tire simulation on a rigid ground since the friction and slip curve for cornering and braking tire forces can be measured accurately and used to predict the overall tire dynamics behavior. This is reflected in the design of street tires with more basic tread patterns that are only needed to prevent hydroplaning and maintain a large contact patch with the road to improve overall traction and wear rate. The tread pattern for off-road tires consists of much larger rubber blocks and is designed to allow for the flow of materials such as sand, snow, or mud. Therefore it is important to create a method to integrate a tread pattern onto the shear deformable shell element off-road tire model.

In order to create a model that can interact with deformable terrain models, a sophisticated collision detection algorithm applicable to the complex tread pattern is needed such that contact forces acting on deformable tread blocks can be transferred to the deformable structural tire model. It is possible to define rigid tread contact surfaces to the plane of the shell elements of the tire to account for the tread pattern without increasing the model dimensionality [34]. However, the tread block deformation is neglected, thus a deformable tread model was created using the co-rotational finite element approach in Chrono::FEA to be integrated with the deformable tire model. The 4-node co-rotational tetrahedral element is able to be connected easily to the 4 node brick element by defining the tetrahedral elements with mutual connectivity to the existing finite element nodes from the deformable tire. An exception was made to permit volumetric elements, like the brick elements, hexahedral elements, and tetrahedral elements to utilize the ChNodeFEAxyzD node class, by extracting only the global position coordinates. This connectivity between the shear deformable shell elements and the co-rotational tetrahedral elements is illustrated in Fig. 4.3. This allows the shell elements and the tetrahedral elements to share the same node objects, although the shell elements require the transverse gradient coordinate vectors. Using this method a model of the tread pattern for the reference tire model (Goodyear Wrangler MT) was created as also shown in Fig. 4.3.

Figure 4.3: (Left) The formation of solid tread blocks by using the same nodes to describe the shear deformable shell elements and the co-rotational elements connectivity. (Middle) The tread pattern of a sample off-road tire, the Goodyear Wrangler MT. (Right) The emulation of the of the sample off-road tire tread pattern created from co-rotational tetrahedral elements on the shear deformable shell element tire model

4.2.4 Tire/Terrain Collision Detection and Contact Methods

It is of no surprise that the interaction between the elements that comprise the deformable tire model and the various terrain models will have a large impact on the overall tire dynamics. The simulation must have a sophisticated collision detection algorithm and contact force evaluation to produce realistic tire force characteristics. For collision detection, Chrono uses the open-source Bullet Physics library as a third party addition. This is a very common physics engine that is capable of rigid body dynamics and soft body dynamics simulation. However, the code is modular and it is possible to incorporate only certain components into other simulation framework. In this case, Chrono relies on the robust collision detection shapes and algorithms provided by Bullet Physics [34]. With this library, objects in Chrono can be represented as a set of primitive collision shapes. These collision shapes include spheres, boxes, cylinders, cones, convex hulls, and triangular meshes. In the case of the off-road tire model, the collision shape required will depend on the application. In the case that the deformable tire is running over a continuous rigid ground body, the contact surface of the tire is defined by nodal contact. This applies spherical collision shapes to each of the nodes of the deformable tire model and the contact forces are applied

at the nodal level. This can be done since the tire model is contact with a large continuous body, such that there are few opportunities for the collision between the tire and ground bodies to be missed.

On the other hand, in the case that the tire is interacting with other finite element meshes or granular terrain, the surface of the tire is defined by triangular mesh elements. This allows for the tire model to interact with smaller collision objects, like DEM particles, without them moving past the more coarse nodal contact surface undetected. The assignment of the spherical and triangular mesh collision shapes on the deformable tire model can be seen in Fig. 4.4 to create nodal and surface mesh contact detection. Once these objects are applied to the bodies in Chrono, a board phase sweep of the collision shapes is performed using an axis aligned bounding box method to determine if there is the potential for objects to be colliding [35]. If this criterion is met then a localized collision detection is performed by calculating the nearest point between two collision shapes. If there is penetration between the shapes, then the contact force calculation is performed.

As described in Chapter 2, the contact force characteristics can be described using a penalty-based approach or a complementarity-based method. However, an implicit time integration scheme is required for the simulation of the finite element tire and terrain models, and use of penalty approach leads to a straight forward implementation. Thus, the penalty-based
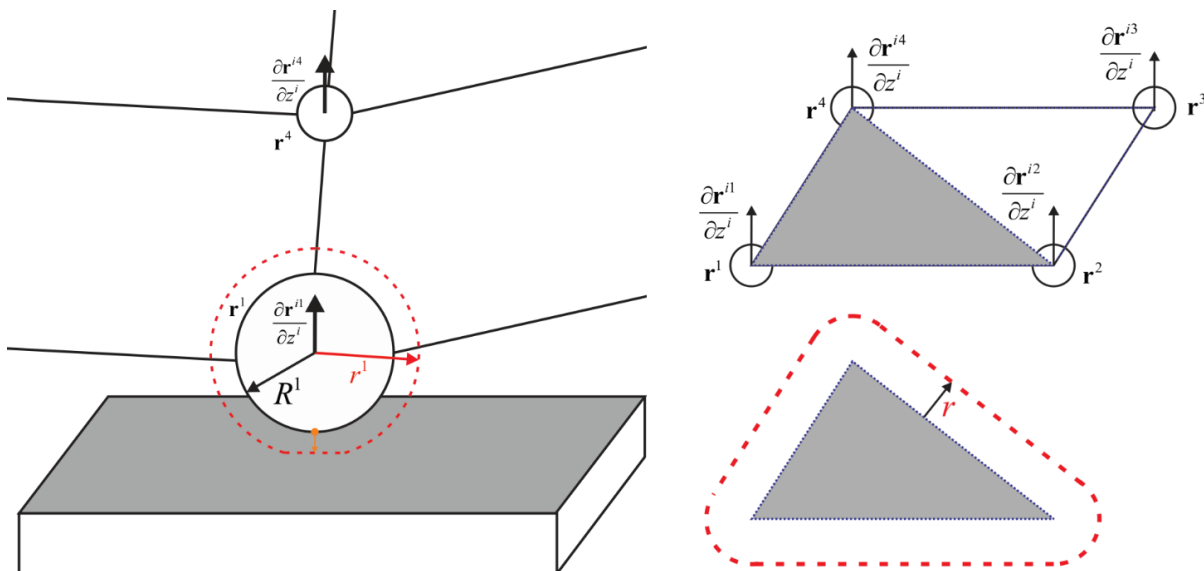
Figure 4.4: (Left) The application of spherical collision shapes is applied to the ChNodeFEAxyzD nodes of the deformable tire model to create a nodal-based contact surface. (Right) The discretization of the shear deformable shell element into triangular surface elements for collision detection

approach is used for modeling contact forces for the mobility simulations. With this in mind, the interpenetration of the flexible tire body must be considered in the design of the tire model. Using a penalty formulation, the normal contact force is evaluated as the following equation:

$$\mathbf{F}_n = k_n \delta_n - \gamma_n \mathbf{v} \|\delta_n\| \tag{4.2}$$

where k_n is the contact stiffness coefficient, γ_n is the contact damping coefficient, δ_n is the normal interpenetration, and $\mathbf{v}$ is the relative velocity. The tangential contact forces are defined using a slip-dependent Coulomb friction model as follows:

$$\mathbf{F}_t = \frac{2}{\pi} \mu_0 \tan^{-1}(5.0\mathbf{v}) \mathbf{F}_n \tag{4.3}$$

where μ_0 is the saturated Coulomb friction coefficient for the large slip cases.

4.2.5 Tire Class Structure and Implementation in Chrono::Vehicle

The deformable tire model has been integrated into Chrono::Vehicle as a series of specific classes. To be integrated into a standard wheeled vehicle system, the shear deformable shell element tire model must inherit from the "ChTire" class. In order to meet the requirements of the base class, the new tire class must include functions to report the tire radius, slip angle, camber angle, and tire forces as the basic properties of a tire model in Chrono::Vehicle. A new subclass was created which will define the characteristics of deformable tires. This class, "ChDeformableTire" contains functions to set the material properties, contact parameters, and internal air pressure magnitude. This class can not only be used for the shear deformable shell element tire model, but other finite element based tires as well. It is also noticed here that the contact surface is set, which applies the Bullet collision shapes and detection radii to the surface of the deformable tire. It is at another class below the deformable tire class, that the construction of the shear deformable shell elements, based on the user-provided input file, is performed and the newly created flexible tire body is constrained to the rigid rim. This class, known as "ANCFTire", has the capability to store the information needed to fully define the shell element, including the material and layer properties for the laminated composite shell, and to apply constraints on the global position coordinates and transverse gradient coordinates of the ChNodeFEAxyzD nodes. A diagram of the full inheritance of the shell element based tire model class is summarized in Fig. 4.5.

4.3 Continuum Based Soil Modeling in Chrono::Vehicle

4.3.1 Continuum Soil Model and Parameters

The continuum based soil model was constructed from the 9-node brick elements described in the previous chapter. The process of creating the deformable soil model in Chrono::Vehicle has been simplified into a few functions. The specification of the material properties and the plasticity model such as the capped Drucker-Prager failure model are performed first as it is the most important part of describing the soil model. A function is used to store the basic elastic material properties, such as density, Young's modulus, and Poisson's ratio, as well as the parameters needed to detail the plastic behavior of the model. The user can then enter the type of plasticity model as well as the parameters needed to describe the evaluation of the plastic strain. Once this is provided, a function is used to create the flexible body from the finite element mesh. The model itself is created as a solid terrain block that is uniform in size and shape, which can easily be described by simple dimensions. The element dimensions are then determined by the total terrain size and the number of elements in a given direction. The solid soil body is then created following the procedure explained in Chapter 3. After the mesh has been added to the system and constrained, the contact surface is created and applied to the outer faces of the body.

4.3.2 Terrain Class Structure and Implementation in Chrono::Vehicle

The continuum based finite element terrain model was incorporated into Chrono::Vehicle as a subclass of the terrain models in "ChTerrain". This base terrain class contains functions to describe the height of the terrain and the unit normal vector to the top surface of the terrain at a
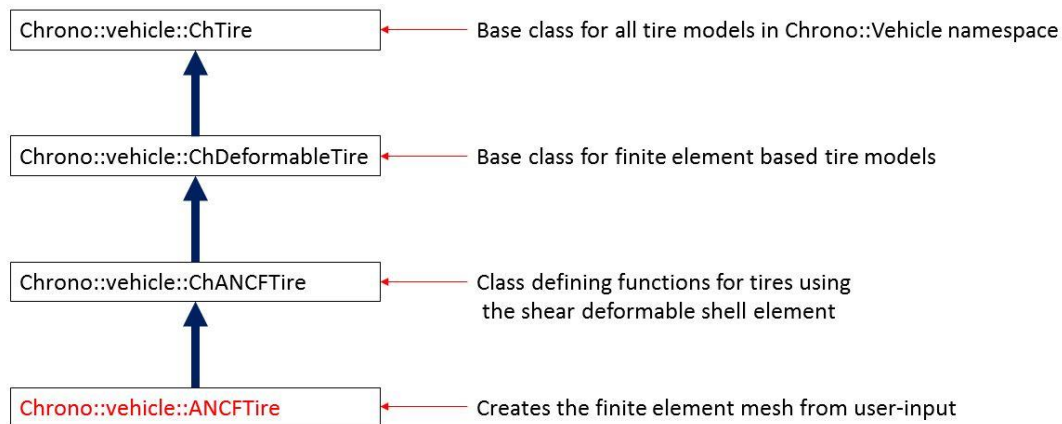
Figure 4.5: Inheritance tree of the tire class based of the shear deformable shell elements in Chrono::Vehicle

given point. A new class was created for the specification of the terrain based on the 9-node brick element. This class became titled "FEADeformableTerrain" and consists of functions to parameterize the elasto-plastic properties of the soil and constructs the flexible body from the 9-node brick elements. In the definition of the 9-node brick elements, a function was created to apply the material properties as well as define the plasticity model to be used along with the necessary parameter information. It is also in this class that boundary conditions are applied to the bottom and sides of the terrain block at the nodal level. The contact properties for the deformable terrain are then applied to the finite element mesh. Much like the deformable tire model, the terrain utilizes the Bullet collision shapes of spheres to define a nodal contact surface or a triangular mesh, which will outline the surface of the terrain block. In the case of the deformable terrain, the nodal contact surface can prove to have more issues modeling complex tire geometries due to a smaller number of contact shapes per element and smaller collision detection radius. This could reduce the effect of tread pattern and small variations in the tire shape. Therefore it is more crucial that the triangular surface mesh be used to support the collision detection of deformable terrain. A diagram of the inheritance for the finite element deformable terrain class is given in Fig. 4.6.

4.4 Computational Time Improvement

4.4.1 Performance Improvement Methods

Sophisticated vehicle dynamics simulation using finite element based tire and terrain models can become increasingly computationally expensive as the model gets more complex. With the addition of the finite element based deformable tire and terrain modeling techniques, the problem dimensionality will drastically increase with an increase in the mesh resolution of the flexible bodies. In order to cope with these large dimensional models and improve the performance, a number of measures were added to the solution procedure in Chrono. Extensive
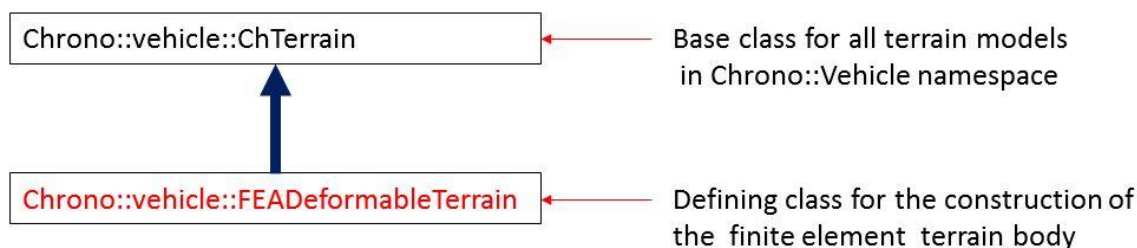
Figure 4.6: Inheritance tree of the deformable terrain class based on the 9-node brick elements in Chrono::Vehicle

code profiling was performed on multiple simulation cases to identify bottlenecks the computation time. From these studies, it was clear that the evaluations of the generalized elastic forces and elastic force Jacobian are the occupying the most amount of time.

Use of OpenMP: The elastic force evaluation process can be enhanced by the application of OpenMP (Open Multi-Processing) parallelization to handle the evaluation of multiple elements at the same time. This was extended to the elastic force functions within the element loop. This technique can split the following evaluation function to be performed by a set number of CPU cores. The number of threads can be set from the main function from the available number of processors. This can theoretically improve the computation time by a factor of the number of available processors, however this scalability is not obtainable. The utilization of OpenMP parallelization can take time to divide the processes between the cores and this overhead will reduce its effectiveness. Despite these imperfections, the overall impact of the OpenMP method on the performance of elastic force evaluation is very positive.

Use of AVX: One of the sources of the computational burden in the elastic force vector and Jacobian matrix calculation is the presence of large matrix multiplication operations. In case of the shear deformable shell element and the 9-node brick element the Jacobian matrix will have a large dimensionality proportional to the degrees of freedom of the element. To improve the performance of these calculations Advanced Vector Extensions (AVX) was implemented for the calculation of the elastic force vector and Jacobian matrix components at every Gaussian point. This process allows single instruction multiple data (SIMD) operations to be performed at a faster rate by processing multiple pieces of data at once [36]. This means that the scalar operations between the entries of large matrices can be processed simultaneously.

4.4.2 High Performance Computing

In addition to the performance enhancements discussed in the previous section, Chrono has the capability for high performance computing. The Chrono::Parallel module was created for the application of large scale parallelization for extremely large scale problems, such as granular terrain with DEM soil or fluid/solid interaction using SPH. This framework allows for the division of the solution procedure across multi-core clusters as well as graphical processing units (GPU). Similarly to the AVX methodology, the GPU architecture supports the execution of SIMDs to perform operations on the elements that comprise a large dimensional problem [13]. To

accomplish this, the variables for the equations of motion are vectorized for organization within the parallel structure. The external forces are gathered such that they are applied to the bodies as point forces and torques on the center of rigid bodies and as point loads at the nodes of flexible bodies. Because the analysis of finite element bodies requires a smaller time step size than DEM or FSI systems, simulations that contain a mixture of flexible bodies and multi-physics methods are integrated over time at different rates. This allows the dynamics of the deformable bodies to be solved more frequently than the multi-physics components, so that time will not be wasted on the over-analysis of discrete elements.

4.5 Deformable Tires and Soil Interaction in Chrono::Vehicle

With the extension of the deformable tire and soil models integrated into the Chrono::Vehicle module, an interface must be created to allow these new designs to interact with other vehicle components. The shear deformable tire model can be used on a variety of terrain models. As stated in an earlier section, the deformable tire utilizes either a nodal contact surface or a triangular mesh contact surface in order to detect collision with other physics objects. Using a penalty based contact approach, the tire is able impact off solid rigid objects, finite element surfaces, and discrete element particles. With this capability, the tire can be dropped, rolled, and driven across terrains of any shape that consists of those bodies. An example of the tire-terrain interaction using the triangular mesh collision shape for mesh to mesh contact is shown in Fig. 4.7.

$$\mathbf{F}_n^{ij} = f\left(\bar{R}, \delta_n^{ij}\right)\left(k_n \mathbf{u}_n^{ij} - \gamma_n \bar{m} \mathbf{v}_n^{ij}\right)$$
$$\mathbf{F}_t^{ij} = f\left(\bar{R}, \delta_n^{ij}\right)\left(k_t \mathbf{u}_t^{ij} - \gamma_t \bar{m} \mathbf{v}_t^{ij}\right)$$
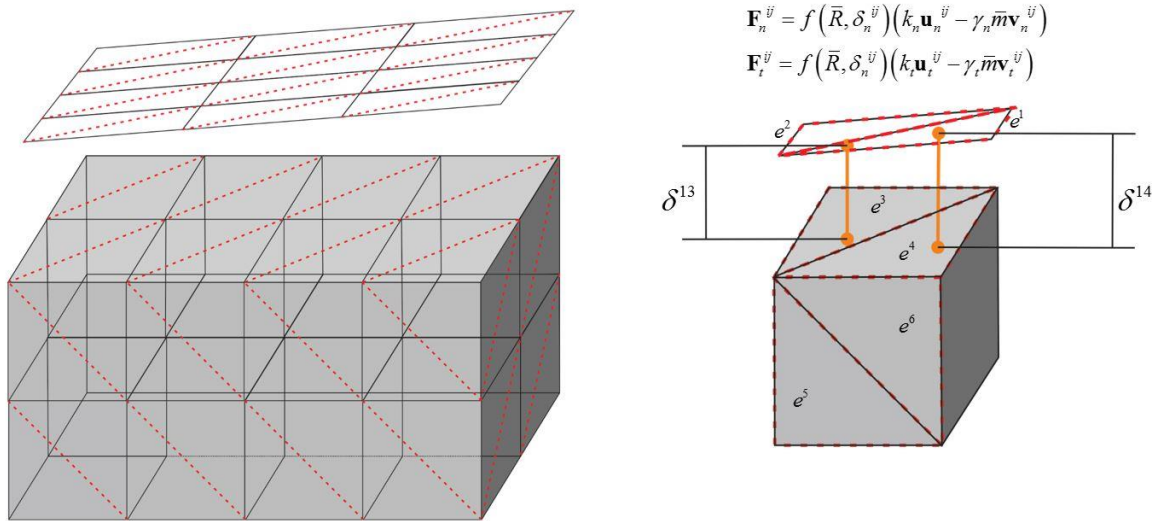
Figure 4.7: Interaction between the triangular mesh contact surfaces for the deformable tire and soil models using a penalty contact method

CHAPTER 5

NUMERICAL EXAMPLES AND CODE VERIFICATION

5.1 Introduction

This chapter will demonstrate the code verification of the newly implemented shear deformable shell element and the 9-node brick element in Chrono. The capabilities of the elements will be presented compared to reference results obtained using the in-house flexible multibody dynamics code and commercial finite element codes for various benchmark problems. Additionally, numerical examples of the deformable tire model and soil model will be explained in this chapter. Lastly, this chapter will detail the impact of the computational performance improvement techniques that were described in the previous chapter.

5.2 Shear Deformable Shell Element Examples

5.2.1 Cantilevered Plate Subjected to a Point Force

The performance of the shear deformable shell element in Chrono was first tested using a static deformation scenario of a cantilevered plate subjected to a point force at the far corner as discussed in the literature [14]. The square plate has a height and width of 1.0 m and the thickness is assumed to be 0.01 m. The plate is composed of isotropic elastic material with a Young's modulus of $E = 2.1 \times 10^8$ Pa and a Poisson's ratio of $\nu = 0.3$. The cantilevered boundary conditions are applied to the nodes of the shell elements in Chrono::FEA. By disabling the variables of these nodes, the global position coordinates and transverse gradient coordinates are removed from the equations of motions and are fixed in the global system. The vertical load applied to the corner of the plate is assumed to be 50 N [14]. A diagram of the cantilevered plate in its reference configuration and its static deformed state are displayed in Fig. 5.1. The vertical tip displacement of the plate was measured for cases of increasing number of elements, which will remove inaccurate mesh stiffness from the system. The static results were compared to a reference solution obtained by a fine mesh of 100x100 shell elements (SHELL181) in ANSYS. The calculated error is shown as a function of the element resolution in Fig. 5.2. This numerical convergence curve is compare to that of the ANSYS 4-node shell element as well as the same shear deformable element presented in the paper [14]. It is observed from this figure that an ideal linear rate of convergence of the finite element solution is achieved by the shell element implemented in Chrono::FEA.
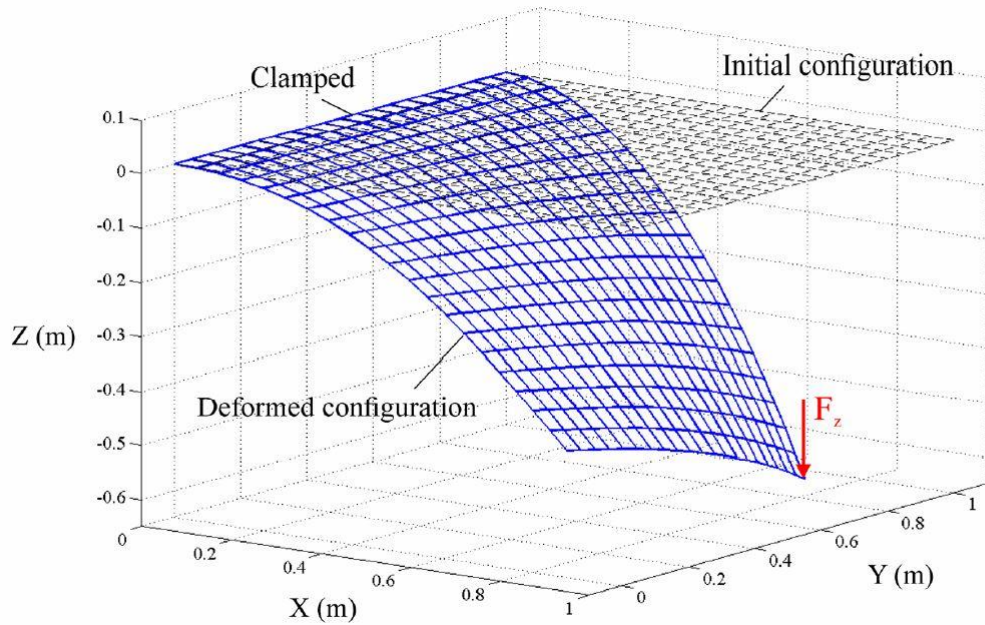
Figure 5.1: Diagram of the cantilevered flat plate comprised of shear deformable shell elements subjected to a point force [14]
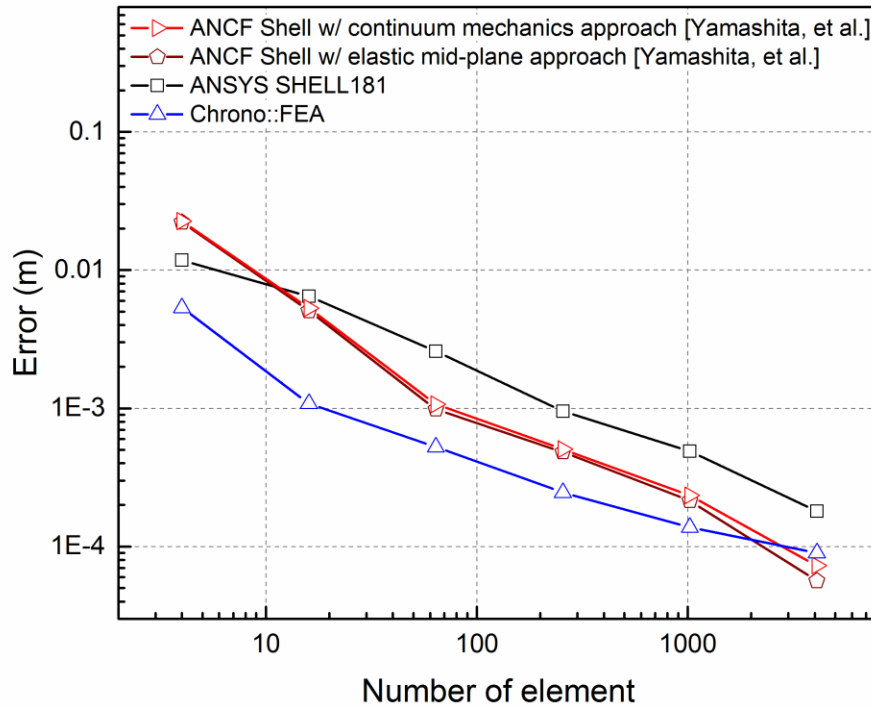
Figure 5.2: The numerical convergence of the vertical tip displacement of the shell element plate example [14]

5.2.2 Cantilevered Quarter Cylinder with Laminated Composite Material

In order to demonstrate the capability of the composite material model implemented in the shear deformable shell element, a quarter cylinder cantilevered plate was modeled under a single point load as in the literature [14]. This initially curved shell is comprised of two layers in a balanced and symmetric laminate configuration, such that the ply angles of the fiber in the laminae are +/- 20°. The curved configuration of the plate has a radius of 1.0 m and it is 1.0 m in width and 0.01 m in thickness, which is split into 0.005 m per composite layer. A constant vertical point load of 10 N is applied to the upper corner of the shell as shown in Fig. 5.3. The Young's modulus of the fiber direction and the matrix for the composite layers are $E_x = 2.0 \times 10^8$ Pa and $E_y = E_z = 1.0 \times 10^8$ Pa, respectively. The respective shear modulus of rigidity and Poisson's ratio are given as $G_x = G_y = G_z = 3.84615 \times 10^7$ Pa and $v_{xy} = v_{xz} = v_{yz} = 0.3$. The equilibrium vertical tip displacement was also recorded for cases of various element resolution and compared to the reference solution acquired with a 100x100 shell element mesh (SHELL181) in ANSYS. The numerical convergence for this benchmark case can be seen in Fig. 5.4. These results also show a linear convergence rate for the laminated composite shell element in Chrono::FEA.
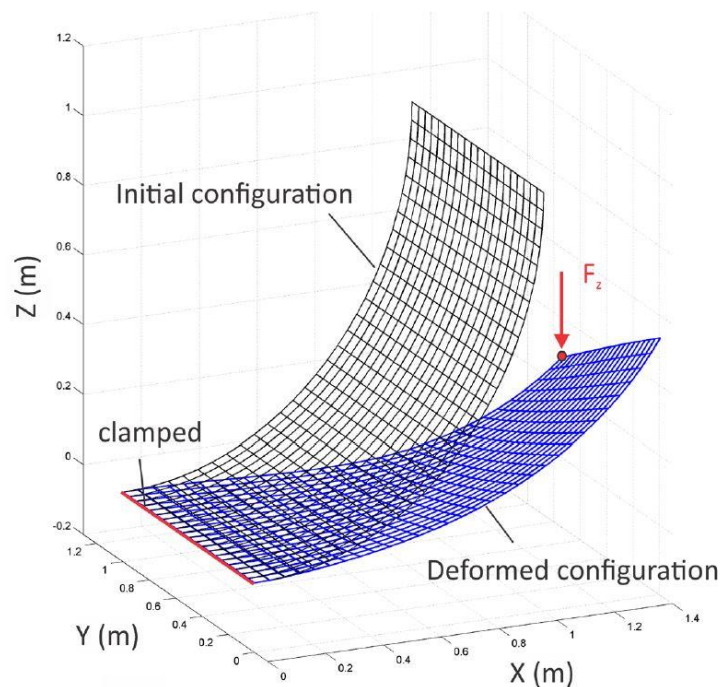
Figure 5.3: Diagram of the laminated composite quarter cylinder cantilevered plate of shell elements subjected to a vertical point load [14]
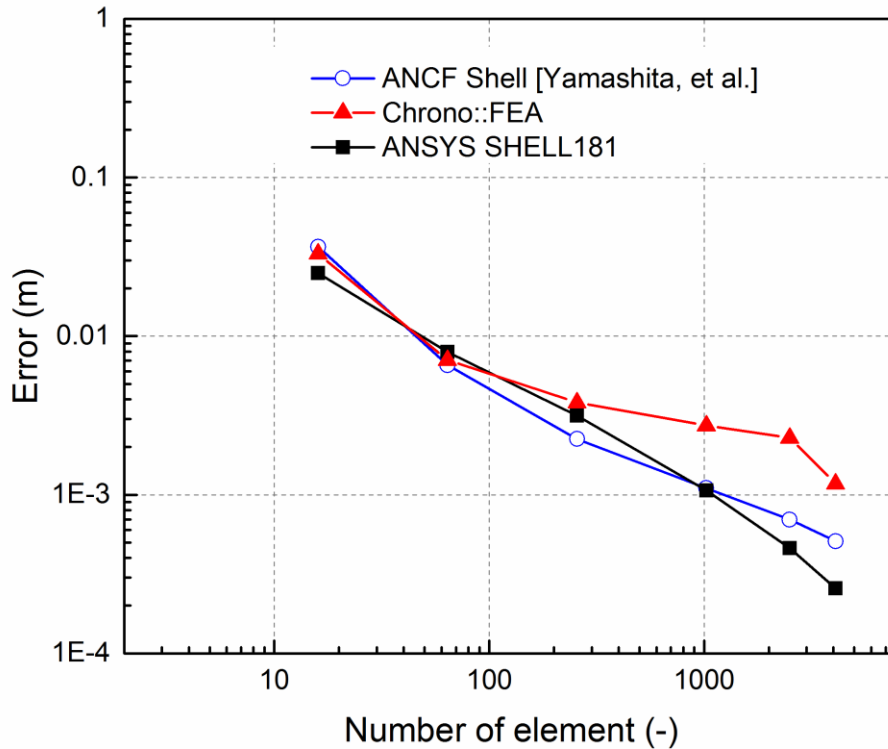
Figure 5.4: Convergence of the laminated composite quarter cylinder comprised of the shear deformable shell element

5.3 9-Node Brick Element Examples

5.3.1 Solid Cantilevered Plate Subjected to a Point Force

The large deformation capabilities of the 9-node brick elements were demonstrated with a test similarly performed by the shear deformable shell element. A flat plat was constructed from the newly integrated 9-node brick elements with only one element representing the plate thickness. In this example the plate shared the same dimensions of the plate in the section above; that is a length of 1.0 m, a width of 1.0 m, and a thickness of 0.01 m. The Young's modulus for the elastic material is $E = 2.1 \times 10^8$ Pa and the Poisson's ratio is $\nu = 0.3$. A point load of 50 N is applied on the far corner of the plate, opposite of the cantilevered boundary condition as shown in Fig. 5.1. The vertical tip node displacement for the static system was determined for increasingly fine element meshes and were compared to a reference solution obtained by ANSYS with a 100x100 brick element mesh (Solid185). The numerical convergence of the tip displacement error is shown

as a function of the mesh resolution in Fig 5.5. This compares the Chrono::FEA implementation against an in-house flexible multibody dynamics code [14] as well as ANSYS. These results demonstrate a quadratic convergence rate for the 9-node brick element for large deformation of elastic materials.

5.3.2 Axially Loaded Solid Beam with Drucker-Prager Plasticity Model

The elasto-plastic behavior of the 9-node brick element was validated by a simple axially loaded cantilevered beam. The beam was comprised of only a single row of 20 brick elements in the axial direction. The beam is 1.0 m long in the axial direction and has a width and height of 0.05 m. The loading condition applied to the beam is a harmonic function defined as $F(t) = 300\sin(\pi t)$ N that is distributed over the nodes at the free end of the beam as illustrated in Fig. 5.6. The elastic properties of the elements include the Young's module, Poisson's ratio, and density of $E = 1.0 \times 10^7$ Pa, $v = 0.3$, and $\rho = 7850 \, kg/m^3$, respectively. The Drucker-Prager model is used to define the plastic deformation of the beam. To describe this the plasticity model, the yield stress
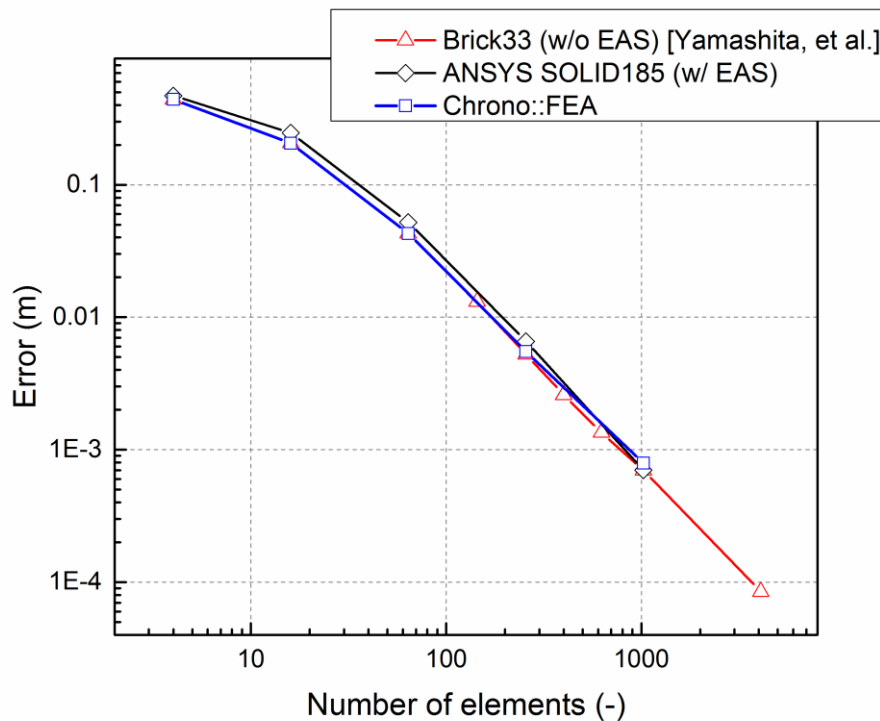
Figure 5.5: The numerical convergence of the tip node displacement of the cantilevered plate of brick elements [14]

and hardening slope are assumed to be $\sigma_y = 1.0 \times 10^5$ Pa and $H = 5.0 \times 10^5$ Pa, respectively. For the following numerical example, three scenarios were considered using two different friction angles and dilatancy angles. The time history of the beam tip axial displacement is collected for a cycle of loading and unloading. The numerical results collected in Chrono::FEA were compared to an equivalent dynamic model in ABAQUS. The results for this uniaxial tensile test, shown in Fig. 5.7, agree very well between the Chrono::FEA and ABAQUS software.

$$F(t) = 300 \sin(\pi t) \text{ N}$$
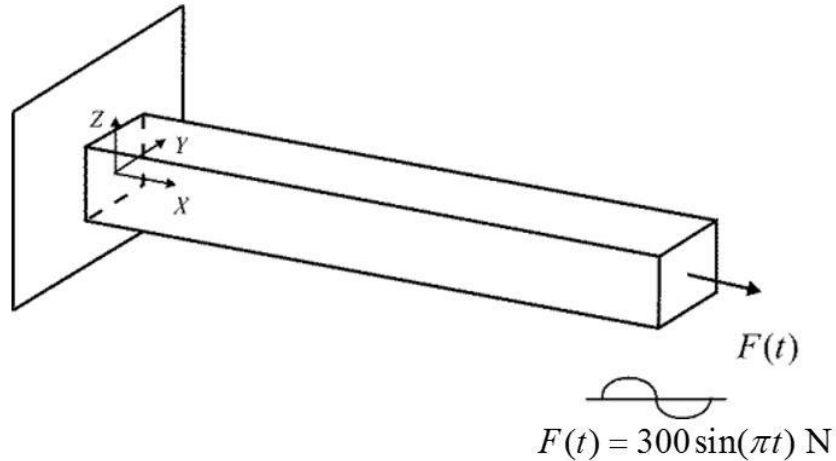
Figure 5.6: A diagram of the cantilevered plastic beam consisting of 9-node brick elements under an axial harmonic loading condition
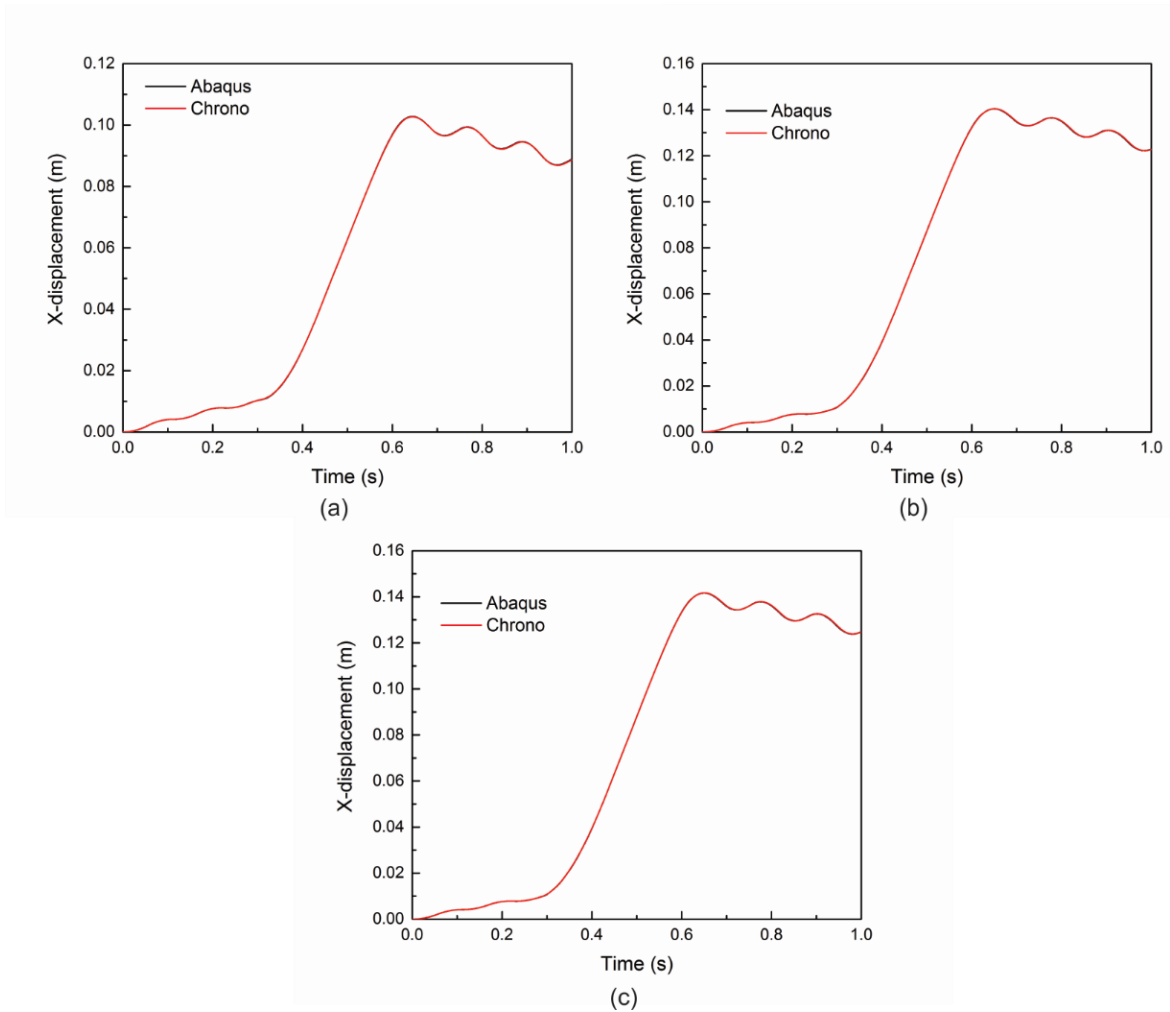
Figure 5.7: The time history results of the axially loaded plastic beams obtained using Abaqus and Chrono::FEA. Each model uses the Drucker-Prager plasticity formulation with a friction angle and dilatancy angle of (a) $\beta = 0.0°, \phi = 0.0°$, (b) $\beta = 10.0°, \phi = 0.0°$, and (c) $\beta = 10.0°, \phi = 10.0°$, respectively

5.3.3 Plastic Soil Punch Test

An example of the finite element soil model was created to test the accuracy of the plastic deformation of the brick elements due to contact with a rigid object. The Capped Drucker-Prager plasticity model was used to model the soil, which would make contact with a rigid punch block being forced into the top of the soil. The rigid box has the dimensions of 0.2 m in length, 0.2 m in width, and 0.1 m in height. It is forced into the soil with a harmonic loading function of $-27000\sin(\pi t)$ N. This punch block is initially placed above the center of the soil patch, which has the dimensions of 0.48 m in length, 0.48 m in width, and 0.6 m in height. The soil has an

element mesh resolution of 12x12x8 elements in the length, width, and height respectively. The lowest plane of nodes is fixed in the initial configuration to represent the bottom of the soil and the sides of the soil model were also fixed to prevent excessive outward deformation. A diagram of this example can be seen in Fig. 5.8. The elastic properties of the soil include a Young's modulus of $E = 5.41 \times 10^7$ Pa, a Poisson's ratio of $\nu = 0.293021$, and a density of $\rho = 2149$ kg/m^3. The yield stress and the hardening slope for the Drucker-Prager formulation are $\sigma_{yield} = 2.10926 \times 10^5$ Pa and $H = 0.0$ Pa. The friction angle and dilantancy angles are assumed to be $\beta = 51.7848°$ and $\phi = 51.7848°$, respectively. In order to parameterize the contact method between the block and the soil, a nodal contact surface is used. A collision detection radius for the spherical contact geometry was set to 0.009 m and a contact stiffness coefficient of 165000 N/m was used for the penalty based force evaluation. The deformed shape of the soil across the centerline at the time when the maximum load occurs is shown in Fig. 5.9 and this compares the Chrono::FEA implementation to that of an in-house flexible multibody dynamics code [14]. It is clear along the soil profile where the contact is made with the rigid punch box and the plastic deformation occurs. Four nodes were identified across the centerline: Node 1 is at the far left edge, Node 2 is the node closest to the rigid
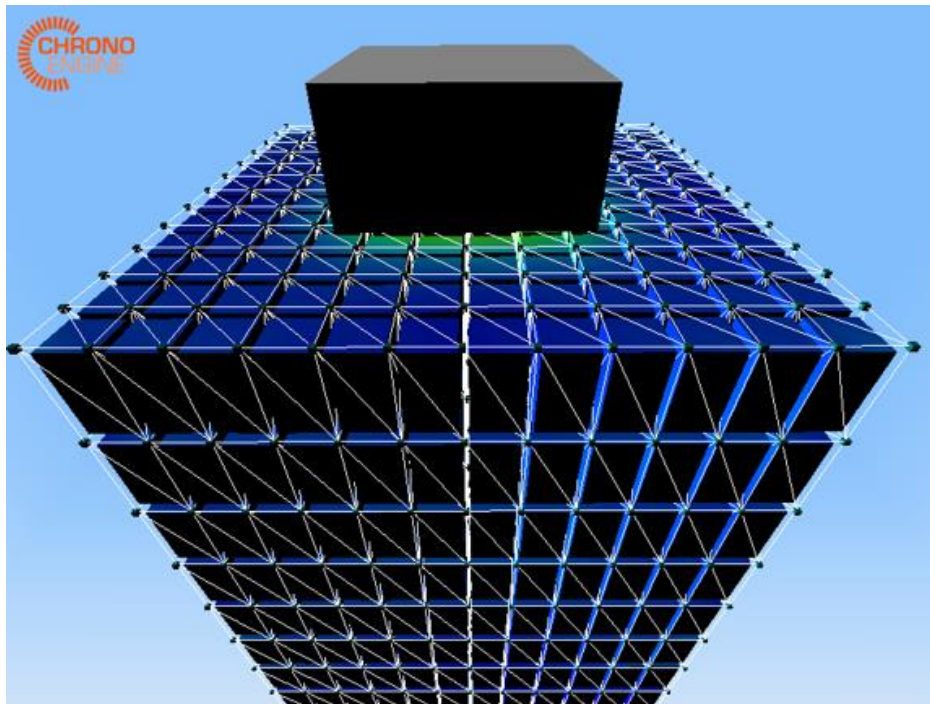
Figure 5.8: Diagram of the soil punch test conducted in Chrono::FEA

block that is still outside of the contact region, Node 3 is the first node that occurs inside the contact region, and Node 4 is the at the center of the block/soil contact. The vertical displacement time history, shown in Fig 5.9, demonstrates the plastic yielding of the nodes in contact with the rigid punch block at a time of $t = 0.29\,\text{s}$. The results of the Chrono::FEA implementation and the in-house code [14] agree very well for the use of the Capped Drucker-Prager plasticity model.

<u>5.4 Deformable Tire Numerical Examples</u>

5.4.1 Quasi-Static Loading

The initial test for the deformable on-road tire model (195/65/R15) used by Yamashita [14] was a vertical loading test on an inflated tire on rigid terrain. For these tests, an on-road deformable tire model constructed from shear deformable shell elements is dropped onto a flat rigid ground body for which the contact forces are is determined with a nodal contact method created in a load class. The contact formulation was based on an adaptive penalty method that would scale the effective contact stiffness and damping coefficients by the number of nodes penetrating the ground. This was done to ensure a uniform interpenetration of all of the nodes into the ground body in order to produce more realistic tire profile deformation. The tire model has a rim radius of 0.227 m and an uninflated tire radius of 0.30685 m. The internal air pressure load of the tire is set to 220 kPa and is applied to the surface of a shell element tire with a mesh resolution of 120x24 elements in the circumferential and width directions, respectfully. The undeformed and deformed tire profile shapes are compared in Fig. 5.10 for a constant vertical loading of 3 kN.
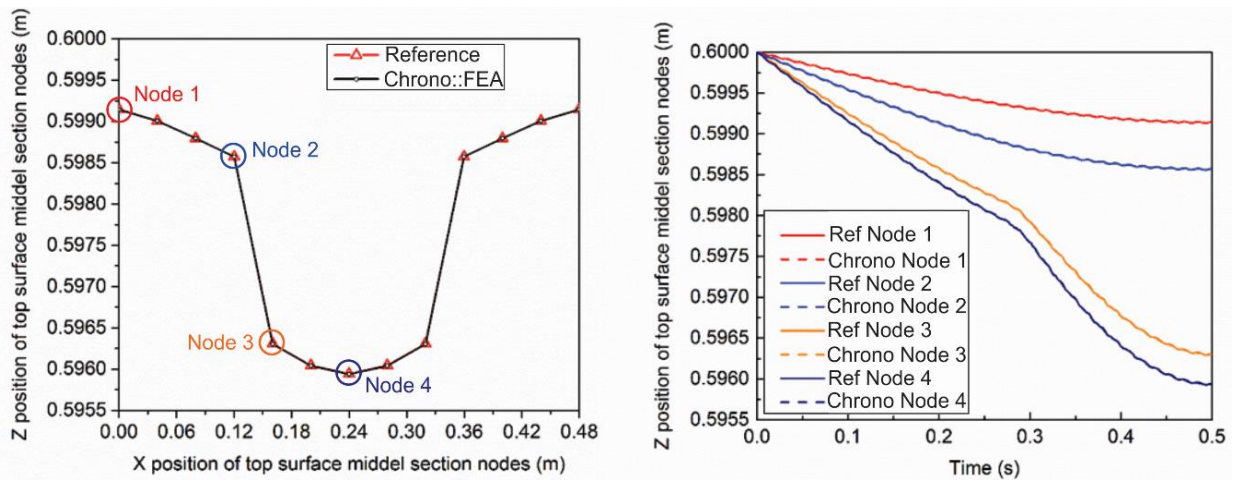
Figure 5.9: (Left) The plastically deformed configuration of the centerline of the finite element soil model. (Right) The time history position of selected nodes along the soil centerline
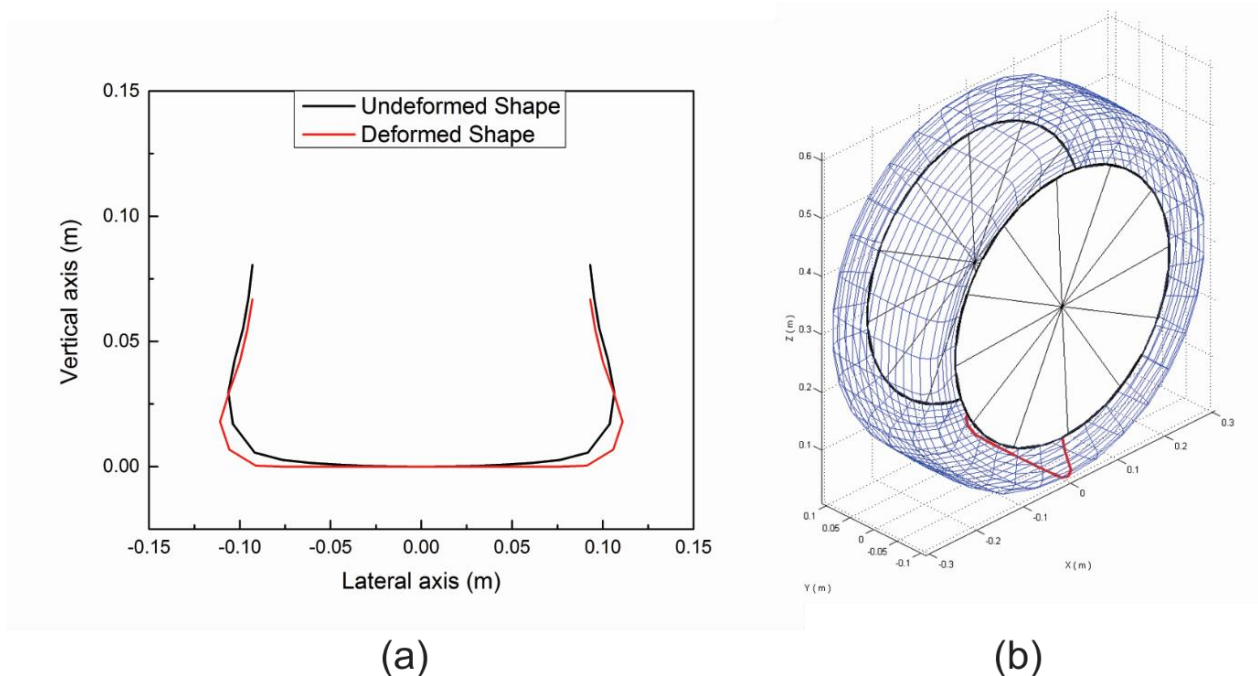
Figure 5.10: (a) Diagram of the cross sectional profile of the deformable tire model in both the undeformed reference configuration and the deformed tire shape under a quasi-static loading condition. (b) Diagram of the on-road deformable tire model constructed from shear deformable shell elements

At the steady state condition, the contact forces were evaluated to determine the normal contact pressure distribution across the contact patch. The normal contact pressure distribution results are shown in Fig 5.11 for the 4.0 kN loading case in Chrono::Vehicle, the in-house deformable tire dynamics simulation code, and experimental data for the same tire model [14]. This quasi-static loading scenario was repeated for over a range of vertical loads from 1.0 kN to 4.0 kN. For each of these simulation cases, the contact patch size was calculated and the vertical and lateral tire profile deflection were collected. From this data, the load-deflection curves shown in Fig 5.12 as well as the contact patch size as a function of vertical load shown in Fig 5.13 for the on-road deformable tire were created. There is good agreement between the equivalent tire models in Chrono and the reference tire simulation for the relationship between the normal contact force and the deformation of the tire body.
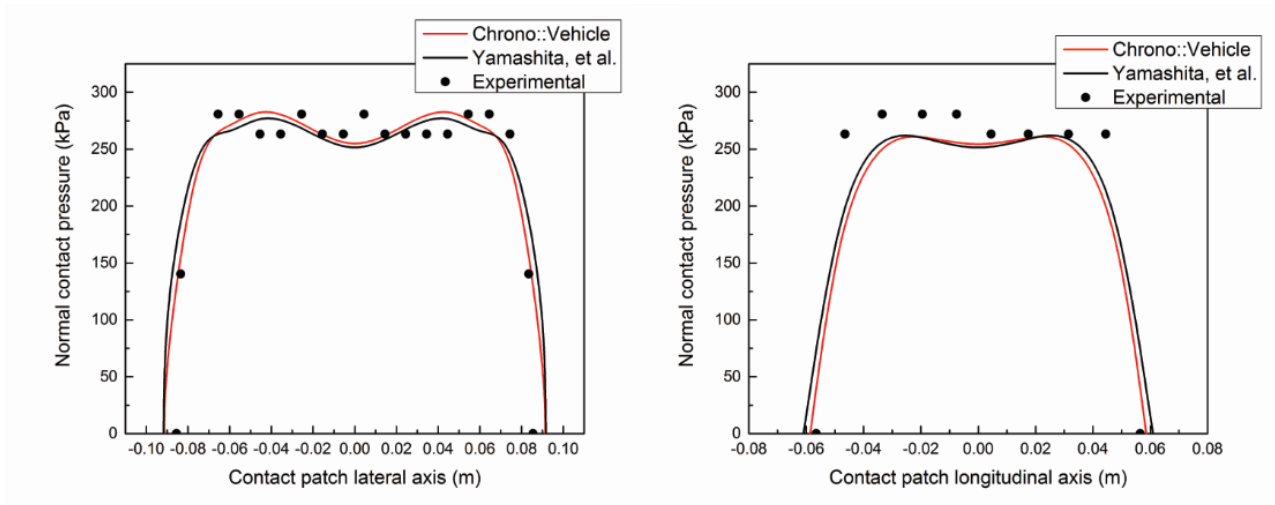
Figure 5.11: The normal contact pressure distribution for the quasi-static loading scenario of 3.0 kN across the center of the contact patch across the lateral (Left) and longitudinal (Right) directions of the tire [14]
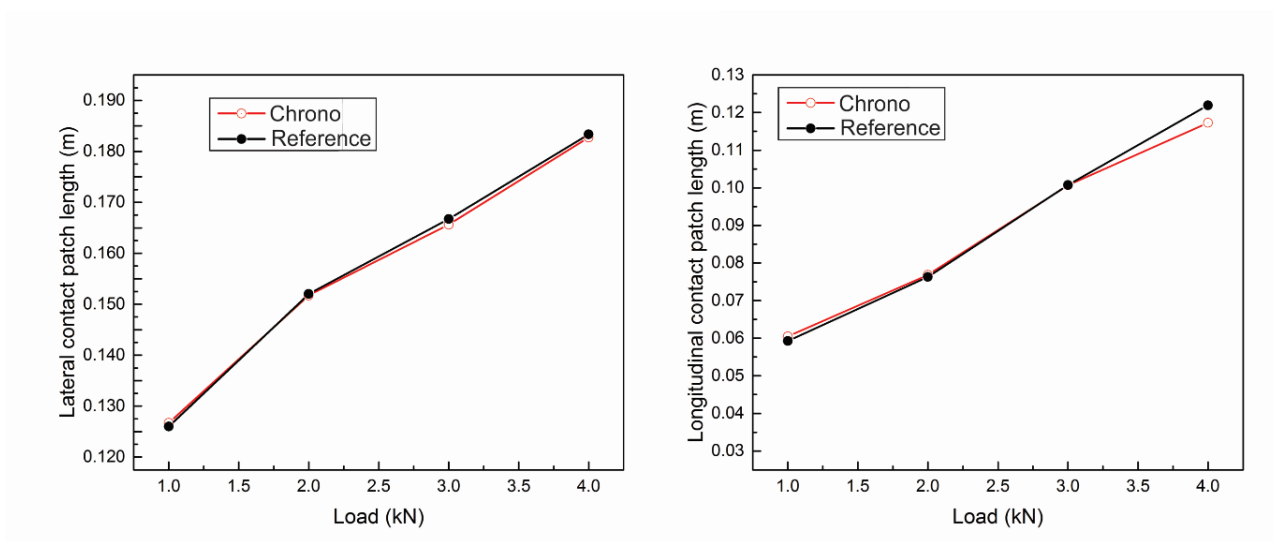
Figure 5.12: The relationship of the contact patch size in the lateral (Left) and longitudinal (Right) directions for a quasi-static loading condition of the deformable tire compared to a reference deformable tire model outside of the Chrono::Vehicle framework [14]
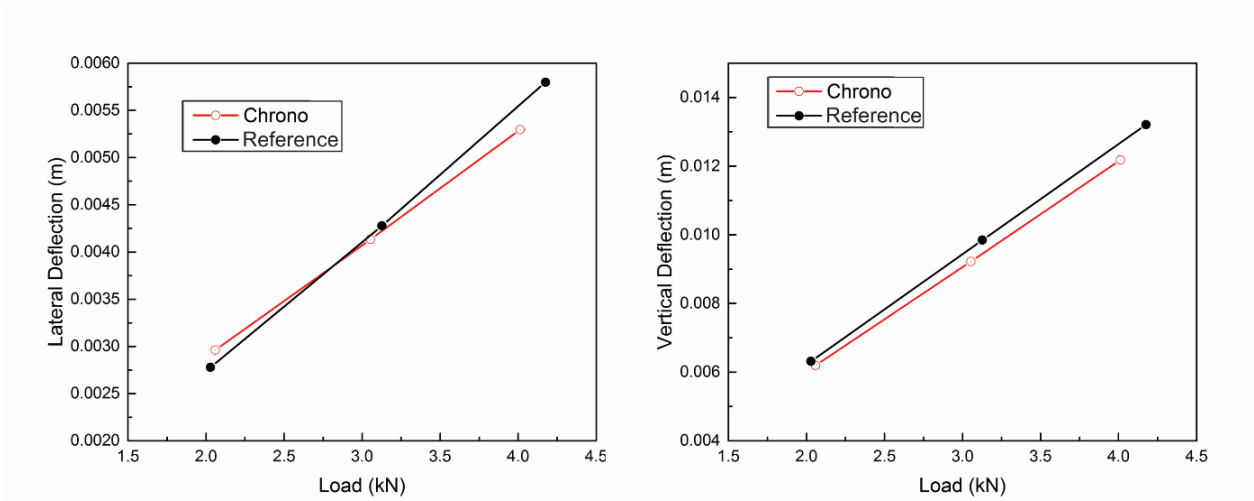
Figure 5.13: The relationship of the lateral (Left) and vertical (Right) deflection for a quasi-static loading condition of the deformable tire compared to a reference deformable tire model outside of the Chrono::Vehicle framework [14]

5.4.2 Steady State LuGre Rolling Simulation

The rolling tire dynamics of the deformable tire model were validated using a steady state LuGre friction model. In this model, the internal friction parameters $z_x\left(\zeta,t\right)$ and $z_y\left(\zeta,t\right)$ are introduced to define the shear contact stresses over the contact patch. The contact patch is discretized into small LuGre element ij, for which the shear contact stress is defined as [37,38]:

$$\left.\begin{array}{l} p_x^{ij} = \left(\sigma_{0x}z_x^{ij} + \sigma_{1x}\dot{z}_x^{ij} + \sigma_{2x}v_{rx}^{ij}\right)p_n^{ij} \\ p_y^{ij} = \left(\sigma_{0y}z_y^{ij} + \sigma_{1y}\dot{z}_y^{ij} + \sigma_{2y}v_{ry}^{ij}\right)p_n^{ij} \end{array}\right\} \tag{5.1}$$

where p_n^{ij} is the normal contact pressure acting on the LuGre element ij. The slip velocity in the element is represented by v_{rx}^{ij} and the coefficients σ_{0k}, σ_{1k} and σ_{2k} are friction parameters for LuGre tire friction model [37,38]. From which, the longitudinal and lateral contact forces defined in the LuGre element ij can be obtained as [37,38]

$$F_x^{ij} = p_x^{ij}\Delta L^{ij}\Delta b^{ij}, \qquad F_y^{ij} = p_y^{ij}\Delta L^{ij}\Delta b^{ij} \tag{5.2}$$

where Δb^{ij} is the width of LuGre element ij. In the steady-state model of the spatially discretized LuGre tire friction, the friction parameters of each element can be obtained by solving the following equation recursively from the leading edge, where $z_x^{0j} = z_y^{0j} = 0$ [14]:

$$\left.\begin{array}{l}\left(\dfrac{\sigma_{0x}\left|v_{rx}^{ij}\right|}{g_x\left(v_{rx}^{ij}\right)}+\dfrac{\left|r^{ij}\omega^{ij}\right|}{\Delta L^{ij}}\right)z_x^{ij}=v_{rx}^{ij}+\dfrac{\left|r^{ij}\omega^{ij}\right|}{\Delta L^{ij}}z_x^{i-1,j}\;,\quad i=1,\cdots,n\;;\quad j=1,\cdots,m\\[4mm]\left(\dfrac{\sigma_{0y}\left|v_{ry}^{ij}\right|}{g_y\left(v_{ry}^{ij}\right)}+\dfrac{\left|r^{ij}\omega^{ij}\right|}{\Delta L^{ij}}\right)z_y^{ij}=v_{ry}^{ij}+\dfrac{\left|r^{ij}\omega^{ij}\right|}{\Delta L^{ij}}z_y^{i-1,j}\;,\quad i=1,\cdots,n\;;\quad j=1,\cdots,m\end{array}\right\} \quad (5.3)$$

The shear contact stresses can then be defined by Eq. 5.3.

Using the same on-road deformable tire model as the previous tire simulation case, a rolling tire simulation was created to evaluate the impact of spatially dependent friction model. For this scenario, the tire was vertical loaded with 4.0 kN to the center of the rim and a gradual torque of $\tau(t)=1000(t-0.1)$ Nm was applied to achieve a steady state rolling condition at $V=22.5$ m/s. From this point the frictional model was changed from a simple Coulomb friction to the LuGre model described above. The normal contact pressure distribution was obtained in this condition and is illustrated in Fig. 5.14. The shear contact stress distribution due to the LuGre contact forces were also evaluated and these results are displayed in Fig. 5.15. These results compare very well to those obtained by Yamashita et al [14].
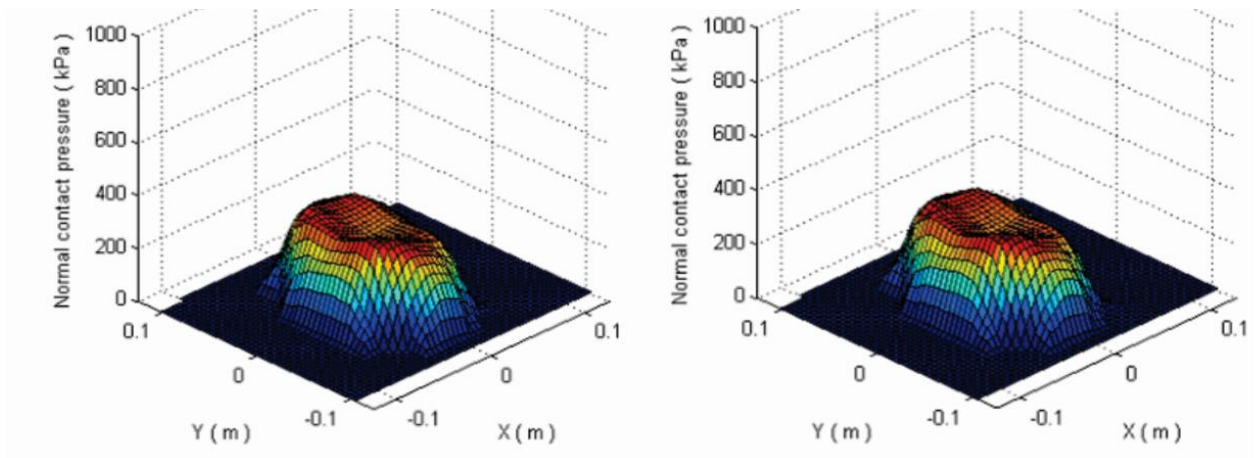
Figure 5.14: The three dimensional normal contact pressure distribution during the rolling tire simulation with LuGre friction obtained from a Chrono::Vehicle simulation (Left) and a deformable tire reference simulation (Right) [14]
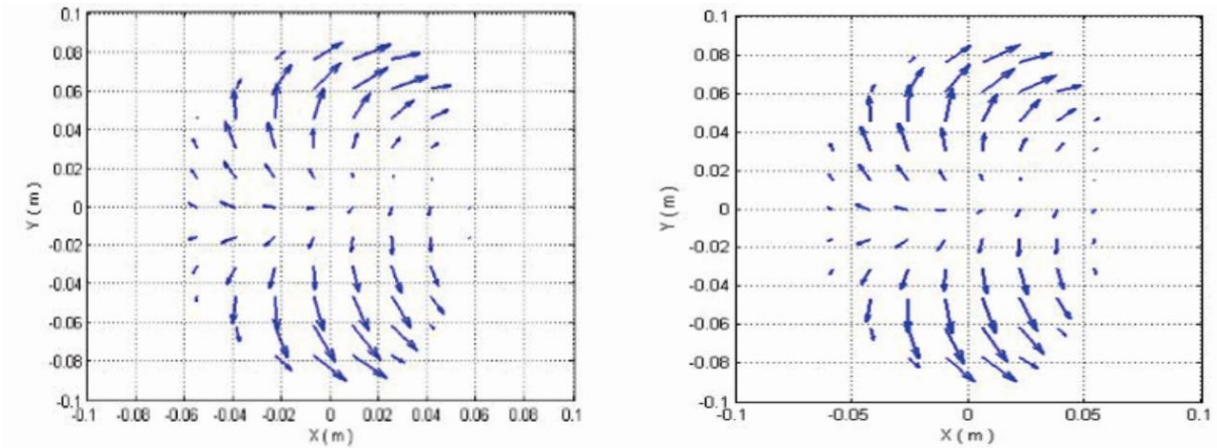
Figure 5.15: The distribution of the shear contact stresses within the tire contact patch during the rolling tire simulation with LuGre friction obtained from a Chrono::Vehicle simulation (Left) and a deformable tire reference simulation (Right) [14]

5.4.3 Treaded Tire Over Step Obstacle

As mentioned in the previous chapter, the integration of the deformable tire model into the Chrono::Vehicle architecture allowed for the modeling of an off-road tire with a deformable tire body and tread pattern. In order to demonstrate the capability of the off-road treaded tire, the model was run across a single rigid step obstacle. This model uses the generalized off-road tire, which has its layer configuration and material properties described in Section 4.4.2. The rim radius is 0.2683 m, the rim width 0.254 m, and the undeformed tire radius is 0.4673 m. The deformable tread blocks are composed of the same material properties of the rubber used in the off-road tire, which is a Young's modulus of $E = 4.74 \times 10^7$ Pa in the fiber and matrix directions, a Poisson's ratio of $v = 0.45$, and a shear modulus of $G = 1.63 \times 10^7$ Pa. A vertical load of 5.0 kN and a gradual torque of $\tau(t) = 3000(t - 0.05)$ Nm is applied to the center of the rigid rim body. The treaded tire simulation is shown using Irrlicht visualization is shown at times $t = 0$ s, $t = 0.28$ s, $t = 0.43$ s, $t = 0.51$ s in Fig. 5.16. At these times, the tire is in its initial condition, rolling up the rigid step, reaching steady state rolling on top of the step, and dropping back to the rigid ground, respectively. The forward and vertical position results of the treaded tire simulation are shown in Fig. 5.17.
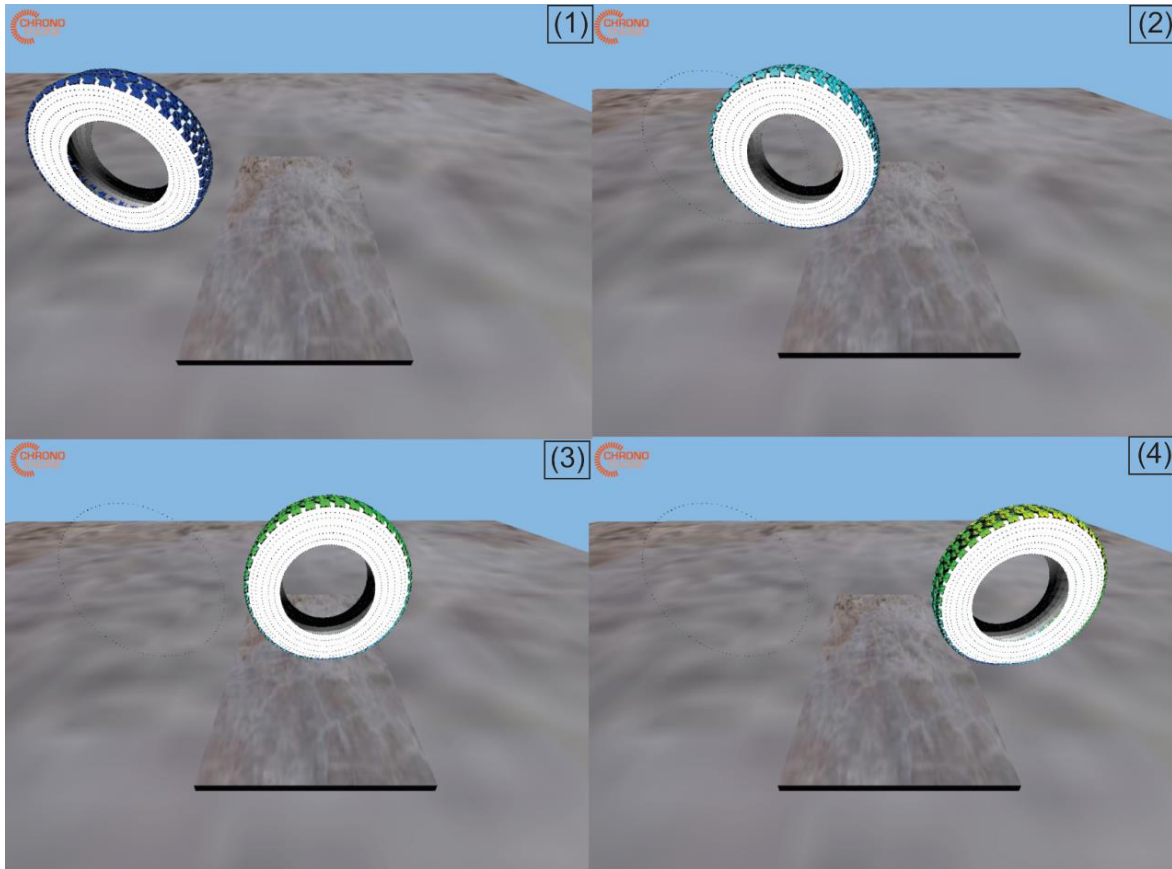
Figure 5.16: Snapshots of the visualization of the rolling treaded tire simulation as the tire transverses the small step obstacle
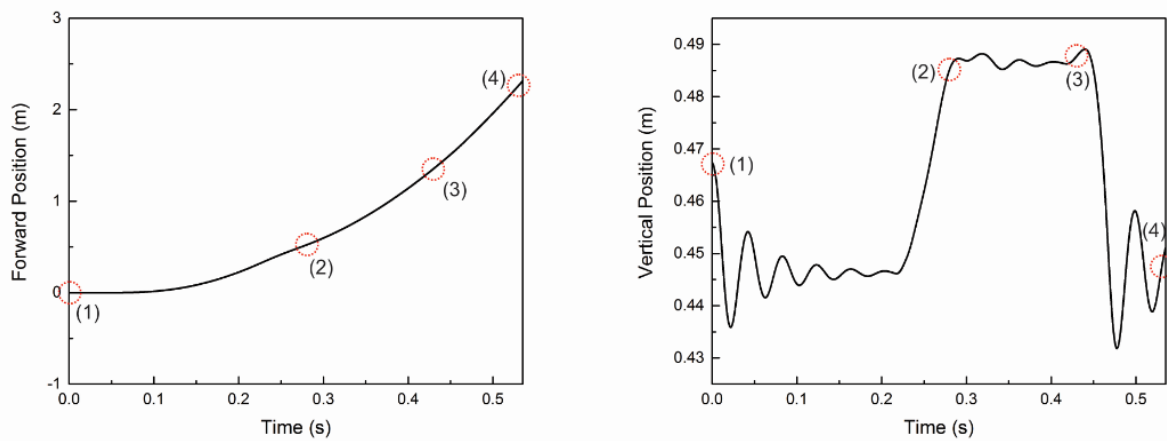
Figure 5.17: (Left) The vertical wheel position of the treaded tire model rolling over a step object. (Right) The forward wheel position of the rolling treaded tire, clearly demonstrating the impact of the step obstacle on the forward motion of the tire

5.4.4 Lugged Rigid Tire on Deformable Soil

An agricultural lugged rigid tire model was created from an object file created in ABAQUS and the surface geometry is mapped onto the rigid tire model. This tire model was then integrated into the tire test rig model in Chrono::Vehicle. A diagram of this lugged tire model in the Chrono::Vehicle simulation can be seen in Fig. 5.18. The tire rig consists of a chassis body, rim body, wheel body, and tire body as well as bodies that will define the toe angle, camber angle, relative distance between the wheel and the chassis that are defined in the global system. A prismatic joint is used to constrain the chassis to the global ground body in order to only allow forward motion. The chassis is then constrained to the set toe angle body via revolute joint about the chassis vertical axis. The wheel's distance from the chassis is then defined with a prismatic joint and this body is then constrained to the set camber angle with a revolute joint about the forward axis of the wheel. A final revolute joint is used between the rim and camber angle body to allow for the rolling about lateral rim axis. The wheel is the fixed to the rim and serves as contacting body for rigid tire simulations. A linear actuator is used to apply a kinematic constraint on the forward velocity of the tire rig. In this scenario, a constant forward velocity of 20 m/s was enforced through the actuator constraint and was applied as an initial condition to the tire rig bodies. A vertical load of 5 kN was applied to the wheel carrier body to emulate a quarter vehicle load. The contact parameters of the rigid tire body include a contact stiffness coefficient of $k = 2.0 \times 10^6$ N/m, a damping coefficient of $c = 2.0 \times 10^3$ Ns/m, and a friction coefficient of 0.9.
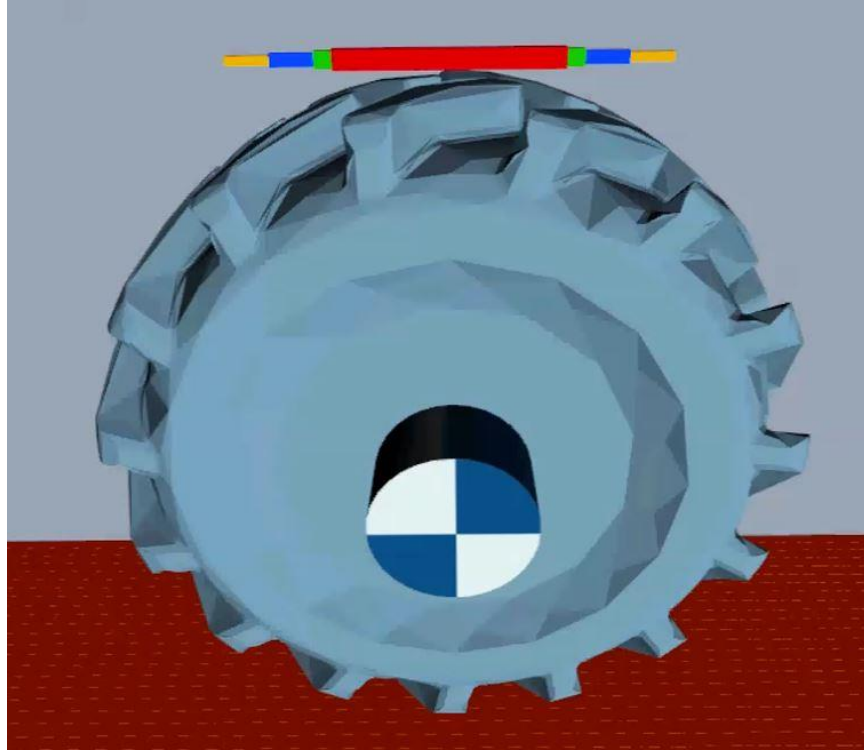
Figure 5.18: Diagram of the lugged rigid tire design with solid shading in its initial configuration

The 9-node brick element soil model was added to the tire rig system to model deformable terrain. The dimensions are 2.5 m in the travelling direction, 0.75 m in the lateral direction, and 0.5 m in the vertical direction. The mesh resolution of the soil is 150x45x6 elements in the travelling, lateral, and vertical directions. The density is assumed to be $\rho = 500\,\mathrm{kg/m^3}$, the Young's modulus is $E = 1.379 \times 10^7\,\mathrm{Pa}$, and the Poisson's ratio is $\nu = 0.3$. The Drucker-Prager plasticity formulation was used and the yield stress is set as $\sigma_y = 1.0 \times 10^4\,\mathrm{Pa}$ and the hardening slope was set to $H = 5.0 \times 10^3\,\mathrm{Pa}$. The friction angle and dilatancy angle of the plastic soil was assumed to be $\beta = 0.0°$, $\phi = 0.0°$, respectively. Snapshots of the lugged rigid tire simulation are shown in Fig. 5.19. At time $t = 0\,\mathrm{s}$, the rigid tire is in its initial configuration. At the second time point, $t = 0.03$ s, the rigid tire fully makes contact with the deformable terrain. At the third listed time, $t = 0.05\,\mathrm{s}$, the tire rolls forward out of the impacted soil where the first contact is made. At this time the tire is slightly raised due to the elastic forces of the deformable soil. At the final time point, $t = 0.115$ s, the tire has reached the end of the soil patch and the imprint of the rigid tread pattern can be seen clearly in the plastically deformed soil. A closer view of the tread pattern left in the deformed

terrain is illustrated in Fig. 5.20. The motion of the tire in quantified in Fig. 5.21 and the instances shown in Fig 5.19 are labeled.

Figure 5.19: A lugged rigid tire was assembled in the tire test rig model in Chrono::Vehicle and was run over the finite element based soil model comprised of 9-node brick elements. As the tire continues to roll forward, the pronounced tread pattern in accurately captured in the plastically deformed soil surface
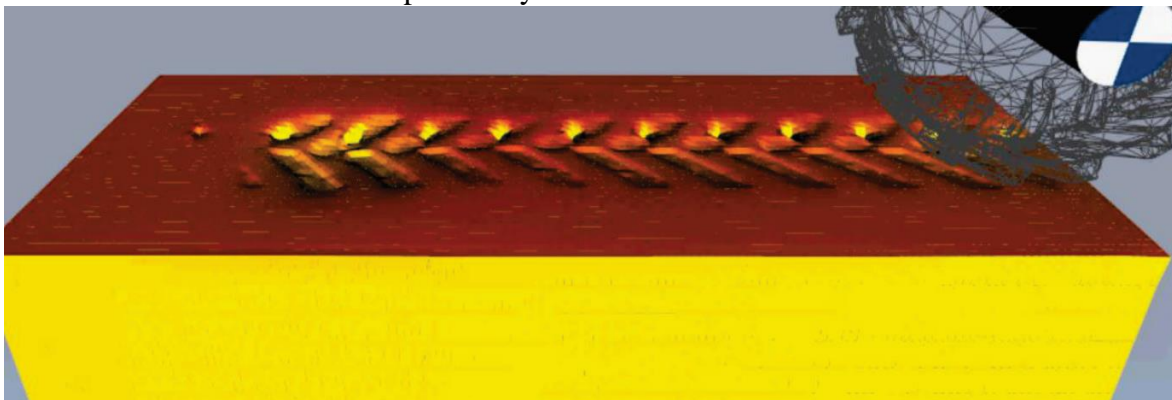
Figure 5.20: A close up snapshot of the imprinted tread pattern of the lugged rigid tire model

Figure 5.21: The overall motion of the lugged rigid tire rolling over deformable terrain is shown from the forward position (Left) and the vertical position (Right) time history data. The tire was subjected to a constant forward velocity of 20 m/s and a constant vertical load of 5 kN

5.4.5 Flexible Off-Road Tire on Deformable Terrain

Similar to the previous numerical example, a tire rig simulation was performed using the deformable off-road tire model interacting with the plastic soil terrain. The tire rig system was created in the same manner as the previous example, but with one exception. Where the rigid wheel body served as the body in contact for the rigid tire model, the flexible tire body was constrained to the rigid wheel in the creation of the deformable tire model in Chrono::Vehicle. The tire model used was the untreaded sample off-road tire as described in Section 5.4.3. The element mesh resolution was set to 90x24 elements in the circumferential and width directions, respectively. The contact properties are the same as the lugged rigid tire, with the stiffness coefficient of $k = 2.0 \times 10^6$ N/m, a damping coefficient of $c = 2.0 \times 10^3$ Ns/m, and a friction coefficient of 0.9. The deformable soil patch was created in the exactly the same as the previous numerical example for comparison. Images of the deformable tire test rig simulation can be seen in Fig. 5.22 at four time instances.
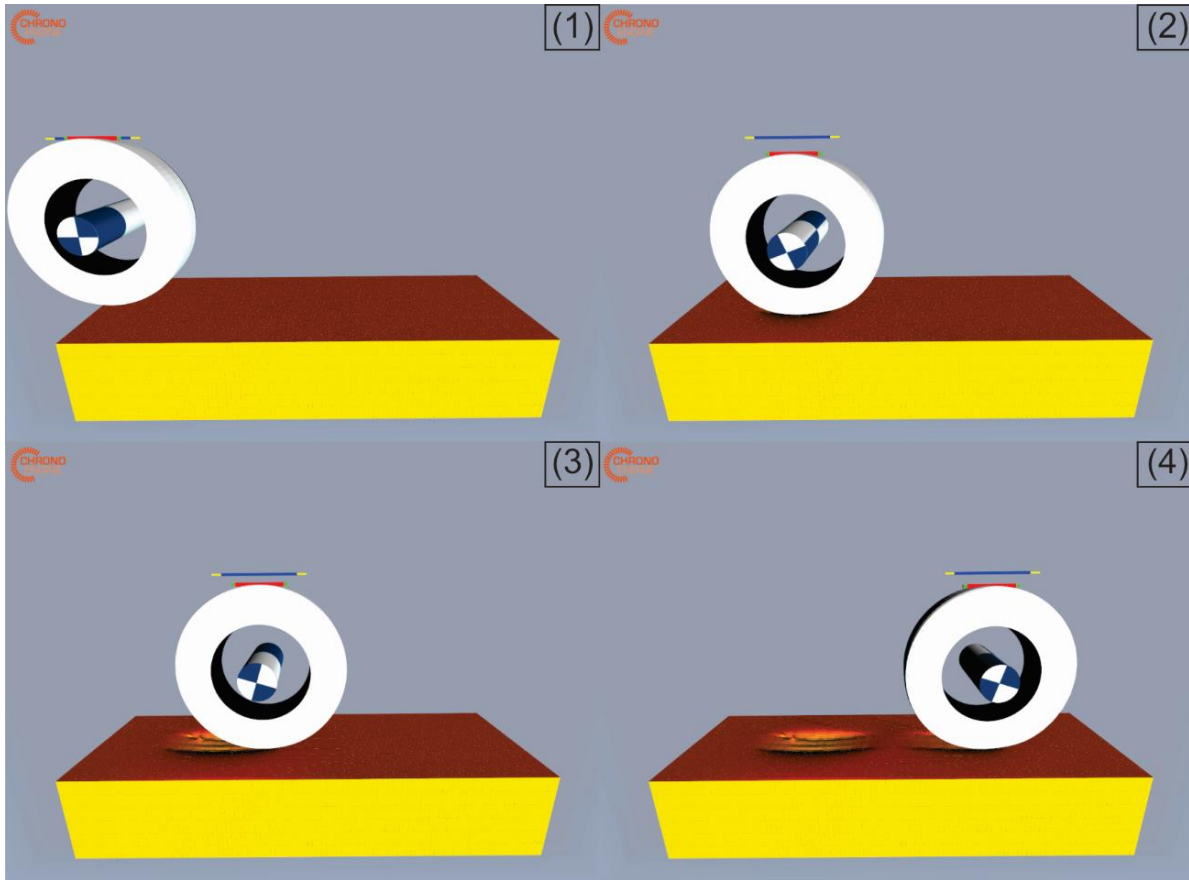
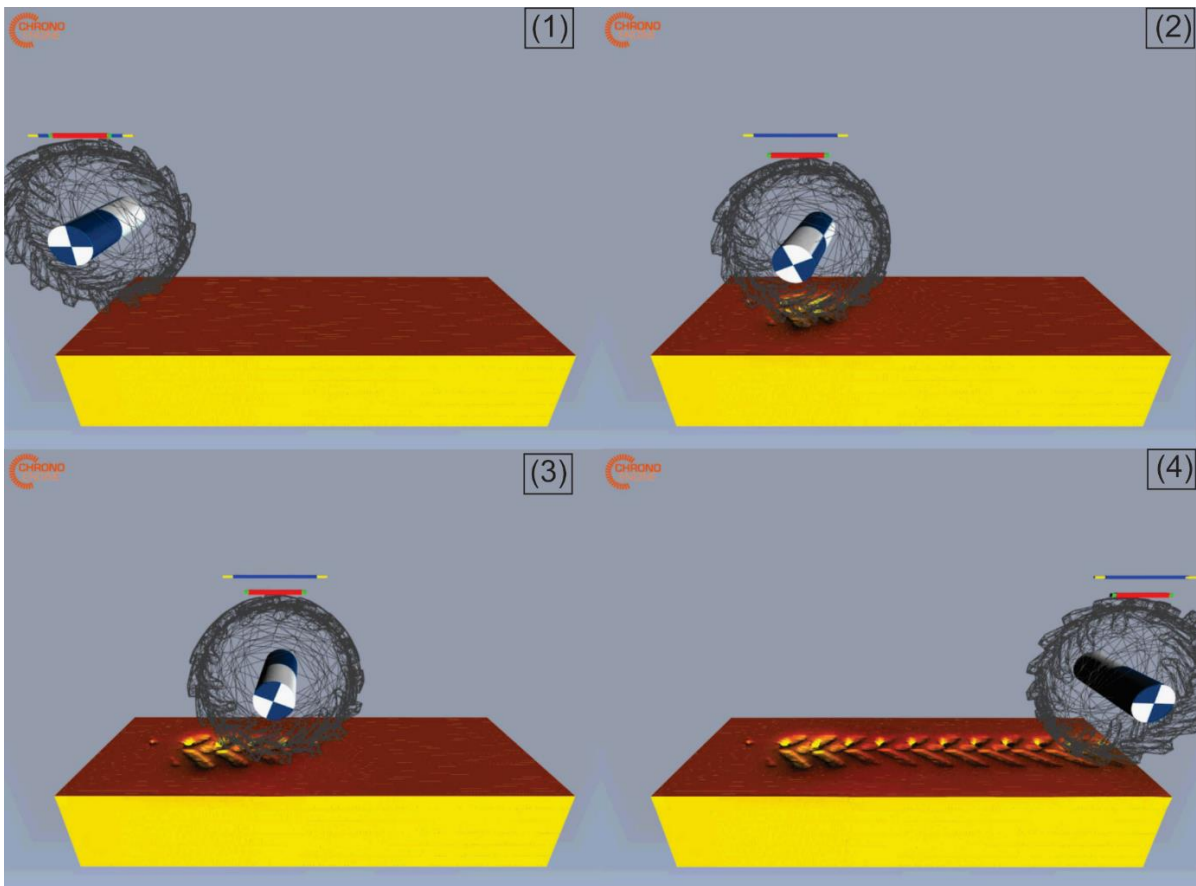Figure 5.22: The off-road deformable tire was assembled in the tire test rig model in Chrono::Vehicle and was run over the finite element based soil model comprised of 9-node brick elements. As the tire continues to roll forward, the bald tire imprint is left in the plastically deformed soil as the tire deforms from contact

At $t = 0$ s, the test rig is again in the reference configuration and the tire body is not inflated. At time $t = 0.03$ s the tire has reached the maximum deflection at which the tire and terrain are most deformed. At time $t = 0.05$ s the tire continues to roll forward out of the plastically deformed soil. The final time point is at $t = 0.075$ s shows the tire approaching the end of the terrain model and the footprint of the tire behind it. The time history of the forward and vertical position of the tire is displayed in Fig. 5.23. A comparison of the time history of both the lugged rigid tire and the deformable tire can be seen in Fig 5.24. It is clear that the tires share the same constant forward velocity for the duration of the simulation. It is also shown that the deformable tire experiences more bouncing phenomenon due to the elastic forces of the tire.
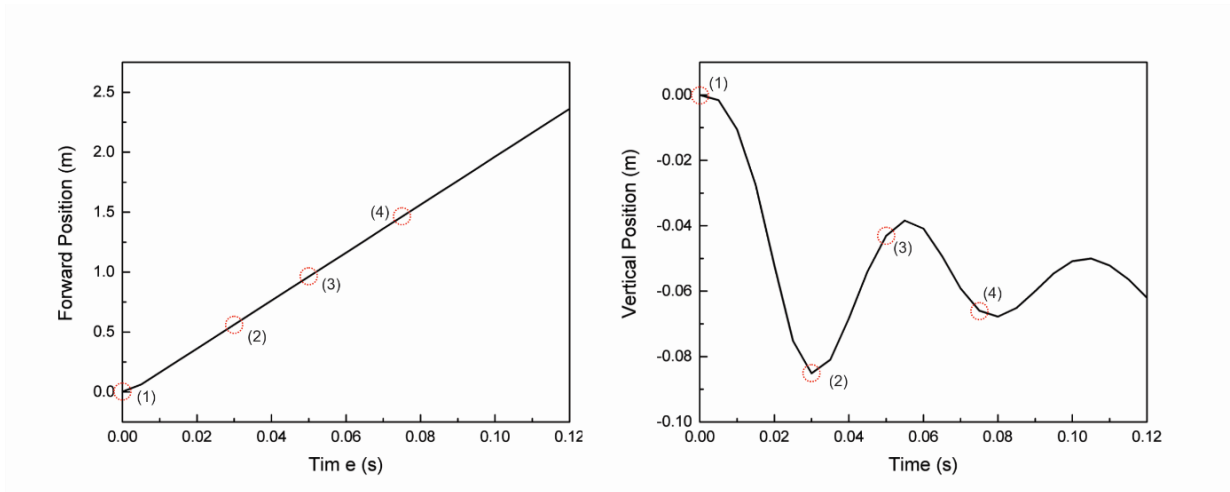
Figure 5.23: The overall motion of the off-road deformable tire rolling over deformable terrain is shown from the forward position (Left) and the vertical position (Right) time history data. The tire was subjected to a constant forward velocity of 20 m/s and a constant vertical load of 5.0 kN
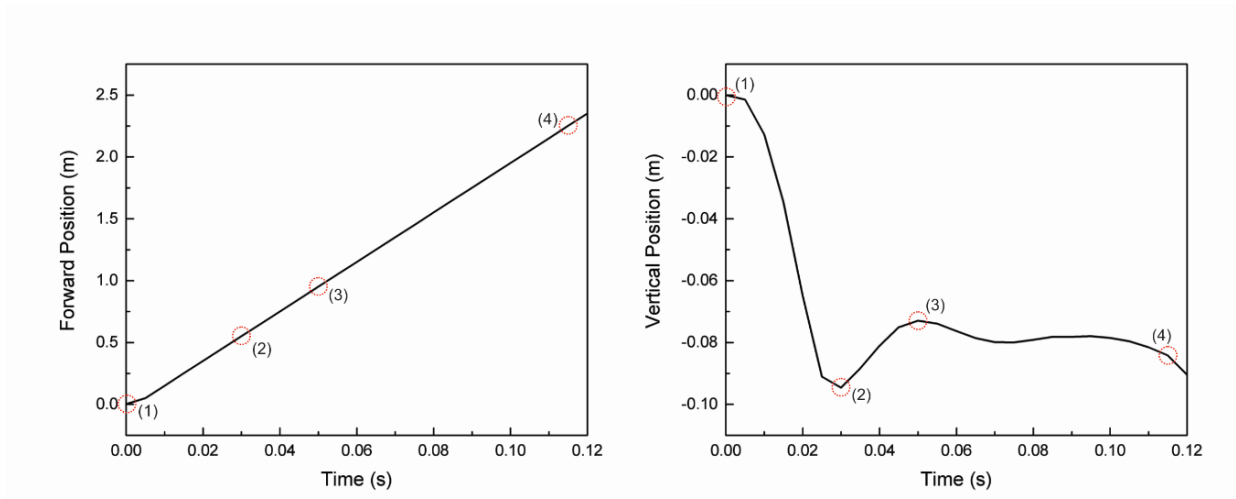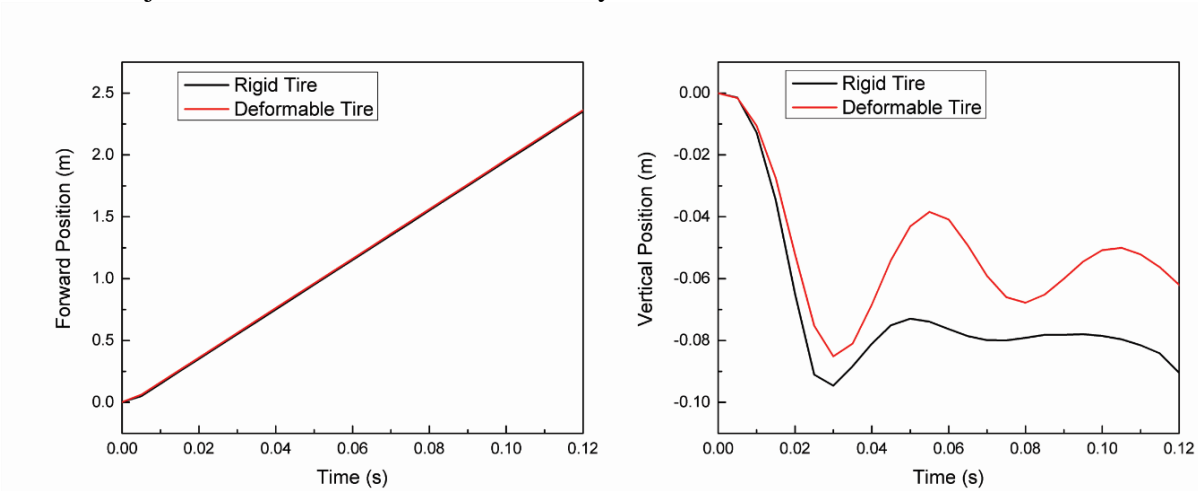

Figure 5.24: A comparison of the forward position (Left) and vertical position (Right) time history data for the equivalent tire test rig scenarios using the lugged rigid tire and the off-road deformable tire models

5.5 Computation Improvement Results

5.5.1 Open MP Scalability

The use of Open MP was applied to the evaluation of the element elastic force vector and elastic force Jacobian matrix at the element loop. This divides the calculation of these element functions amongst the available threads for the hardware being used. This has the theoretical potential to speed the computation time by a factor of the number of threads being used. However, it is not possible to achieve perfect scalability for parallel computing. As a test example, a simple swinging pendulum was created using 50x50 shear deformable shell elements. The configuration

of this model is shown in Fig. 5.25. For this problem, the parallel efficiency of flexible dynamics simulations is summarized in Fig. 5.26. The parallel efficiency is calculated from the following equation:

$$\eta = \frac{t_N}{t_1 / N} \tag{5.4}$$

where η is the parallel efficiency, t_1 is the computation time taken when using a single thread, and t_N is the computation time using N number of threads. This shows how close the scalability of the elastic force evaluation is to ideal. From Fig. 5.26, it is clear that as the number of available cores increases, the parallel efficiency will decrease. This reduction becomes saturated as the number of cores exceeds 8. Figure 5.26 also shows the reduction of the relative simulation time. As the number of cores increases, the computation time continues to be reduced but at a slower rate.
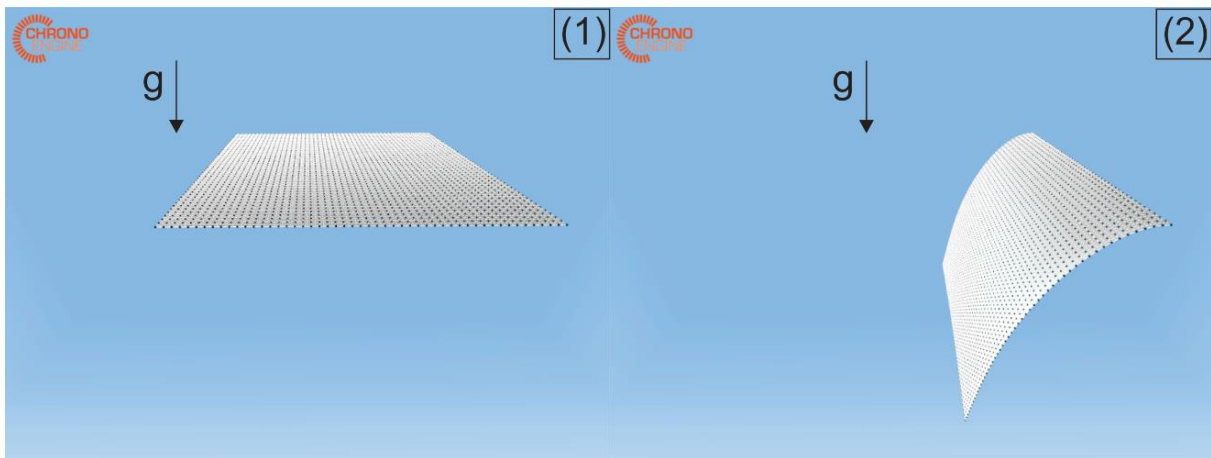
Figure 5.25: Diagram of the swinging shell pendulum benchmark problem in the (1) initial configuration and (2) the deformed configuration at time $t = 0.4\,\text{s}$
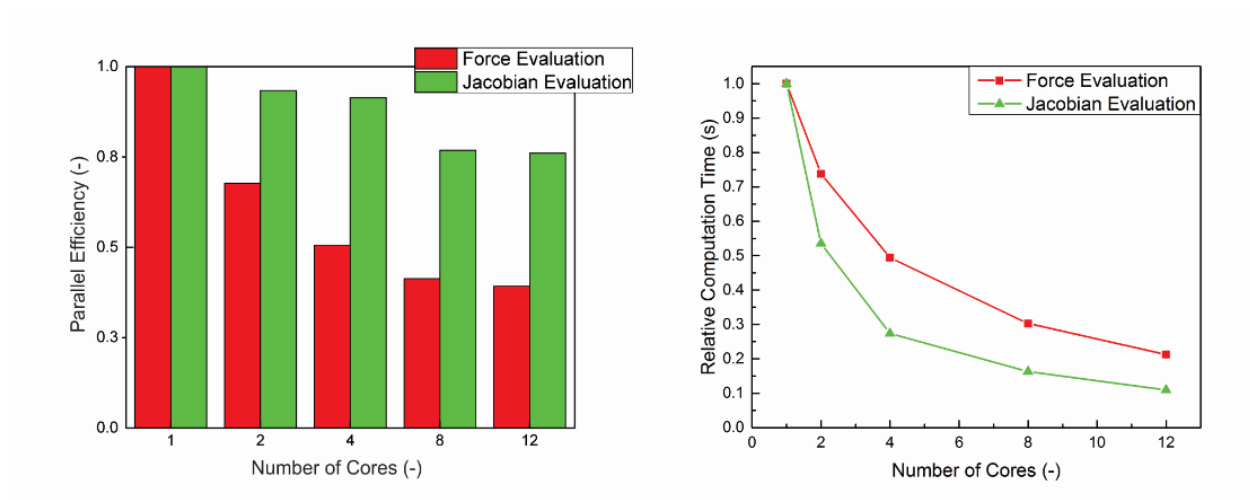
Figure 5.26: The parallel efficiency (Left) and the relative time reduction (Right) for the elastic force calculation and the elastic force Jacobian matrix evaluation due to the impact of Open MP on a flexible dynamics simulation

5.5.2 Impact of AVX

With the addition of AVX, the matrix calculations within the elastic force evaluation and elastic force Jacobian matrix calculation can performed more efficiently. As mentioned in Chapter 4, the inclusion of AVX can be used to execute operations between the elements of two matrices in parallel. To improve the performance of the flexible dynamics simulation, this method can be applied to large matrix operations that are used in the calculation of the elastic force vector, constitutive matrix, and elastic force Jacobian matrix. The relative computation time for the each of these calculations are shown in Table 5.1. The reduction of the percentage of the total simulation time taken by the elastic force and Jacobian evaluation is shown as well as the reduction of the total simulation time is also displayed in Table 5.1. With the addition of both AVX applied to the matrix operations in the elastic force and Jacobian evaluations and Open MP using four threads, the total computation time of a flexible multibody dynamics simulation was reduced by 58.3%.

Table 5.1: The impact of using AVX of the enhancement of large matrix operations on the efficiency of flexible dynamics problems

	Improvement from Matrix Operation with AVX
Elastic Force Evaluation	8.333 %
Jacobian Evaluation	30.612%
Percentage of Total Simulation Time	19.529%
Time per Iteration	8.168%

CHAPTER 6

FULL VEHICLE DYNAMIC SIMULATION

6.1 Full Vehicle Model Specifications

Full vehicle models can be constructed entirely from the subsystems that exist in Chrono::Vehicle. For the simulation examples discussed in this Chapter, a wheeled and tracked vehicle models are utilized. The following wheeled vehicle is described by subsystems that define the steering, braking, driveline, suspension, tire, and wheel. The wheeled vehicles use an all-wheel drive driveline model so that the four tires experience the same torque from the throttle. The powertrain subsystem for the vehicle accounts for the inertia of the engine block, crankshaft, and in-gear shaft to transfer torque from the engine to the wheels and taking energy losses into account. The powertrain system will automatically shift gears when the vehicle reaches the maximum forward velocity at the current engine output. The full wheeled vehicle system has a mass of $m = 2530$ kg and is subjected to gravitational forces in the vertical direction. The fully constructed vehicle model is shown in Fig. 6.1 with four deformable tires.

The tracked vehicle in Chrono::Vehicle is modeled after the M113 armored personnel carrier. The full vehicle systems are comprised of idlers, sprockets, suspensions, and track-shoe subsystems. The idler consists of a cylindrical rigid body inserted under the track-shoes in the rear of the vehicle and is attached to a linear actuator in order to create tension in the track. The sprocket subsystem creates a rigid gear body, using circular arcs to draw the gear profile. The track-shoe subsystem is constructed from a series a rigid shoe bodies that are connected to one another using revolute joints. The assembly of the tracked vehicle is done such that the initial configuration is under the least amount of tension in order to allow for variability in design. The slack of the initial track hangs from the front of the vehicle and the extension of the idler in the initial time steps creates the track-shoe shape. The full tracked vehicle has a total mass of $m = 15970$ kg. An image of the tracked vehicle in its initial configuration is shown in Fig. 6.2.

6.2 Simulations of Vehicle with Deformable Tires

The following simulation examples involve the wheeled vehicle system using four deformable off-road tires. A flat rigid box of 100 m in length and 100 m in width is used as the terrain model. The rigid terrain has a friction coefficient of $\mu = 0.9$, a contact stiffness coefficient of $k = 2.0 \times 10^5$ N/m, and a contact damping coefficient of $c = 40.0$ Ns/m.
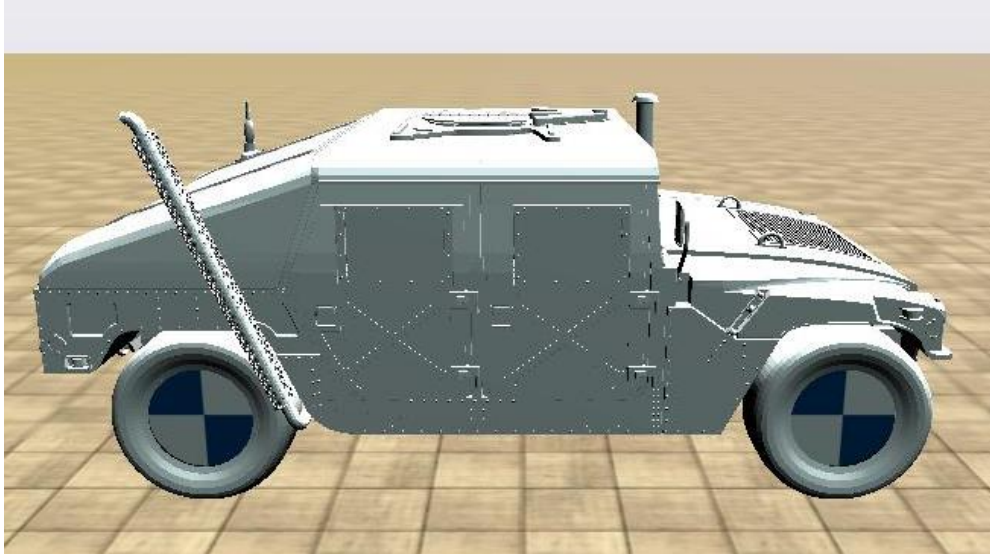
Figure 6.1: Diagram of the fully constructed wheeled vehicle with four deformable tire
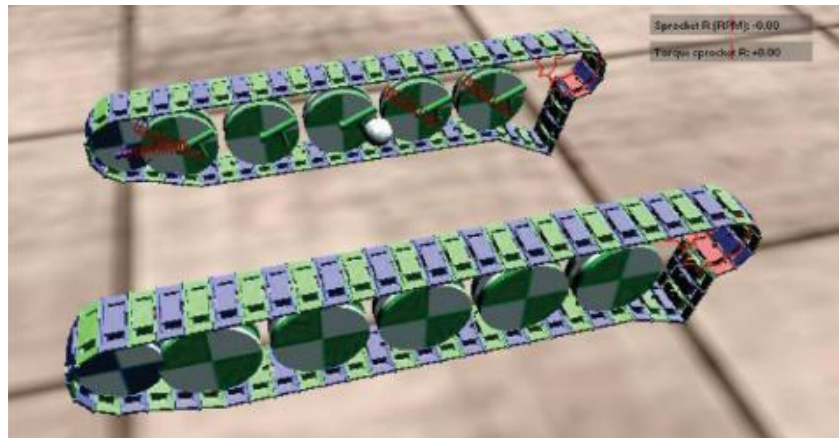
Figure 6.2: Diagram of the fully constructed M113 tracked vehicle

6.2.1 Forward Acceleration Simulation

In order to demonstrate capability of a vehicle mobility simulation using four deformable tires on a full off-road vehicle system. The wheeled vehicle is constructed with the initial chassis position at 0.49 m above the rigid ground (at 0.0 m). The four deformable off-road tires are each created from a mesh of 90x24 shear deformable shell elements. A driver model was created to describe the input operations to the vehicle system. In this example, the throttle is first applied at $t = 0.1$ s and is continuously applied as with the function $T(t) = 5(t - 0.1)$, until the maximum throttle is reached at $t = 0.2$ s. Snapshots of the forward vehicle acceleration are illustrated in Fig. 6.3 at the time points $t = 0.0$ s, $t = 0.03$ s, $t = 1.68$ s, and $t = 3.94$ s. At the first time point, the wheeled vehicle is in the initial configuration with the tires uninflated and the suspension

compressed. At $t = 0.03\,$s, the maximum torque is applied to the wheels and vehicle begins to accelerate forward. At the next two time points, $t = 1.64\,$s and $t = 3.97\,$s, the vehicle undergoes a gear change to second and third gear, respectively. The motion of the vehicle can be shown in Fig 6.4, where the time history of the forward position and velocity are displayed. These plots show the acceleration of the vehicle and the saturation of the forward velocity from the given torque. Once this steady-state velocity is reached, the gear is shifted upwards, accelerating the vehicle further. The time history of the contact forces exerted on the vehicle in the longitudinal and vertical directions are illustrated in Fig. 6.5. The longitudinal force plot describes the forward acceleration
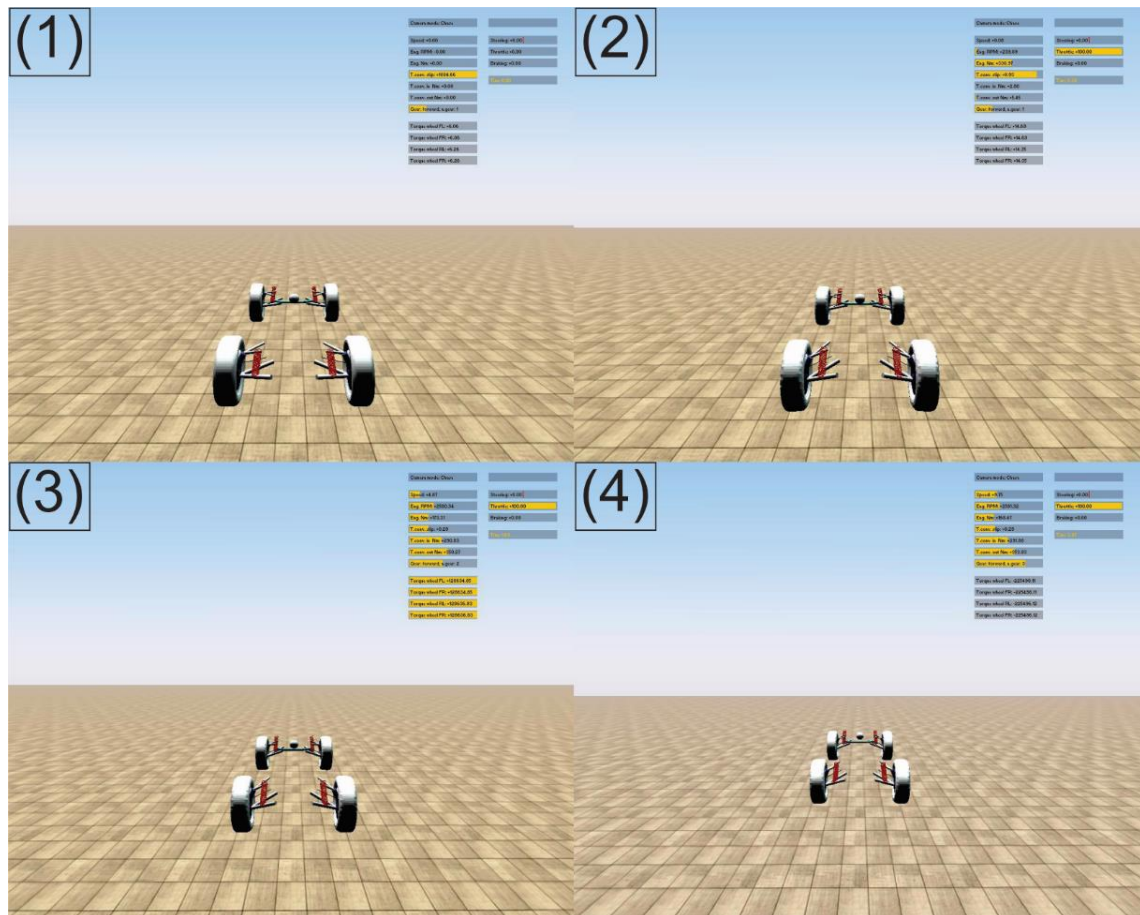
Figure 6.3: Images of the full vehicle with four deformable tires on rigid terrain in a forward acceleration scenario
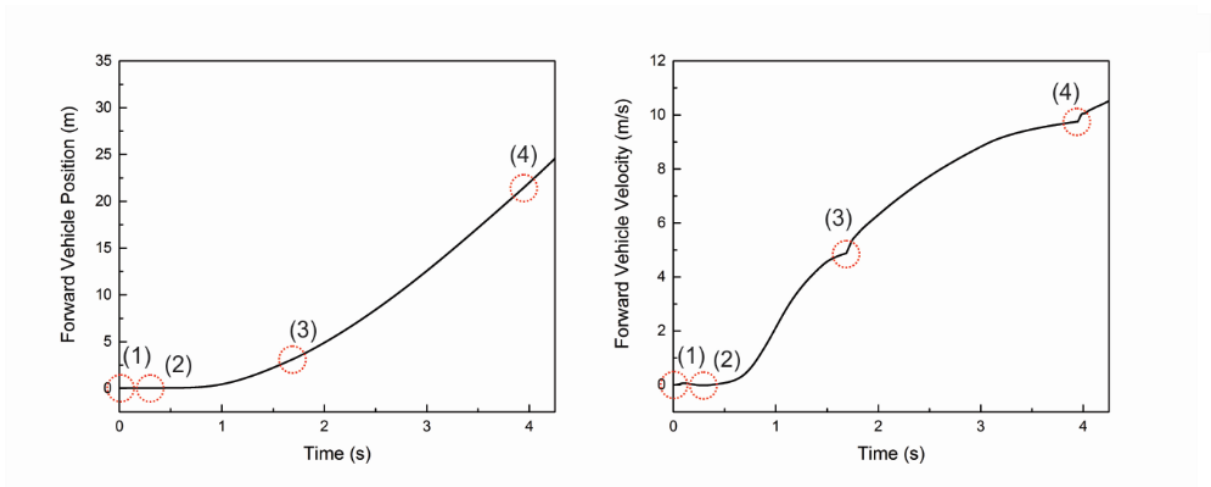
Figure 6.4: The time history plot of (Left) the forward position of the vehicle and (Right) the forward velocity of the vehicle
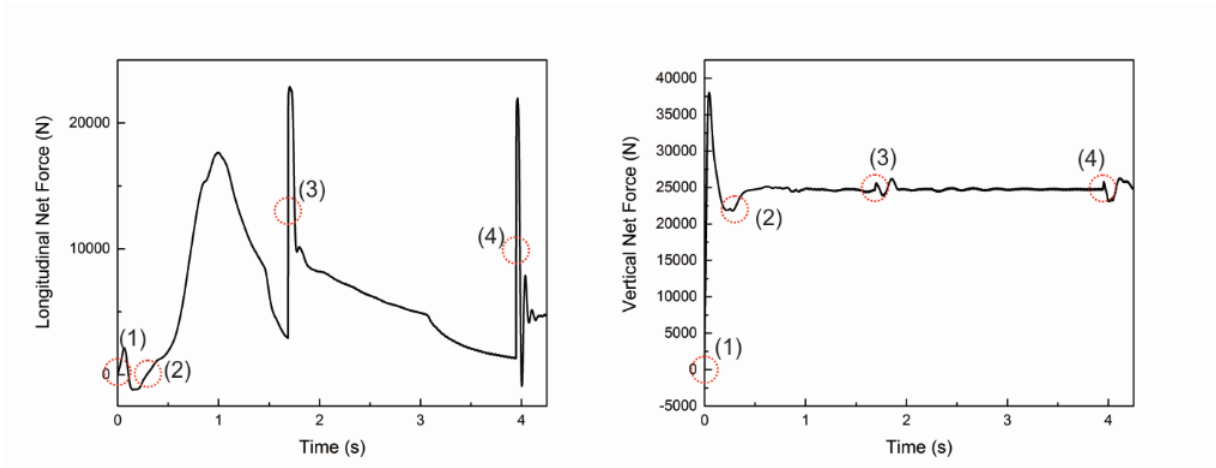
Figure 6.5: The time history plots of (Left) the net longitudinal force and (Right) the net vertical force on the deformable tires

by reaching the maximum Coulomb frictional force before slowly decreasing. This maximum friction force value is then reached again when the gear is shifted. The net vertical force shows the impact of the vehicle earlier in the simulation and the relatively steady-state value equal to that of the vehicle weight that is maintained. An equivalent simulation was performed using a rigid tire model with the same geometry.

6.2.2 Vehicle Cornering Simulation

In the following simulation example, the configuration of the vehicle is the same as that of the previous example. Similarly to the last example, the vehicle is assembled with four deformable

tires on dropped onto a flat rigid terrain. The throttle is applied once again at a rate of $T(t) = 5(t - 0.1)$, from a time of $t = 0.1\,\text{s}$ to $t = 0.3\,\text{s}$, where it is kept constant. At $t = 1.1\,\text{s}$, the steering is applied to the front wheelset of the vehicle with the function $T(t) = (t - 1.1)$ until $t = 1.6$ s. Images of the cornering simulation can be seen in Fig. 6.6 at time points $t = 0.0\,\text{s}$, $t = 0.30\,\text{s}$, $t = 1.10\,\text{s}$, and $t = 1.60\,\text{s}$. At the initial time, the vehicle is slightly off of the ground and the tires are not inflated. At $t = 0.30\,\text{s}$, the maximum throttle is first reached and the vehicle starts to accelerate forward. At $t = 1.10\,\text{s}$, the steering angle is first applied after the vehicle gets up to speed. At $t = 1.60\,\text{s}$, the steering is complete and the vehicle continues turning at this rate. Time history plots of the forward position and the lateral position are shown in Fig. 6.7. The contact forces applied to the deformable tires are also displayed in Fig. 6.7. A comparison of the deformable and rigid tire vehicles for the vehicle position and contact forces time history is illustrated in Fig. 6.8.
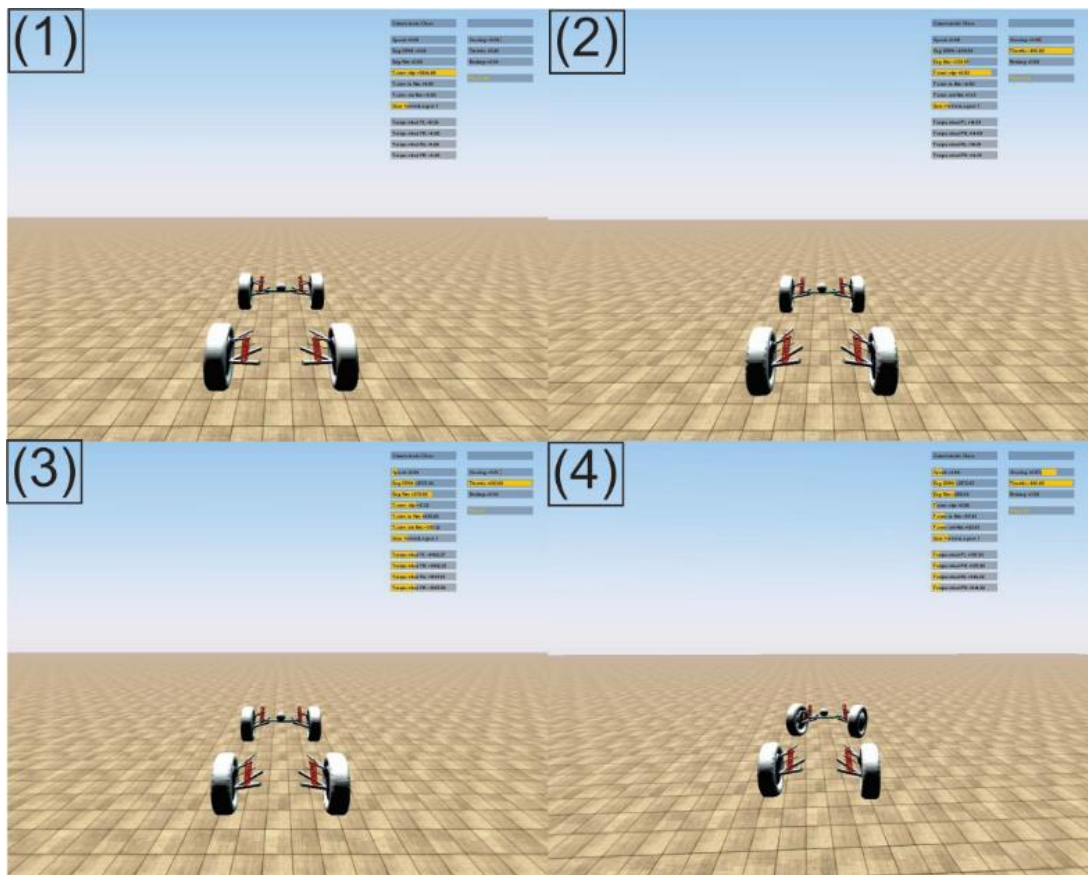
Figure 6.6: Images of the full vehicle system with deformable tires traveling over flat rigid terrain in a cornering scenario
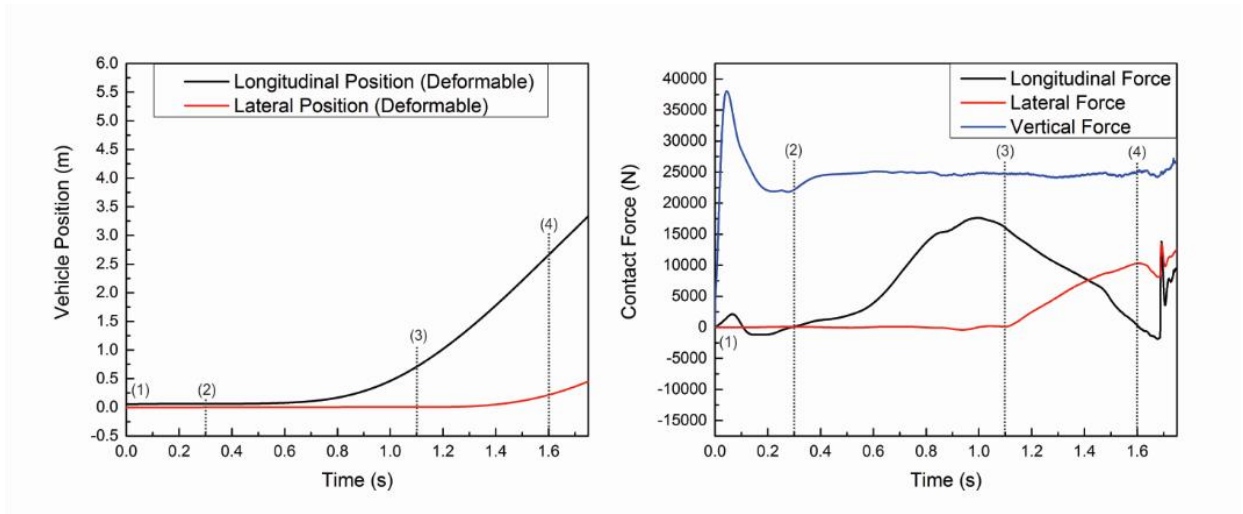
Figure 6.7: The time history plots of (Left) the longitudinal and lateral position of the wheeled vehicle and (Right) the net longitudinal, lateral, and vertical contact forces on the tires
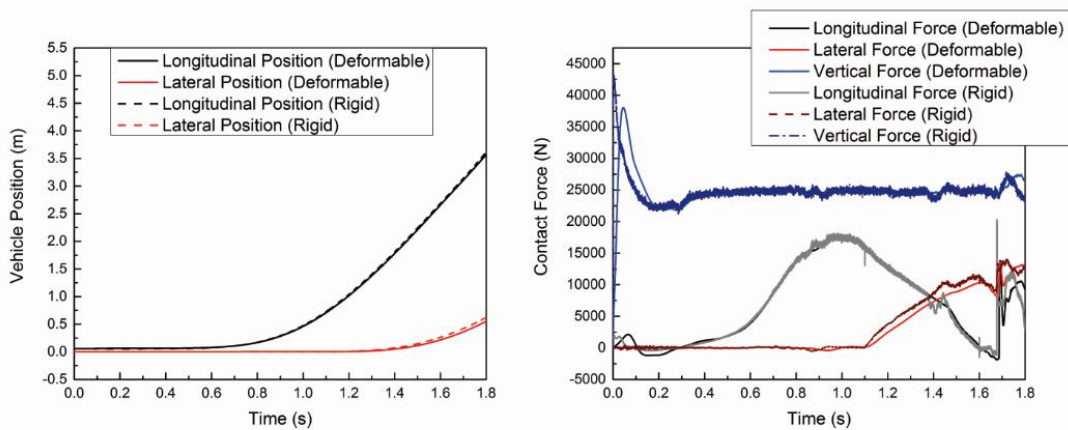
Figure 6.8: The time history plots of (Left) the longitudinal and lateral position of the wheeled vehicle and (Right) the net longitudinal, lateral, and vertical contact forces on the tires comparing vehicles with deformable and rigid tires

6.3 Vehicle Simulations on Continuum-Based Deformable Terrain

6.3.1 Vehicle with Rigid Tires on Deformable Terrain

The full vehicle model was created, this time with four rigid tires. The rigid tire bodies are defined as simple cylindrical collision models of radius of 0.467 m and a width of 0.254 m. These cylinders have a contact stiffness coefficient of $k = 2.0 \times 10^6$ N/m, a damping coefficient of $c = 2000.0$ Ns/m, and a friction coefficient of $\mu = 0.9$. The continuum deformable terrain model used comprised of 200x20x4 elements for a patch with the dimensions of 8.0 m in length, 3.0 m in width, and 0.75 m in height. The Young's modulus of the soil is assumed to be $E = 13.79$ MPa,

the Poisson's ratio is $\nu = 0.3$, and the density is $\rho = 200\,\text{kg/m}^3$. The permanent soil deformation was defined by the Drucker-Prager plasticity model where the yield stress and hardening slope are $\sigma_y = 10.0\,\text{kPa}$ and $H = 5.0\,\text{kPa}$, respectively. The friction angle and dilatancy angle are both assumed to be $0.0°$. Images of this simulation are shown in Fig. 6.9. at the time points $t = 0.0\,\text{s}$, $t = 0.33\,\text{s}$, $t = 1.91\,\text{s}$, and $t = 2.56\,\text{s}$. At the first time point, the body system is assembled above the deformable soil patch. At $t = 0.33\,\text{s}$, the vehicle has made contact with the continuum soil and is approaching the maximum penetration from the impact. At $t = 1.91\,\text{s}$, the vehicle has begun to roll forward out of the hole made from the initial impact. At the final time point, the vehicle is rolling steadily forward leaving a permanently deformed trail behind it. The time history of the forward and vertical positions of the vehicle is illustrated in Fig. 6.10, with the previously mentioned time points highlighted. It is clear from these results that the continuum based finite element soil model can be used to create a predictive model for full wheeled vehicle/soil interaction.

Figure 6.9: Images of the full vehicle system with rigid tires traveling over finite element deformable terrain in a forward acceleration scenario

Figure 6.10: The time history plots of (Left) the forward vehicle position and of (Right) the vertical vehicle position

6.3.2 Tracked Vehicle on Deformable Terrain

In the following simulation example, a tracked vehicle is dropped onto a half patch of deformable finite element terrain. The M113 tracked vehicle consists of 64 single pin shoes on the right track and 63 single pin shoes on the left track. The vehicle is initially located at a height of 0.8 m to account for the slack in the hanging track. This slack will be removed as the dynamic simulation starts and the initially compressed idler is extended to its equilibrium position. A large soil patch of 12.0 m in length, 5.0 m in width, and 0.5 m in height in located under the raised track vehicle system. The continuum soil is made up of a 60x30x6 element mesh with a collision detection radius of 0.015 m. The Young's modulus of the soil is $E = 13.79\,\text{MPa}$, the Poisson's ratio is $v = 0.3$, and the density is $\rho = 200\,\text{kg/m}^3$. The plastic soil deformation was described with the Drucker-Prager plasticity model where the yield stress is assumed to be $\sigma_y = 50.0\,\text{kPa}$, the hardening slope is $H = 25.0\,\text{kPa}$, the friction angle is $\beta = 0.0\,°$, and the dilatancy angle is also set to $\phi = 0.0\,°$. Snapshots of the tracked vehicle are illustrated in Fig. 6.11 at the time points $t = 0.0$ s, $t = 0.50\,\text{s}$, $t = 3.50\,\text{s}$, and $t = 5.50\,\text{s}$. At $t = 0.0\,\text{s}$, the vehicle is in the initial configuration and idler is compressed leaving slack under the track. At $t = 0.50\,\text{s}$, the vehicle has fully come into contact with the ground and plastic deformation occurs. At $t = 3.50\,\text{s}$, the vehicle moves out of the deformed hole left from the impact. Finally at $t = 5.50\,\text{s}$, the vehicle has moved forward leaving a

trail of permanently deformed soil behind it. The time history plot of forward position and vertical position of the vehicle are shown in Fig. 6.12.
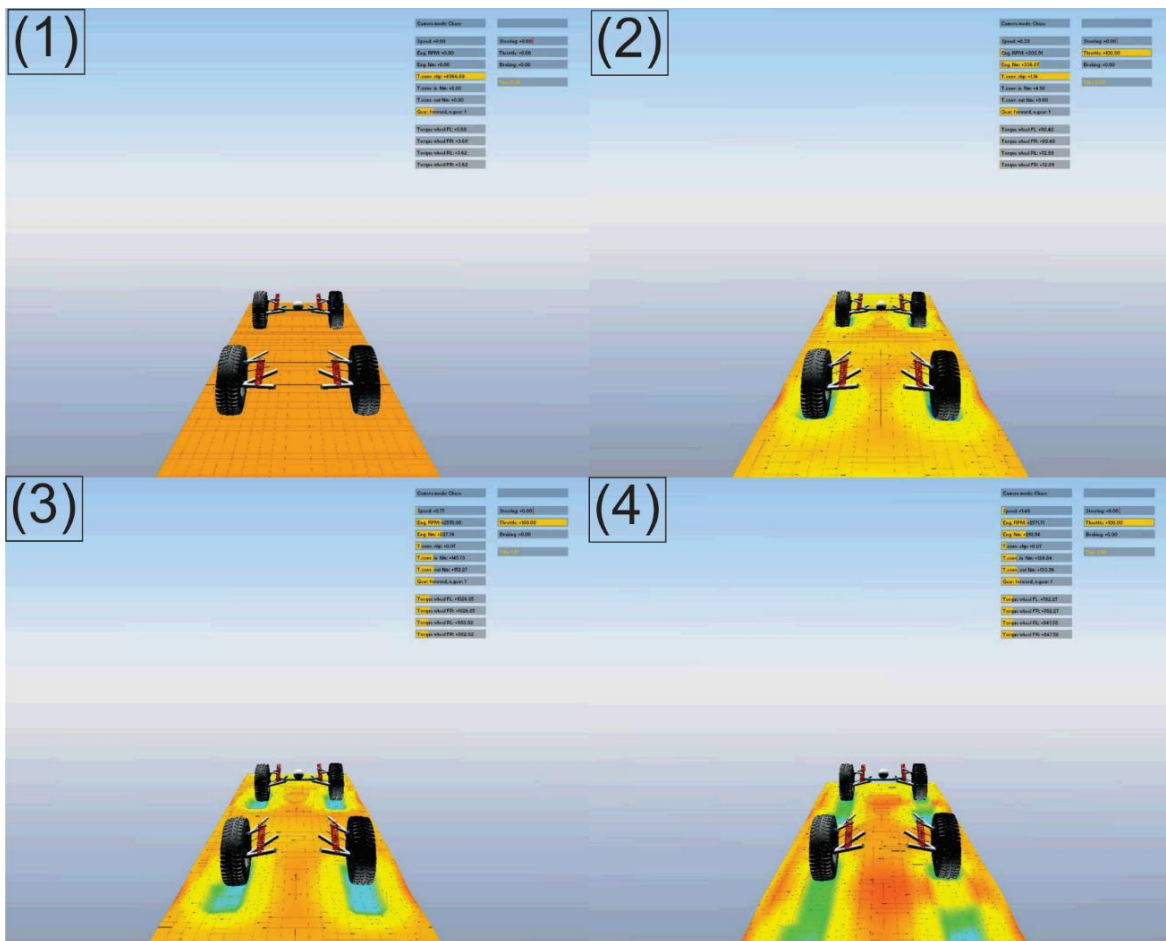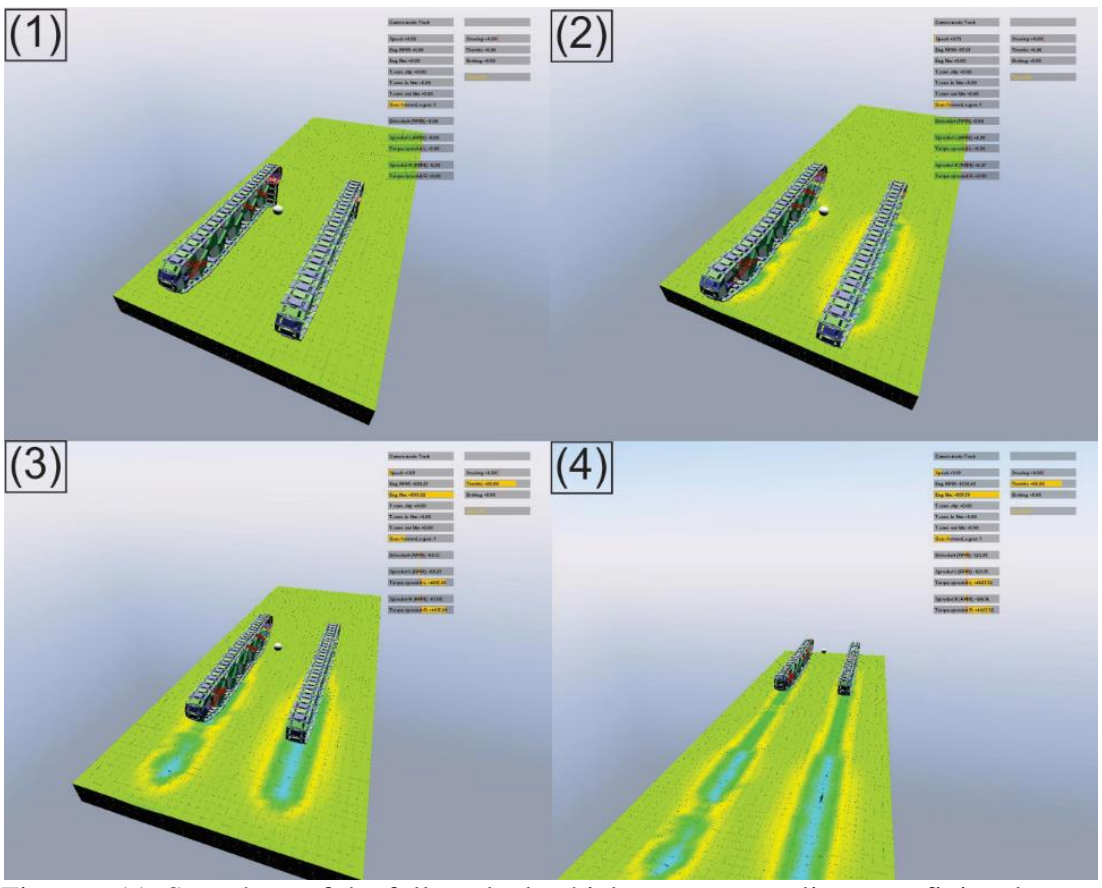

Figure 6.11: Snapshots of the full tracked vehicle system traveling over finite element deformable terrain in a forward acceleration scenario

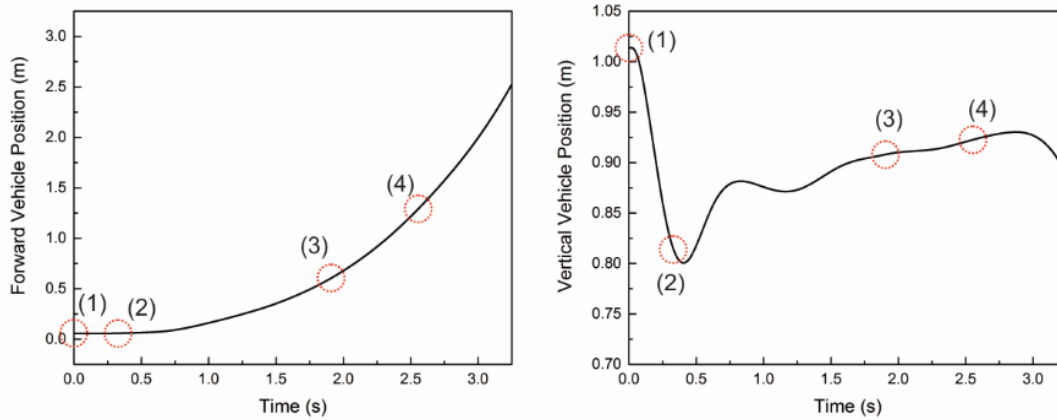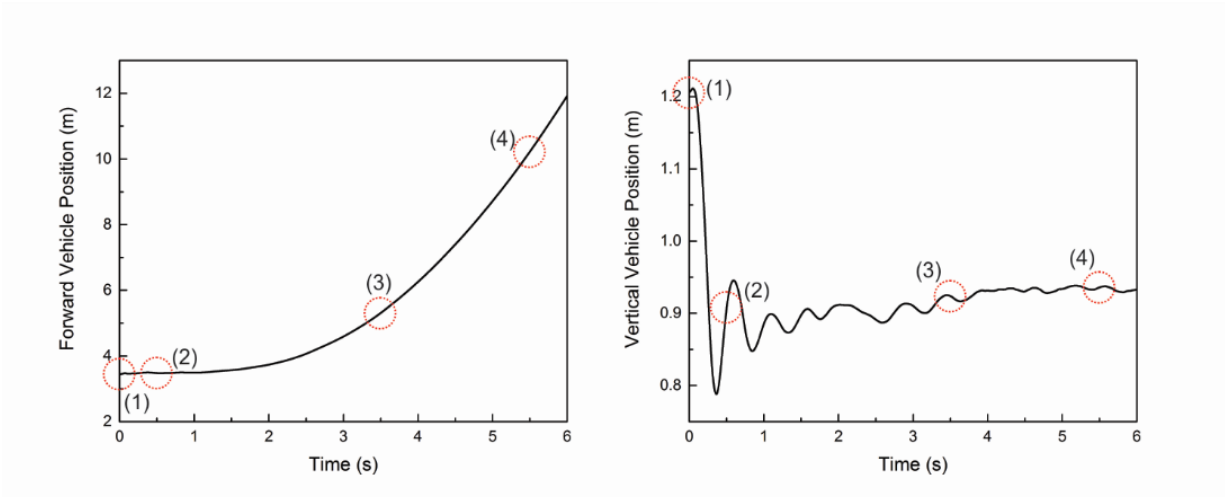Figure 6.12: The time history plots of (Left) the forward tracked vehicle position and of (Right) the vertical tracked vehicle position

CHAPTER 7

SUMMARY AND CONCLUSION

In the area of off-road vehicle mobility analysis, both empirical and semi-empirical models are widely used to quantify the vehicle/soil interaction. Despite their computational simplicity, these models are reliant on experimental data and do not accurately capture highly nonlinear terrain deformation. To create a more thorough reliable mobility analysis model, a high-fidelity physics-based computation modeling method was pursued in this study. To this end, the interaction of the vehicle tires and terrain must be considered extensively. In the area of dynamic tire modeling, computational models exist that make assumptions to determine the contact patch area and do not account for transient effects of the deformation of the tire on the contact forces. It is also difficult to incorporate finite element based deformable tires into multibody dynamics simulation due to fundamental differences in the formulations and solution procedures. This is often handled by co-simulation techniques with commercial software, but this requires a very small step size to ensure numerical stability during severe maneuvering scenarios. In off-road terrain modeling, finite element methods can also be used to represent soil as a continuum with the inclusion of constitutive models to describe the elasto-plastic behavior. For this reason, it is crucial that deformable tire and terrain models are developed such that they are integrated into a general-purpose multibody dynamics simulation framework. This allows for the creation of high-fidelity physics-based vehicle models that utilizes flexible multibody dynamics in a single computational environment. To achieve this goal, the following tasks were accomplished:

(1)   Integration and validation of a laminated composite shear deformable shell element based on the absolute nodal coordinate formulation into the flexible multibody simulation engine Chrono::FEA.

(2)   Integration and validation of a 9-node brick element considering the capped Drucker-Prager plastic yield criterion into Chrono::FEA.

(3)   Development and validation of a structural physics-based off-road deformable tire model that is parameterized and constructed within the Chrono::Vehicle framework.

(4)   Analysis of full wheeled and tracked vehicles on continuum-based deformable terrain within Chrono::Vehicle.

The computational structure of vehicle mobility simulation plays a critical role in contribution to the development of an accurate physics-based model. The chosen simulation environment must be capable of creating the high-fidelity tire and terrain models that can be used in conjunction with multibody dynamics computational algorithms. To this end, the multi-physics simulation engine Chrono was selected, and the features and capabilities of this software were described in detail in Chapter 2. Chrono is an open source C++ multi-physics simulation engine that has been previously utilized for evaluation of off-road mobility capability. This code has been developed and supported by research groups at the University of Parma, Italy and the University of Wisconsin-Madison. Chrono is modularly constructed such that additional features are built from the central computational solution procedure. This allows for the different analytical feature modules to interact within the same simulation framework. Chrono is capable of performing rigid multibody dynamics simulation and is equipped with a generalized solution procedure which can solve for the equations of motion either as a set of differential algebraic equations or differential variational inequalities. This multibody dynamics module, Chrono::MBD, contains a library of rigid body primitives and motion constraints and can also import rigid body geometry from third party modeling software. Finite element analysis can be performed by the Chrono::FEA module. In additional to these basic simulation modules, Chrono makes use of Toolkit modules that utilize the features of the more basic modules to support a specific application. For the purpose of this study, the Toolkit Chrono::Vehicle was used, which couples the features of Chrono::MBD and Chrono::FEA to create full vehicle models. These models can vary in complexity from a single tire testing rig consisting of a rim, wheel, tire and chassis to a full vehicle with four tires, suspension, operator commands, and powertrain. While this software has many necessary tools for vehicle mobility analysis, there is a lack of an accurate deformable tire model and continuum soil model needed for realistic off-road vehicle dynamics. Chrono also has the potential for high-performance computing capabilities, which can be essential for the performing high-fidelity vehicle mobility simulations in a reasonable timeframe.

In order to integrate physics-based deformable tire and terrain models into the vehicle dynamics simulation, it is first necessary to enhance the finite element analysis module with the inclusion of computationally efficient structural elements from which the tire and terrain models can be made. The integration of these structural elements for modeling deformable tires and soils was described in Chapter 3. For this purpose, a shear deformable composite shell element and a 9-

node brick element that were recently developed by Yamashita, et al. for physics-based tire/soil interaction simulations were integrated into the Chrono::FEA structure. The 4-node shell element is formulated based on the absolute nodal coordinate formulation and utilizes the global position coordinates as well as the transverse gradient coordinates at each node to describe the orientation and deformation of the element. Use of the transverse gradient coordinates leads to a constant mass matrix for fully nonlinear dynamics problems, thereby allowing the shell element to be integrated into a multibody dynamics simulation framework in a straightforward manner. The element lockings are eliminated with the use of assumed natural strain (ANS) and enhanced assumed strain (EAS) approaches in the generalized elastic force formulation. For the terrain modeling case, a 9-node brick element was integrated into the Chrono::FEA framework. This brick element considers the global position coordinate of the eight corner nodes and the curvature coordinates at a node in the center of the element. This element utilizes the Hencky strain measure in order to include finite strain multiplicative plasticity theories in the generalized internal force calculation. Numerical examples are shown in Chapter 5 for verification of the preceding elements against common finite element analysis software and an in-house flexible multibody dynamics code. The numerical convergence of the shear deformable shell element achieved a similar linear convergence as compared to that of the ANSYS Shell 181 element in both isotropic and laminated composite cases. The numerical convergence of the brick element also reached results similar to the ANSYS Brick 185 with enhanced assumed strain in an elastic benchmark case. The time history results of a benchmark using a Drucker-Prager plasticity model in the 9-node brick element was verified against the software ABAQUS and a capped Drucker-Prager model was compared to the in-house dynamics code, in which those elements were originally implemented by Yamashita.

Chapter 4 details the design and integration of the deformable tire and terrain models into the vehicle dynamics Toolkit Chrono::Vehicle. An off-road style tire was developed inspired by the design of the Wrangler MT tire. This model consisted of three material sections across the width of the tire, one for the bead, sidewall, and tread areas of the tire as these areas have vastly different material compositions. Each material section has a layer configuration for the laminated composite shell elements in that sections. Each layer consisted of a material property model, a ply angle, and a thickness. The complete structural design used the cut cross-section of a commercial tire to determine the layer configurations, the material properties required, and the initial undeformed tire shape.

The tire properties, such as the load-deflection relationship, contact patch size, deformed shape, and normal contact pressure distribution were verified in Chapter 5, using experimental and published results. The shear contact stresses of the tire were then verified against published results for a steady-state rolling tire using a LuGre tire friction model. The basis for this tire model was then integrated into the Chrono::Vehicle module so that the design can be easily modified and automatically generated. A deformable tread pattern was then integrated into the off-road style deformable tire with the use of co-rotational tetrahedral elements. This element was used because of its simple integration onto the deformable tire model and the ability to model important tread pattern features, such as diagonal gaps for granular soil flow, without significant mesh refinement. A shared connectivity method was used such that the tetrahedrons and the shells could be defined with the same node objects in Chrono. A numerical example of the performance of this treaded tire model as it is able to successfully traverse over a rigid step obstacle is shown in Chapter 5. A description of the continuum based soil model and its generalization and integration into Chrono::Vehicle is also discussed in Chapter 4, while examples of its interaction with various tire models are shown in Chapter 5. In these examples, a lugged rigid tire and the deformable off-road tire are each run over a patch of continuum soil using the tire test rig model. The soil is able to accurately capture the tire footprint of the bald deformable tire and the tread pattern of the lugged rigid tire in its plastically deformed state.

When considering the large degree of freedom systems that come with finite element based tire and terrain models, the simulation can be very computationally expensive. To remedy this, methods such as Open Mulit-Processing (OpenMP) and Advanced Vector Extensions (AVX) were integrated into the Chrono architecture to lessen the computational burden. OpenMP allows for execution of a loop to be divided and performed amongst the available processing threads in parallel. This was applied to the elastic force and Jacobian evaluations finite elements in the Chrono system. These calculations can be very time consuming for flexible bodies with a fine element mesh or multilayered laminated composite elements and the application of OpenMP can drastically reduce this time. AVX allows for the speed up of single instruction multiple data (SIMD) operations, such as large matrix operations. By allowing the multiple matrix element operations to be performed in parallel, the impact of single large matrix multiplication can also be reduced, particularly in the Jacobian matrix calculation. The addition of further high performance computing techniques, such as GPU parallel computing, in Chrono is discussed in Chapter 4 as

well. The effectiveness of OpenMP and AVX on flexible dynamics simulations in Chrono is quantified in benchmark examples shown in Chapter 5 and a total computation time reduction of 58.3% is achieved. This performance improvement allows for the simulation of high-fidelity physics-based full vehicle dynamics models to be done much more efficiently without sacrificing accuracy.

In Chapter 6, simulation examples were presented to demonstrate the extension of the deformable tire and terrain models to full vehicle dynamics simulation. The specifications of the wheeled and tracked vehicles used in the simulations were first described. There were two full vehicle simulations that utilize the deformable tire model. In the first scenario, four deformable tires were attached to the wheeled vehicle as it simply accelerates forward. In the second simulation, the wheeled vehicle undergoes a cornering simulation. In both of these cases, the vehicle dynamics will be compared to that of an equivalent model with rigid tires. To demonstrate the capability of the deformable soil model, a both a wheeled and tracked vehicle were examined. The first simulation contains a rigid wheeled vehicle dropped and accelerating over a deformable soil patch. The second scenario demonstrates the interaction between a tracked vehicle and a patch of finite element terrain in a similar manner.

REFERENCES

1. Bekker, M. G. 1969, *Introduction to Terrain-Vehicle Systems*, The University of Michigan Press, Ann Arbor.

2. Wong, J. Y. 2008, *Theory of Ground Vehicle. 4th ed.* Hoboken, NJ: John Wiley & Sons.

3. Contreras, U. Li, G., Foster, C.D. Shabana,A.A. Jayakumar, P. and Letherwood, M.D., 2013, "Soil Models and Vehicle System Dynamics", *ASME, Applied Mechanics Reviews*, Vol.65, 040802-1.

4. Xia, K., 2011, "Finite element modeling of tire/terrain interaction: Application to predicting soil compaction and tire mobility", *Journal of Terramechanics*, vol.48. pp.113-123.

5. Shoop S.A., Richmond,P.W., Lacombe, J., 2006, "Overview of cold regions mobility modeling at CRREL", *Journal of Terramechanics*, vol.43, pp.1-26.

6. Varghese, A.G., Turner, J.L., Way,T.R., Johnson,C.E., Dorfi, H.R., 2012, "Traction prediction of a smooth rigid wheel in soil using coupled Eulerian-Lagrangian analysis", *Proceedings of 2012 SIMULIA Community Conference*, pp.1-15.

7. Wasfy, T.M., Wasfy.H.M., Peters, J.M., 2014, "Coupled Multibody Dynamics and Discrete Element Modeling of Vehicle Mobility on Cohesive Granular Terrains", *Proceedings of the ASME 2014 IDETC & CIE Conference*, Buffalo, DETC2014-35146.

8. Negrut, D.,Serban, R., Mazhar, H., Heyn, T., 2014, "Parallel Computing in Multibody System Dynamics: Why, When and How", *ASME Journal of Computational and Nonlinear Dynamics,* 9:041007-1.

9. Heyn, T., Anitescu, M., Tasora. A, Negrut, D., 2013, "Using Krylov subspace and spectral methods for solving complementarity problems in many-body contact dynamics simulation", *International Journal for Numerical Methods in Engineering*, vol.95, pp.541-561.

10. Nakashima, H., and Oida, A., 2004, "Algorithm and Implementation of Soil-Tire Contact Analysis Code Based on Dynamic FE-DE Method", *Journal of Terramechanics*, vol.41, pp.127-137.

11. El-Gindy, M., Lescoe, R., Oljer, F., Jojansson, I., Trlvedl, M., 2011, "Soil Modeling Using FEA and SPH Techniques for a Tire-Soil Interaction", *Proceedings of the ASME 2011 IDETC & CIE Conference*, Washington, DETC2011-47104

12. Tasora, A., Serban, R., Mazhar, H., Pazouki, A. Melanz, D., Fleischmann, J., Taylor, M., Sugiyama, H., Negrut, D., 2015, "Chrono: An Open Source Multi-physics Dynamics Engine", *Lecture Notes in Computer Science*, vol. 9611, pp.19-49

13. Pazouki, A., Serban, R., Negrut, D., 2014, "A high performance computing approach to the simulation of fluid-solid interaction problems with rigid and flexible components", *Archive of Mechanical Engineering*, vol. 61, pp. 227-251

14. Yamashita, H., 2016, "Flexible Multibody Dynamics Approach for Tire Dynamics Simulation", Doctoral Thesis, University of Iowa, Department of Mechanical and Industrial Engineering

15. Project Chrono, 2016, "What is Project Chrono?", website, projectchrono.org/about

16. Madsen, J., 2014, "Validation of a Single Contact Point Tire Model Based on the Transient Pacejka Model in the Open-Source Dynamics Software Chrono", Technical Report, University of Wisconsin-Madison Simulation Based Engineering Lab

17. Mikkola, A., 2014, "Lugre Tire Model for HMMWV", Technical Report TR-2014-15, University of Wisconsin-Madison Simulation Based Engineering Lab

18. Project Chrono, 2016, "Anchoring in Poly-Disperse Granular Material", website, projectchrono.org

19. Yamashita, H., Valkeapää, A., Jayakumar, P., Sugiyama, H. and 2015, "Continuum Mechanics Based Bilinear Shear Deformable Shell Element Using Absolute Nodal Coordinate Formulation", *ASME Journal of Computational and Nonlinear Dynamics*, vol.10, 051012-1-9.

20. Simo, J. C., 1992, "Algorithms for Static and Dynamic Multiplicative Plasticity That Preserve the Classical Return Mapping Schemes of the Infinitesimal Theory", *Computer Methods in Applied Mechanics and Engineering*, vol. 99, pp. 61-112.

21. Bischoff, M., Ramm, E., 1997, "Shear Deformable Shell Elements for Large Strains and Rotations", *International Journal for Numerical Methods in Engineering*, vol. 40, pp.4427-4449

22. Yamashita, H., Jayakumar, P., Sugiyama, H., 2016, "Physics-Based Flexible Tire Model Integrated With LuGre Tire Friction For Transient Braking and Cornering Analysis", *ASME Journal of Computational and Nonlinear Dynamics*, vol. 11, 031017-1-17

23. Vu-Quoc, L., and Tan, X. G., 2003, "Optimal Solid Shells for Non-Linear Analyses of Multilayer Composites: I Statics", *Computer Methods in Applied Mechanics and Engineering*, vol. 192, pp. 975-1016

24. Vu-Quoc, L., and Tan, X.G., 2003, "Optimal Solid Shells for Nonlinear Analyses of Multilayer Composites. Part II: Dynamics", *Computer Methods in Applied Mechanics and Engineering*, vol.192, pp.1017-1059

25. Simo, J. C., and Rifai, M. S. and Fox, D.D., 1990, "On a Stress Resultant Geometrically Exact Shell Model. Part IV: Variable Thickness Shells with Through-the-Thickness Stretching", *International Journal for Numerical Methods in Engineering*, vol. 81, pp. 91-126

26. Betsch, P., and Stein, E., 1995, "An Assumed Strain Approach Avoiding Artificial Thickness Straining for A Non-Linear 4-Node Shell Element", *Communications in Numerical Methods in Engineering*, vol. 11, pp. 899-909

27. Sze, K. Y., 2002, "Three-Dimensional Continuum Finite Element Models for Plate/Shell Analysis", *Progress in Structural Engineering and Materials*, vol. 4, pp.400-407

28. Mostafa, M., Sivaselvan, M. V. and Felippa, C. A., 2013, "A Solid-Shell Corotational Element Based on ANDES, ANS and EAS for Geometrically Nonlinear Structural Analysis", *International Journal for Numerical Methods in Engineering*, vol. 95, pp.145-180

29. Andelfinger, U., and Ramm, E., 1993, "EAS-Elements for Two-Dimensional, Three-Dimensional, Plate and Shell Structures and Their Equivalence to HR-Elements", *International Journal for Numerical Methods in Engineering*, vol. 36, pp.1311-1337

30. Dvorkin, E. N., and Bathe, K. J., 1984, "A Continuum Mechanics Based Four-Node Shell Element for General Non-Linear Analysis", *Engineering Computations*, vol. 1, pp.77-88

31. Bathe, K. J. and Dvorkin, E. N., 1986, "A Formulation of General Shell Elements - The Use of Mixed Interpolation of Tensorial Components", *International Journal for Numerical Methods in Engineering*, vol. 22, pp.697-722

32. Betsch, P., and Stein, E., 1996, "A Nonlinear Extensible 4-Node Shell Element Based on Continuum Theory and Assumed Strain Interpolations", *Journal of Nonlinear Science*, vol. 6, pp. 169-199

33. de Souza Neto, E. A., Peric, D. and Owen, D. R. J., 2008, *Computational Methods for Plasticity: Theory and Applications*, Wiley

34. Project Chrono, 2016, "Project Chrono API/SDK Documentation", website, http://api.chrono.projectchrono.org//index.html

35. Coumans, E., 2015, "Bullet 2.83 Physics SDK Manual", website, bulletphysics.org

36. Intel, 2011, "Introduction to Intel Advanced Vector Extensions", website, software.intel.com/en-us/articles/introduction-to-intel-advanced-vector-extensions

37. Canudas-de-Wit, C., Tsiotras, P., Velenis, E., Basset, M. and Gissinger, G., 2003, "Dynamic Friction Models for Road/Tire Longitudinal Interaction", *Vehicle System Dynamics*, vol. 39, pp.189-226.

38. Deur, J., Asgari, J., Hrovat, D., 2004, "A 3D Brush-Type Dynamic Tire Friction Model", *Vehicle System Dynamics*, vol. 42, pp. 133-173